DEVELOPMENT OF MICROFLUIDIC CELL CULTURE PLATFORMS FOR INVESTIGATING CELLULAR PHENOMENA

By

Bryson McKinley Brewer

Dissertation
Submitted to the Faculty of the
Graduate School of Vanderbilt University
in partial fulfillment of the requirements
for the degree of
DOCTOR OF PHILOSOPHY
in
Mechanical Engineering
May, 2015
Nashville, Tennessee

Approved:
Deyu Li, Ph.D.
Robert W. Pitz, Ph.D.
Leon M. Bellan, Ph.D.
Donna J. Webb, Ph.D.
Rebecca M. Sappington, Ph.D.

ACKNOWLEDGEMENTS

This work was made possible through funding from the NSF Graduate Research Fellowship, IBM Fellowship, and a few other NSF and NIH grants. I was extremely fortunate to have been well funded throughout the course of my graduate studies, permitting me to focus worry-free on my research projects.

First, I would like to thank my advisor Dr. Deyu Li for all of his support and guidance during my Ph.D. program. Dr. Li reached out to me early on during my graduate school selection process and was one of the primary reasons I chose to attend Vanderbilt. Throughout my graduate school career, he has provided invaluable insight and has presented me with numerous interesting projects to pursue. Under his leadership, I have been exposed to interdisciplinary collaboration and have developed the skillsets required of an independent researcher, experiences that will undoubtedly benefit me throughout my career. I admire the way Dr. Li approaches both specific research problems and the basic pursuit of scientific knowledge, and I am fortunate to have completed this dissertation under his direction.

Next, I express my deepest gratitude to the rest of my committee members, Dr. Robert Pitz, Dr. Leon Bellan, Dr. Donna Webb, and Dr. Rebecca Sappington. Thank you for your time, patience, encouragement, valuable ideas, and helpful guidance throughout this process. I would also like to extend a special thank you to Dr. Yaqiong Xu for her interesting insights and thoughtful advice on several of my research projects.

I am also grateful to all of those with whom I have collaborated at Vanderbilt, particularly everyone in the Webb, Xu, and Sappington labs. Without your help, the work presented in this dissertation would not be possible. I would also like to acknowledge all

of my colleagues in the Micro/Nanoscale Thermal Fluids lab, both past and present. Your instruction, assistance, and irreplaceable friendship have certainly made my time here enjoyable (and entertaining).

Finally, I am deeply appreciative of the love, support, and encouragement of my parents and sisters – Ronnie, Shiela, Bethany, and Brooke Brewer. Your influences on my life are responsible for everything I have achieved. Thank you for making this journey possible.

TABLE OF CONTENTS

Page

LIST OF FIGURES

CHAPTER 1

INTRODUCTION

1.1 Background

Our understanding of cell and molecular biology has vastly improved over the last 100 years, partly because of tremendous contributions from assays based on cell culture; however, the commonly used *in vitro* cell culture/co-culture tools that lead to these advancements are not dissimilar to those used in the early days (Meyvantsson & Beebe, 2008). Large dishes and flasks typically used in biological cell culture offer little to no spatiotemporal control over the physical and chemical cues that can affect cell function and behavior (Meyvantsson & Beebe, 2008). Thus, the detailed study of cell interaction and behavior in culture is somewhat limited. The rapid development of microfluidic cell culture systems provides a solution to overcome these limitations. With the key features of laminar flow, optical transparency, biocompatibility, ease of fabrication, and device features comparable in size to cells, microfluidic cell culture systems are uniquely suited for manipulating the cellular microenvironment, addressing many limitations of traditional cell culture methods and allowing for the in-depth investigation of cellular interactions (Gao et al., 2011; George M Whitesides, 2006; Young & Beebe, 2010). As a result, an increasing number of cell biology researchers are beginning to employ microfluidic platforms in their investigations of fundamental cell phenomena. This introductory chapter provides some background on several important aspects of cell behavior and cell-cell interactions relevant to my Ph.D. research, and also describes the development of microfluidic cell culture systems and their use in investigations of interesting cell biology questions.

1.2 Cell Behavior and Cell-Cell Interactions

Cells serve as the fundamental building blocks of biological organisms. In order for these individual units to operate in coordination to form a functioning multicellular system, complex mechanisms are employed that allow cells to communicate with one another (Chen, Tan, & Tien, 2004). This communication may occur through direct cell-cell interactions or extracellular signaling via soluble factors (Cooper, 2000; Lodish et al., 2000) and is responsible for activities such as growth and development, tissue repair, immunity, and the maintenance of homeostasis (Chen et al., 2004). Furthermore, both cell-cell communication and cell interactions with the local microenvironment are essential for appropriate and expeditious cellular responses to a multitude of mechanical, chemical, and electrical stimuli (Kam, Shen, & Dustin, 2013). The remainder of this section provides fundamental information regarding three types of biological phenomena involving cellular communication and response that are relevant to the microfluidic cell culture studies presented in this dissertation; these topics are (1) neuron-neuron interaction and synapse formation, (2) cancer cell migration, and (3) inflammation and the immune response.

Neuron-Neuron Interactions and Synapse Formation

Neurons (or nerve cells) are specialized cells that, along with glial cells, form the basic units of the nervous system. Many different types of neurons exist within the human brain; however, all neurons share a similar architecture consisting of four primary features: (1) a cell body or *soma*, (2) dendrites, (3) an axon, and (4) pre-synaptic terminals (Kandel, Schwartz, & Jessel, 2000). Junctions formed between pre-synaptic terminals on the axon of one neuron and the post-synaptic regions on the dendrites of another neuron are referred to as synapses (M. Shi et al., 2013). Trillions of synaptic connections form functional networks of neurons that enable communication through the transmission of electrical signals via neurotransmitters (Scheiffele, 2003). These groups of neurons interconnected via synapses facilitate fundamental brain functions such as processing sensory information, initiating motor and emotional responses, and memory (Kandel et al., 2000). Despite the inherent complexity of the system, synaptic circuits are formed in a reproducible manner, with the number, location, and function of synaptic connections being well controlled (Scheiffele, 2003). Not surprisingly, the pursuit of a greater understanding of the process and factors that influence synapse formation is a fundamental area of neurobiological research.

In the process of synapse formation, the post-synaptic terminals are found on actin-rich protrusions called dendritic spines, originating from the dendritic shaft (Matus, Ackermann, Pehling, Byers, & Fujiwara, 1982). Dendritic spines are plastic in nature, having morphologies varying from filopodia-like protrusions to mature stubby, thin, or mushroom-shaped spines (Sorra & Harris, 2000). It is this plasticity that is thought to contribute to the highly dynamic behavior of synaptic contacts during formation (Dunaevsky, Tashiro, Majewska, Mason, & Yuste, 1999). In fact, abnormalities in dendritic spine density, morphology, and development have been associated with numerous neurological disorders including Alzheimer's disease, Parkinson's disease, and mental retardation (Chechlacz & Gleeson, 2003; Ferrer & Gullotta, 1990; Smith, Villalba, & Raju, 2009). Despite the apparent significance of spines and synapses on proper brain function, the molecular signals regulating the formation of these dynamic structures are not well understood (M. Shi et al., 2013). In addition to the molecular signaling involved in synapse formation, it has been shown that the transmission process through a stable synapse can be investigated using electrical and chemical excitation techniques (Dean, Bayliss, Erickson, Lawing, & Millhorn, 1990; Zimmermann & Whittaker, 1974). With these ideas as motivation, several strategies employing novel microfluidic systems that will allow for the in-depth examination of synapse formation and behavior will be presented in the course of this dissertation.

Cancer Cell Migration

Cancer is the leading cause of death in most developed countries of the world and was responsible for 7.6 million deaths worldwide in 2008 (Parkin, Pisani, & Ferlay, 1999). Upon receiving a cancer diagnosis, a patient's likelihood of survival diminishes dramatically if the cancer spreads from the primary tumor to other non-adjacent locations in the body (Valastyan & Weinberg, 2011). This migration of cancer cells throughout the body is called metastasis. As a result of the importance of metastatic potential in a patient's prognosis, much research has been devoted to the study of the migration of cancer cells in both the local tumor microenvironment and throughout the body (C. Y. Li et al., 2000). A multitude of factors influence the potential of a tumor to become metastatic including exchanges between tumor cells and the host tissue, the level of angiogenesis (development of vasculature) in the tumor, and interactions between tumor cells and the surrounding extracellular matrix (ECM) (Kalluri & Zeisberg, 2006; Stetler-Stevenson, Aznavoorian, & Liotta, 1993; Zetter, 1998). Although biochemical signaling has traditionally been the focus of cancer researchers studying the migration of cancer cells, mechanotransduction, or the response of tissues and cells to mechanical stimuli, is also known to play an important role in tumor development and progression (S. Huang & Ingber, 2005). Of particular interest is the role that fibroblasts in the local tumor microenvironment (deemed cancer-associated fibroblasts or CAFs) play in the reorganization of ECM to facilitate tumor progression and metastatic spread (Xing, Saidou, & Watabe, 2010). Subsequently, the mechanisms of the genesis of CAFs from surrounding healthy cells (including normal fibroblasts) is a subject of ongoing study (Polanska & Orimo, 2013). It is the role of mechanotransduction in the phenomena of cancer cell migration and modification of the local tumor microenvironment that will be explored using microfluidic approaches in this dissertation.

Inflammation and the Immune Response

The immune response is a set of biological processes that enable an organism to both detect the presence of foreign material in the body and prevent disease and further damage from occurring (Herbert & Cohen, 1993). Inflammation is a component of the immune system responsible for the repair of damaged or injured cells/tissues (Larsen & Henson, 1983) and has been one of the most intensively researched areas in experimental medicine for nearly two centuries (Schmid-Schönbein, 2006). The inflammatory response is a cascade of reactions and cellular activities (such as phagocytosis, chemotaxis, cell differentiation, etc.) that eventually results in a repaired tissue (Schmid-Schönbein, 2006). Numerous stimuli may trigger an inflammatory response, including burns, chemical irritants, physical trauma, stress, and infection by pathogens. Although certain mechanisms are common among many inflammation reactions, the precise mediators of the inflammatory response are highly dependent on the tissue, type of injury, and local microenvironment (Larsen & Henson, 1983). In addition, the normally protective biological function of inflammation is also associated with a variety of disorders and diseases ranging from atherosclerosis (Hansson, Robertson, & Söderberg-Nauclér, 2006) to cancer (Coussens & Werb, 2002). Thus, the ability to dissect individual mediation pathways for the inflammatory response in unique tissues and microenvironments is an important component of the development of therapeutic strategies targeting inflammatory diseases. In this dissertation, a novel microfluidic platform is presented that enables the detailed study of targeted signaling processes in the retinal neuroinflammatory response to aging and other neurodegenerative stressors.

1.3 Microfluidic Cell Culture Systems

Put simply, microfluidics encompasses the science and technology enabling the study of small volumes of fluid, typically on the order of 10^{-9} to 10^{-18} liters (George M Whitesides, 2006). Although the study of microfluidics is thought to have begun with the development of rudimentary parallel plate electrophoretic separation devices in the 1940s, it was not a heavily researched field until the beginning of the 1990s when analytical chemists realized that they could take advantage of the established silicon microfabrication techniques of the microelectronics industry to create miniaturized systems that offered several advantages over traditional chemistry techniques (Folch, 2013). However, the true explosion of interest in the capabilities of microfluidic technologies came with the development of soft lithography, which enabled the rapid prototyping of transparent elastomeric materials, of which the most popular is polydimethylsiloxane (PDMS) (Duffy et al., 1998; Whitesides et al., 2001). This new class of PDMS devices provided all of the advantages offered by glass and silicon based microfluidic devices – laminar flow, high surface area to volume ratio, negligible inertial effects, small reagent volumes, high throughput, biocompatibility, etc. – while also introducing the benefits of low-cost, optical transparency, elasticity, gas-permeability, and the ability to quickly produce a working prototype from an initial conceptual design (Beebe, Mensing, & Walker, 2002; Mukhopadhyay, 2007; Young & Beebe, 2010). It is this revolution that ushered in new applications for microfluidic technologies; researchers began exploiting microscale fluid physics in fields such as heat management, energy generation, display technology, and most prevalently, biology and medicine (Squires & Quake, 2005).

As the role of microfluidics in biology was being initially explored, it quickly became apparent that microfluidic devices were especially well-suited for cell biology research. The ability of microfluidic systems to precisely manipulate small volumes of fluid in device features roughly the same size as cells allows enhanced spatiotemporal control over the cellular microenvironment (Young & Beebe, 2010). Microfluidic cell culture systems also enable the precisely controlled exchange of culture media, simultaneous cell stimulation and imaging, parallelization and automation, and high-throughput single-cell manipulation and analysis (Mehling & Tay, 2014). As a result, a multitude of microfluidic cell culture systems have been proposed and demonstrated. For example, early work by Jeon et al. involved the design of a microfluidic gradient generator that could be used to study the chemotaxis of neutrophils in the presence of a chemoattractant gradient (Jeon et al., 2002). In this device, a bifurcating “Christmas tree” network of microchannels is employed to establish a soluble linear gradient of IL-8 in a cell culture chamber, achievable because of the inherent laminar flow characteristics present in most microfluidic systems. Using this setup, the migration of neutrophils in response to the chemoattractant gradient could be observed using microscopic techniques.

Another successful use of microfluidic technologies for cell culture is Taylor’s development of a microfluidic multicompartment device for neuroscience research (Taylor et al., 2003). In this microfluidic design, two large culture chambers are connected via a series of smaller microgrooves. Careful manipulation of the fluid volumes added allows reagents introduced in one chamber to be isolated from the opposite chamber by means of a hydrostatic pressure difference. With this setup, neurons can be loaded into one chamber and their subsequent neurite growth directed through the microgrooves into the opposite chamber. As a result, greater control over the manipulation of distinct neuronal microenvironments can be achieved when compared to traditional open culture methods.

Microfluidic platforms have also become increasingly important in the study of mechanotransduction in *in vitro* cell culture. A number of platforms have been developed that probe the effects of stimuli such as shear stress, interstitial flow, confinement, and stretching on a variety of cell types (Polacheck, Li, Uzel, & Kamm, 2013). For instance, a microfluidic stretcher device was developed by Huh et al. in which strain could be imparted on a suspended PDMS membrane by using vacuum pressure to deflect the sidewalls anchoring the membrane (Huh et al., 2010). Monolayers of human alveolar epithelial cells and microvascular endothelial cells were cultured on each side of the PDMS membrane. Then, application of a computer-controlled vacuum produced a cyclical stretch, emulating physiological breathing movements. This "lung on-a-chip" device was used to determine the effects of mechanical strain on the inflammatory response of lung tissues to foreign nanoparticles, and the platform was presented as a low-cost alternative to animal and clinical drug screening studies.

Finally, recent trends have attempted to move cell culture from the traditional practice of examining single layers of cells in two-dimensions to three-dimensional (3D) studies that more closely mimic the *in vivo* cellular microenvironment. Again, microfabrication and microfluidic strategies are well-suited for the investigation of cellular phenomena in a 3D culture system (Huh, Hamilton, & Ingber, 2011). For example, microfabrication can be employed to generate tissue-tissue interfaces that are not possible using conventional 3D ECM gel cultures to study the polarization of epithelial cells in the intestine, kidney, and cornea (Huh et al., 2011; Imura, Asano, Sato, & Yoshimura, 2009; Jang & Suh, 2010; Puleo, McIntosh Ambrose, Takezawa, Elisseeff, & Wang, 2009). In addition, 3D microfluidic systems will be instrumental in the development of future "human-on-a-chip" platforms that integrate numerous connected organ functionalities on a single device and will hopefully revolutionize the drug development and screening industries (Esch, King, & Shuler, 2011).

The future potential of microfluidics in cell culture studies is certainly high, as these examples are just a few of the demonstrated instances of the successful implementation of microfluidic cell culture. The foundation of work described here serves as the basis for the research presented in this dissertation.

1.4 Dissertation Overview

As demonstrated in this brief introduction, a wealth of interesting cell biology questions are primed for investigation using microfluidic cell culture platforms. This proposal presents the results of several projects addressing some of these issues. The dissertation is organized as follows.

Chapter I provides a brief introduction regarding several interesting cell biology phenomena, as well as the history and development of microfluidic technology for use in cell culture studies.

Chapter II presents two new methods that further develop previously demonstrated valve-separation cell co-culture systems. First, an oil barrier platform is described that employs an immiscible fluorocarbon oil barrier to separate cell culture chambers, limiting the physical damage imparted by mechanical valve designs while also being planar in nature, enabling compatibility with non-elastic device materials. A co-culture of neurons was maintained in the device, and separate transfections of the neuronal populations allowed for the subsequent imaging of synapse formation. Second, two versions of a membrane valve method are shown that use an inflatable PDMS membrane to separate cell culture chambers with large dimensions. The membrane valve offers the advantage of three-dimensional compatibility and better nutrient/waste exchange in three-dimensional hydrogels through enhanced flow perfusion.

Chapter III details the ligand trap, a microfluidic co-culture platform that uses a semi-permeable gel barrier containing embedded receptor-coated nanoparticles to selectively block the perfusion of specific signaling molecules between different cell populations. Various characterizations have been carried out to demonstrate the viability of the device design with several different ligand-receptor pairs. The applicability of the ligand trap in studies of the neuroinflammatory response of the retina as it relates to glaucoma is also explored.

Chapter IV presents a microfluidic stretcher platform that can be used to maintain long-term stress on fibroblasts cultured on a suspended PDMS membrane. Several interesting fibroblast behaviors were observed upon exposure to the mechanical stretch stimulus including increased production and organization of fibronectin in the locally deposited ECM and the enhanced ability to direct migration of cancer cells co-cultured with the fibroblasts. Along with the finding that stretched fibroblasts also exhibit increased expression of the tumor-associated growth factor receptor PDGFRα, these results indicate that mechanotransduction may be an important factor in the transformation of healthy fibroblasts into cancer-associated fibroblasts.

Chapter V details a novel microfluidic neuron co-culture system that incorporates graphene-based optoelectronic sensors that enable scanning photocurrent microscopy measurements of synaptic contacts. A photocurrent map showcasing synaptic regions in a neuronal network is presented, and the platform is also used to examine the photocurrent response of spines and protrusions upon global chemical stimulation of the neurons.

Chapter VI summarizes the research described in this dissertation and discusses the future outlook for microfluidic cell culture technology.

CHAPTER 2

ENHANCED VALVE-ENABLED MICROFLUIDIC CELL CULTURE SYSTEMS

2.1 Introduction

A number of microfluidic cell culture/co-culture platforms have been developed that demonstrate improved control over cell-cell interactions. Designs that use micropatterning of specific molecules on a substrate allow for selective attachment of specific cell types to pre-determined regions (Bhatia, Yarmush, & Toner, 1997; Kane, Zinner, Yarmush, & Toner, 2006; Khetani & Bhatia, 2008). Co-flowing laminar streams of fluid have also been used to load and treat cells within particular regions of a microfluidic channel (Lucchetta, Lee, Fu, Patel, & Ismagilov, 2005; Takayama et al., 1999). Alternative strategies employ the concept of compartmentalization, using microgrooves (Taylor et al., 2005), collagen tracks (Ravula, Wang, Asress, Glass, & Bruno Frazier, 2007), and semi-permeable membranes (Kimura, Yamamoto, Sakai, Sakai, & Fujii, 2008) to separate cell populations. New cell biology assays have been developed based on the novel capabilities these platforms provide; however, there is still a need for better manipulation and more control of the cellular microenvironment. For example, a successful co-culture device should at least allow for (1) loading of different cell types into specific compartments, (2) culture of each cell type in its optimal media until reaching confluence, (3) manipulation of one cell population’s microenvironment without affecting other nearby populations, and (4) real-time, high resolution imaging (Gao et al., 2011).

One microfluidic cell co-culture design previously developed in our lab that incorporates these basic desired functions uses a pneumatically or hydraulically controlled polydimethylsiloxane (PDMS) barrier to separate cell populations (Gao et al., 2011). Using this approach, cells of different types can be cultured to confluence and transfected or stained individually in cell culture chambers that remain separated by the PDMS valve barrier. Then, upon release of the barrier, different cell populations are allowed to interact in a controlled manner (**Fig. 2.1**). This platform has been successfully used for various applications, including the observation of dendritic spine and synapse formation among primary hippocampal neurons separately transfected with pre- and post-synaptic markers (Gao et al., 2011; Majumdar, Gao, et al., 2011) and the investigation of the effects of secreted angiocrine factors on the regulation of tumor cell/endothelial cell cross-migration (Brantley-Sieders et al., 2011). However, despite these positive results, this platform still suffers from some limitations. For example, the valve-enable PDMS barrier cannot be considered truly reversible because cells, neurites, or other biological material trapped under the PDMS barrier during its actuation would incur physical damage (Hosmane et al., 2011). Also, the rectangular shape of the region under the PDMS barrier results in a sieve valve effect (Marcus, Anderson, & Quake, 2006; Melin & Quake, 2007) that can allow leakage of some small molecules between the separated cell culture chambers. Although this could be partially remedied by using rounded profiles in the barrier region (Unger, Chou, Thorsen, Scherer, & Quake, 2000), forming a complete seal is still a challenge. In addition, using rounded channels requires more complicated and time-consuming fabrication (Fordyce, Diaz-Botia et al., 2012), making this strategy less than ideal. Finally, the small height dimension of the valve barrier region makes the platform two-dimensional in this part of the device; a similar three-dimensional platform would require a much larger interfacial cross-sectional area after the valve has been opened and the cell populations are allowed to interact. Thus, in this chapter a couple of alternative approaches are presented to address some of the limitations of the previously established valve-enabled PDMS barrier platform.

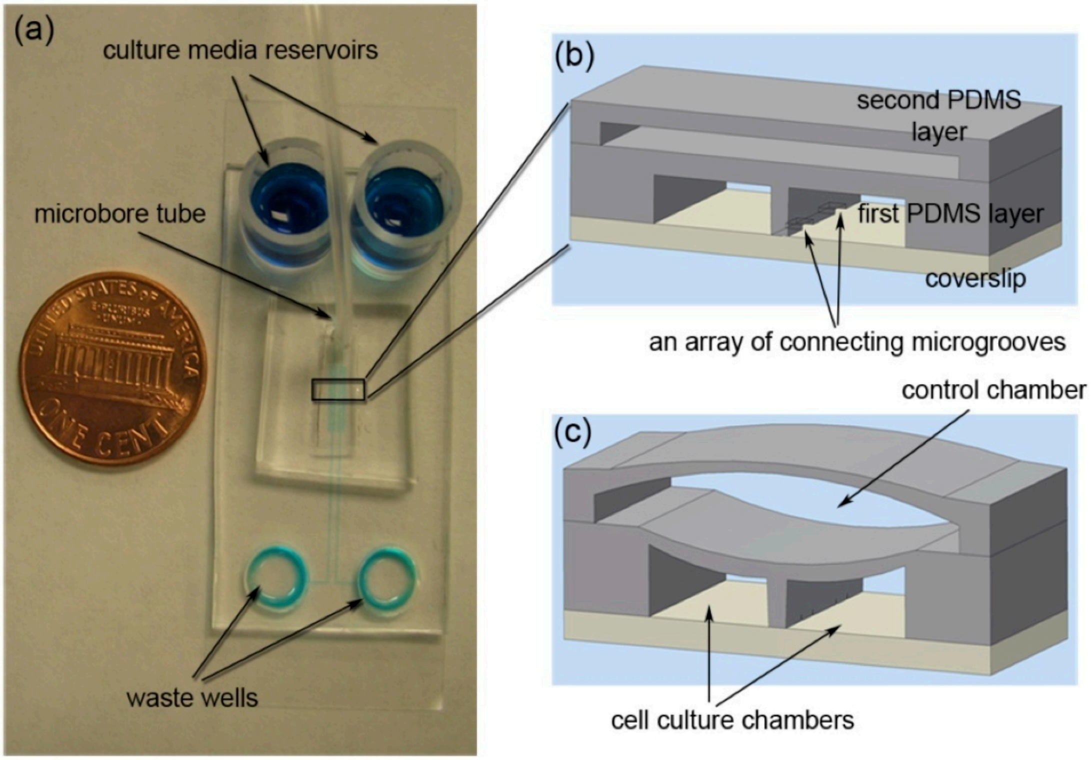

Figure 2.1: Schematics demonstrating the valve-enabled microfluidic cell co-culture platform. **(a)** A photograph showcasing the primary features and the size of the microfluidic platform. **(b)** A cross-section diagram showing the device in the "open" position. Note that the array of microgrooves that connect the two chambers may also be replaced with a single continuous PDMS valve barrier. **(c)** After applying pneumatic or hydraulic pressure to the upper control chamber, the two cell culture chambers are isolated from one another. This figure was reproduced from (Gao, 2011).

2.2 Oil Barrier Platform

2.2.1 Motivation

One means of achieving well-sealed, reversible separation of cell populations in microfluidic co-culture platforms is to use a non-solid barrier. Several instances have been demonstrated in the literature for a variety of applications of this strategy. For example, a pinned interface between two immiscible fluids has been achieved by selectively changing the surface chemistry in specific regions of a microchannel (Atencia & Beebe, 2005). Using this technique, a stable gas/liquid interface, or virtual wall, can be formed. After channel modification, surface tension will counteract the effects of gravity and confine water to the hydrophilic regions of the microchannel, provided the pressure difference between the air and water phases does not exceed a critical value. This method is particularly useful for applications in which dissolved gas species need to be removed from a liquid, such as extracting dissolved oxygen from water (Hibara et al., 2005). Gas/liquid interfaces may also be employed to expose a gas species to a liquid phase to initiate a chemical reaction or adjust the pH of a solution (Atencia & Beebe, 2005). In addition to forming pinned interfaces between gases and liquids, surface modification has been used to stabilize the interface between different immiscible liquids for both vertical (Zhao, Viernes, Moore, & Beebe, 2002) and horizontal (Hibara et al., 2002) liquid/liquid interfaces. Pinned interfaces are well-suited for use in drug partitioning studies (Surmeian et al., 2002), ion extraction from solvents (Maruyama et al., 2004), enzymatic reactions (Maruyama et al., 2003), and formation of membranes through interfacial polymerization (Zhao et al., 2002). However, pinned interfaces created using surface modification present several challenges for biological studies involving cell culture. First, changing the surface chemistry of microchannels requires an additional fabrication step when compared to other microfluidic platforms, complicating device production. Studies have also shown that with decreasing surface wettability via treatment with chemicals such as octadecylsilane, the growth and proliferation of attached cells may be reduced (Altankov, Grinnell, & Groth, 1996). In addition, the critical differential pressure across a pinned liquid/gas or liquid/liquid boundary generated using surface modification may be too low to ensure interface stability in long-term cell culture applications. Thus, difficulties would likely arise in attempting to implement this technique in the construction of a reversible cell culture barrier.

An improved technique incorporates microposts into microfluidic channels to enhance the stability of the interface between two fluids by increasing the critical differential pressure required to rupture the interface (Berthier et al., 2009; Tetala, Swarts, Chen, Janssen, & van Beek, 2009; Xu, Xue, Bachman, & Li, 2006). One demonstration of this method employs an array of microposts to separate a middle channel containing water from two outer chambers containing air (Lai, Xu, & Allbritton, 2011). Thus, a virtual wall barrier is formed between two chambers. As long as the critical pressure is not exceeded, water will remain confined to the central channel and not flow into the outer chambers. With careful operation, this method could likely be inverted so that an air layer is used to separate two chambers filled with water. While this type of device was shown to be effective at trapping cells in the regions between microposts (Lai et al., 2011), a few challenges prevent it from being useful for the type of neurobiology and cancer biology studies previously conducted using the solid-PDMS valve barrier platform. First, in order to create an interface, the PDMS channels were allowed to recover their natural hydrophobic state before loading any water into the device. Hydrophobic channels are less compatible with the more user-friendly passive pumping method (Walker & Beebe, 2002) used in our previous studies (Gao et al., 2011). In addition, for channels with sharp corners or other irregular features, a hydrophobic surface increases the chance of small air bubbles forming in the cell culture chamber. Problematically, the presence of air in the cellular microenvironment can be detrimental to cell viability (Skelley & Voldman, 2008; Sung & Shuler, 2009; Zheng, Wang, Zhang, & Jiang, 2010). Reversibility of the valve may also be difficult, particularly when trying to use an air-based virtual wall. Once the channel walls in the valve region are wetted by the aqueous phase, reintroducing a stable air barrier will be very difficult without first completely drying out the entire device. Finally, the permeability of PDMS to air (Hosokawa, Sato, Ichikawa, & Maeda, 2004; Kang, Kim, & Park, 2008; Merkel, Bondar, Nagai, Freeman, & Pinnau, 2000) could result in the degradation of an air-based virtual wall in long-term cell culture. Thus, significant modification of the virtual wall concept is needed for successful implementation into a microfluidic cell co-culture platform.

This section details a microfluidic cell co-culture platform that uses a liquid fluorocarbon oil (Fluorinert FC-40) phase to reversibly separate two cell populations without the need for a surfactant (Brewer, Shi, Edd, Webb, & Li, 2014). In this design, two outer cell culture chambers are connected via a series of microgrooves to a middle channel in which FC-40 can be loaded to separate cells from one another without crushing the cell bodies/processes in the barrier region. Liquid fluorocarbons such as FC-40 have been used in a variety of microfluidics applications including droplet actuation (Chatterjee, Hetayothin, Wheeler, King, & Garrell, 2006), nanoparticle synthesis

(Shestopalov, Tice, & Ismagilov, 2004), and cell encapsulation (Köster et al., 2008), and its biocompatibility is well documented (Köster et al., 2008; Lowe, Davey, & Power, 1998; W. Shi et al., 2010). The FC-40 oil barrier is created by taking advantage of the immiscibility of the fluorocarbon oil (located in the middle channel) and the aqueous media found in the outer cell culture chambers, which can form a stable interface in the reduced cross-sectional area of the connecting microgrooves. This was achieved without any special surface modifications (other than standard oxygen plasma treatment used for device fabrication) or the necessity of hydrophobic channel walls, and the barrier can remain stable for multiple days. A thorough characterization of the oil barrier platform was performed. The stability of the oil barrier over time and under differential pressure was examined. Also, the interface between the oil and water phases was studied by dynamically changing the FC-40 flow rate. Furthermore, a rudimentary COMSOL™ model was developed that helps predict oil barrier performance. In addition, tests were conducted evaluating the use of either air or FC-40 + surfactant as the separating fluid. The platform was also used to observe the initial synaptic contact between two populations of primary hippocampal neurons separately transfected with different fluorescent proteins, demonstrating the viability of the device for use in cell culture studies. Additionally, results show that the oil separator more effectively blocks the transport of small CellTracker dyes, indicating that it could provide a better fluidic seal than the solid-PDMS valve barrier platform. Finally, it is worth noting that although PDMS was used to fabricate these devices, other materials such as thermoplastics could be used as well, since the operation of the barrier requires no deformation to achieve separation. This is important because PDMS is permeable to many small molecules

(Toepke & Beebe, 2006) and incompatible with most organic solvents (J. N. Lee, Park, & Whitesides, 2003). Thus, for applications in which these issues are a concern, oil barrier platforms made of alternative materials that do not suffer from permeability problems could be advantageous.

2.2.2 Oil Barrier Design, Fabrication, and Operation

As shown in **Fig. 2.2**, the liquid fluorocarbon oil barrier platform consists of two outer cell culture chambers (1 mm x 5 mm x 100 µm; width *(w),* length (*l*), and height (*h*), respectively) separated by a 200 µm (*w*) x 100 µm (*h*) oil channel. The series of microgrooves connecting the oil channel to the outer culture chambers are each 100 µm (*l*) x 50 µm (*w*) x 5 µm (*h*). The device was fabricated using standard soft lithography techniques (McDonald & Whitesides, 2002; Whitesides et al., 2001).

A reusable master mold was created using SU-8 multi-layer photolithography. The 5 µm layer for the connecting microgrooves was patterned by spinning SU-8 2005 (Microchem, Newton, MA) at 2000 RPM for 35 seconds. After pre-baking at 95°C for 2 minutes, the SU-8 was exposed through a photomask (CAD/Art Services Inc., Bandon, OR) with an exposure energy of 390 mJ/cm^2 using a Novacure 2100 Spot Curing System (EXFO Inc., Quebec, CANADA). The 5 µm layer was completed after a 3 minute post-bake at 95°C and development with SU-8 developer (Microchem, Newton, MA). Similarly, the 100 µm layer for the oil channel and cell culture chambers was patterned by spinning SU-8 2050 at 1650 RPM for 35 seconds, pre-baking at 65°C for 5 minutes and 95°C for 20 minutes, manually aligning the photomask and exposing at 390 mJ/cm^2, post-baking at 65°C for 1 minute and 95°C for 10 minutes, and developing for ~10 minutes with SU-8 developer.

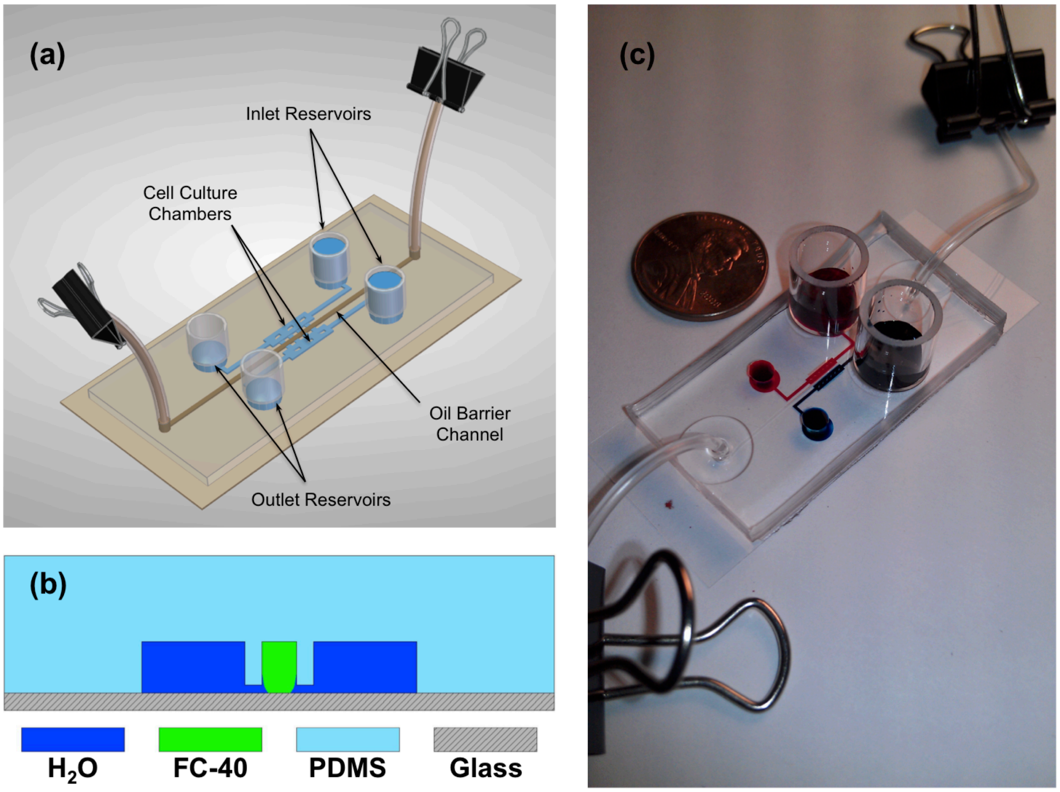

Figure 2.2: Design of the fluorocarbon oil barrier microfluidic platform. **(a)** Three-dimensional schematic of a loaded, static oil barrier device. **(b)** A cross-section diagram of the device showing the fluidic connection between the outer cell culture chambers and the middle oil channel via microgrooves (not to scale). **(c)** A photograph demonstrating a static oil barrier device separating red dye in the left culture chamber from blue dye in the right culture chamber. A U.S. penny is shown for scale.

After fabrication of the master, liquid PDMS base polymer was mixed with the curing agent (Ellsworth Adhesives, Germantown, WI) at a 10:1 mass ratio and poured over the mold, which was degassed in a vacuum for ~1 hour and cured for at least 2 hours at 70°C. After curing, the solid-PDMS layer was cut and peeled from the mold, and holes were punched to form the inlets and outlets of each channel. Next, the PDMS device and a glass coverslip (VWR Vista Vision, Suwanee, GA) were treated in a plasma cleaner (Harrick Plasma, Ithaca, NY) and bonded together, forming an irreversible seal. Deionized (DI) water was immediately added to the channels in order to prevent the PDMS from reverting to its natural hydrophobic state (Duffy et al., 1998). Pyrex cloning cylinders (Fisher Scientific, Pittsburgh, PA) were attached to the inlet and outlet reservoirs of the cell chambers using uncured liquid PDMS. In addition, 0.02” I.D./0.06” O.D. Tygon microbore tubing (Cole-Parmer, Vernon Hills, IL) was inserted into the inlet and outlet holes of the middle oil channel and sealed with uncured liquid PDMS. Finally, the assembled device was placed in a 70°C oven for ~1 hour to cure the PDMS seals around the reservoirs and tubing, during which time the channels remained filled with DI water.

In addition, a four-chamber version of the oil barrier device was fabricated using the same protocol (see **Fig. 2.3**). The four-chamber device design is simply a modified two-chamber design with an outer cell culture chamber and oil channel attached via microgrooves to the right and left of the inner culture chambers. Thus, the four-chamber device contains three oil channels that can be used to independently separate all of the culture chambers. It is worth noting that for the purpose of demonstration, we employed only the central oil channel for all experiments performed in this study. The dimensions of the key features of the four-chamber platform are identical to those of the two-chamber design. A summary of the fabrication procedure for the oil barrier device (two-chamber version) is shown in **Fig. 2.4**.

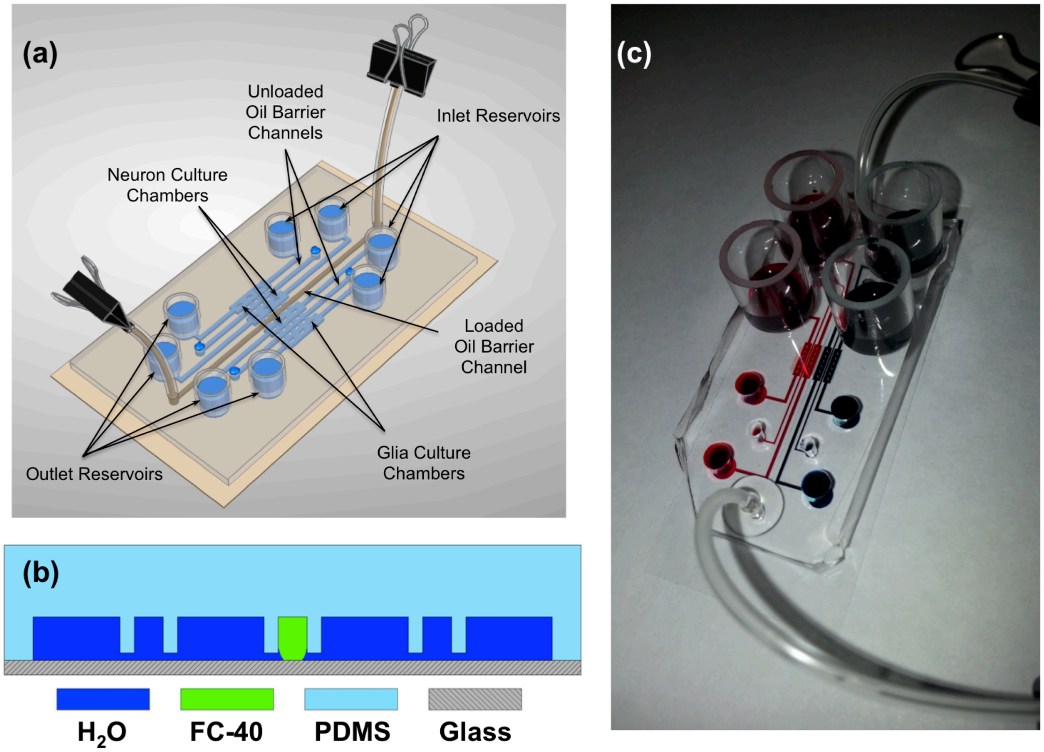

Figure 2.3: Design of the four-chamber oil barrier microfluidic platform. **(a)** Three-dimensional cartoon of a static four-chamber oil barrier device in which the middle oil channel is loaded with FC-40. Note that for the experiments performed in this paper, only the center oil channel was filled with oil; thus, the two inner chambers were separated from one another while the outermost chambers were fluidically connected to the inner chambers at all times. However, all chambers may be isolated from one another by filling all three oil channels with FC-40. **(b)** A cross-section diagram of the four-chamber device, showcasing the fluidic connection between the outer cell culture chambers and the inner chambers. **(c)** A photograph demonstrating a static oil barrier isolating the two chambers with red dye on the left from the two chambers with blue dye on the right.

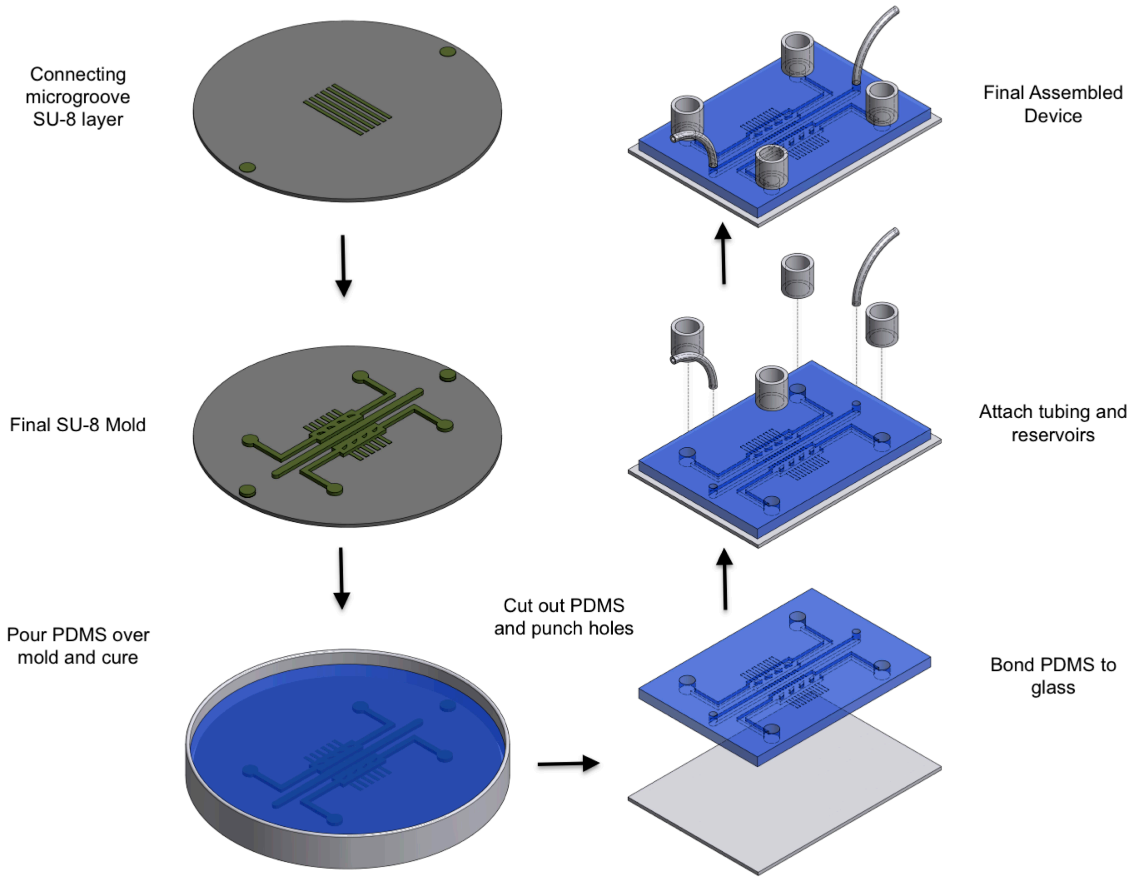

Figure 2.4: Summary of the fabrication of a two-chamber oil barrier device.

Static and Dynamic Device Operation

The FC-40 oil barrier device can function in two schemes: a static approach and a dynamic approach. In the static scheme, the first step is to remove any excess liquid from the inlet and outlet reservoirs of the culture chambers. This helps to achieve a gross pressure balance between the two phases during initial loading. Then, a syringe is used to slowly inject FC-40 into the middle channel, displacing the aqueous phase already there. Once the oil occupies the entire channel and tubing, a ¾″ AACO binder clip is used to clamp the tubing, first on the syringe end and then on the open end. This ensures that the oil channel does not become pressurized, causing oil leakage into the outer culture chambers. Media can then be added to the reservoirs as necessary. On the other hand, the dynamic scheme uses a syringe pump (Chemyx Inc., Stafford, TX) to flow oil continuously through the middle channel. A syringe filled with FC-40 is directly attached to the inlet tubing of the middle oil channel; a syringe pump is then used to control the flow rate (up to ~125 μL/min) to maintain a stable oil barrier. There are advantages for both approaches, depending on the application. The static oil barrier is more user-friendly for biological studies, as the entire device can be contained within a Petri dish, making it easier to maintain a sterile environment as the device is transferred between culture hoods, incubators, and microscopes. However, greater control over the oil/water interface was demonstrated using the dynamic oil barrier, which could be advantageous for applications in which the use of a syringe pump is not problematic. Both strategies were used in this study for characterization of device performance, although only the static oil barrier was used for biological testing.

Proper media flow in the cell culture chambers was achieved using a previously demonstrated passive pumping method in which the pressure drop created by a difference in fluid level height between the inlet and outlet reservoirs drives the flow (Gao et al., 2011). A variety of factors can influence the flow rate in this method, including fluid level, the shape and completeness of the meniscus formed in each reservoir, evaporation, and time since loading media (Lynn & Dandy, 2009). Thus, well-determined flow rates were not achieved for this approach; however, as demonstrated previously for similar microfluidic cell culture applications, the passive pumping method is sufficient for supplying cells with fresh media, as well as removing waste from the culture region (Gao et al., 2011). Nonetheless, the Hagen-Poiseuille equation ($\Delta p = R_{hyd} Q$, where Δp is the pressure drop, R_{hyd} is the hydraulic resistance of a rectangular channel, and Q is the flow rate) can be used to estimate the range of flow rates realized in the device. Using this method, the maximum flow rate just after loading media was estimated to be ~20-60 nL/s (depending on the channel length and volume of media loaded), with the flow rate decreasing over time until the culture media was refreshed.

2.2.3 Device Characterization and FEM Modeling

Long-term Stability of the Static Oil Barrier

The effectiveness and stability of the FC-40 valve were investigated by loading a static oil barrier and observing how well the barrier confined the fluorescent dye fluorescein isothiocyanate (FITC) to one culture chamber. To demonstrate the long-term stability of the FC-40 separator, a static oil barrier was loaded and the water-based fluorescent dye was used to visualize the location of the oil/water interface. FITC (Thermo Scientific, Rockford, IL) was added to one culture chamber after loading the oil barrier; images were then captured periodically using a Nikon AZ100 fluorescence microscope (Nikon Instruments Inc., Melville, NY). At the end of the experiment, DI water was injected into the middle oil channel, replacing the FC-40. A final image was captured just after (<5 min) removing the oil barrier. As shown in **Fig. 2.5**, the presence of oil in the middle channel effectively confined FITC to the loading side for ~72 hours. However, shortly after removing the oil barrier, the FITC was able to quickly diffuse into the opposite chamber. Note that the movement of FITC across the oil barrier region and into the opposite cell culture chamber is caused primarily by diffusion, and is likely not the result of a "dragging" effect induced by the water displacing the oil in the middle channel. Significant FITC migration was only observed after the oil was completely displaced and the flow of water in the middle channel stopped. This is consistent with our way of replacing the oil with water through injecting water to push the oil out, rather than withdrawing the oil using negative pressure. These results indicate that the static FC-40 valve is capable of preventing perfusion of small molecules for extended periods of time (> 3 days).

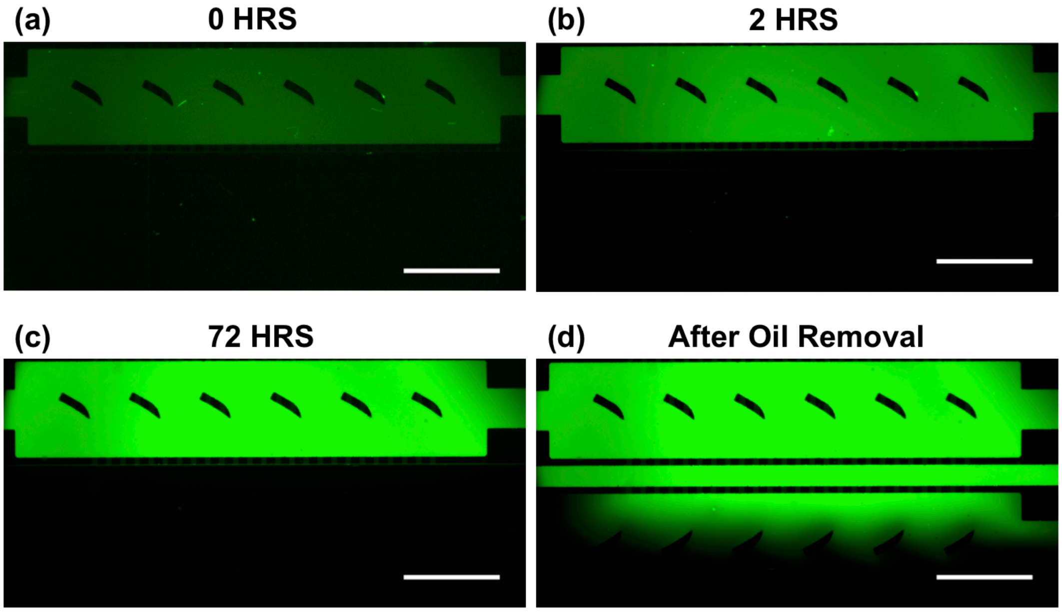

Figure 2.5: Demonstration of the long-term stability of a static oil barrier device using FITC. Fluorescence images were obtained **(a)** immediately after loading the static oil barrier, **(b)** after 2 hours, **(c)** after 72 hours, and **(d)** after removing the oil barrier (< 5 minutes). Note that the concentration of FITC in the device increases over time due primarily to evaporation of the aqueous solvent. The scale bar is 1 mm.

It is worth noting that all tests were performed at room temperature (20°C); however, for later biological tests, instabilities in the oil barrier were observed when room temperature FC-40 was added to a device that had been stored in a 37°C incubator. We observed oil leaking into the cell culture chambers shortly after loading the barrier because of thermal expansion of the oil as its temperature increased; this can be determined from the equation

$$\frac{\Delta V}{V_i} = B(\Delta T) \tag{2.1}$$

where $\Delta V/V_i$ is the relative volume change with respect to the initial volume, B is the volumetric coefficient of expansion ($0.0012°\mathrm{C}^{-1}$ for FC-40), and ΔT is the change in temperature. According to Eq. (2.1), an expansion of ~2% occurs as the oil is heated from 20°C to 37°C. Since the inlet and outlet tubes are clamped, the oil expands into the cell culture chambers, resulting in the observed leakage. Thus, extra care was needed when conducting biological studies to ensure that both the FC-40 oil and the device were at the same stable temperature. This was achieved by first pre-heating the FC-40 oil and syringe in the 37°C incubator. Then, the entire microfluidic device was placed on a 37-40°C hotplate during the actual loading of the oil barrier. Loading of a static oil barrier typically required < 5 minutes. By quickly returning the device to the incubator after loading, a stable oil barrier was maintained. For applications in which devices must be removed from the incubator for extended periods of time (i.e. live-cell imaging with the oil barrier loaded), a temperature-controlled microscope stage is recommended, as mismatches in expansion coefficients between the oil and the rest of the device may result in barrier instabilities as the device cools to room temperature. Finally, it is worth noting that the FC-40 is biocompatible and small leakage into the cell culture chamber is fine as long as interference with imaging is not an issue. In fact, we did not observe any detrimental effects on cells that had come into contact with FC-40 that leaked into the culture chambers.

Investigation of the Shape of the Oil/Water Interface

A more thorough investigation of the oil/water interface was conducted using confocal microscopy. Both a static and dynamic oil barrier with oil flow rates up to 150 μL/min were analyzed. For the static case, an oil barrier was introduced into a device initially filled with FITC. Then, using a Quorum WaveFX spinning disk confocal system equipped with a Nikon Eclipse Ti microscope (Nikon Instruments Inc., Melville, NY) and a Hamamatsu ImageEM-CCD camera with a Plan Fluor 40X objective (N.A. 1.3), a z-stack of images (vertical resolution of 0.2 μm) focused on the oil/water interface at a single microgroove was obtained using MetaMorph imaging software (Molecular Devices, Sunnyvale, CA). Similarly, z-stacks of images were acquired for dynamic oil barriers generated using different flow rates after the oil/water interface had stabilized in the microchannel. These images were post-processed using ImageJ, allowing for visualization of the overhead view and side-view cross-sections, as well as three-dimensional reconstructions of the interface. The radii of curvature of the interface in both planes were determined from these reconstructions to derive the pressure drop across the oil-water interface. Top and side views of the interface are presented in **Fig. 2.6**, which shows a single connecting microgroove for both a static and dynamic oil barrier. From these images, a noticeable layer of water (in green) is observed on the sidewalls of the middle channels. This wetting of the channel walls by the aqueous phase is likely a result of the hydrophilic nature of the PDMS after plasma bonding, achieved by keeping the channels immersed in water before testing (Ren, Bachman, Sims, Li, & Allbritton, 2001). In addition, an ultra-thin boundary layer of water appears to be present at the bottom of the channel on the glass substrate. As expected, the thicknesses of these aqueous layers decreases as the oil flow rate increases from 0 to 125 µL/min. Although the presence of an ultra-thin residue film of water across the bottom of the oil barrier could potentially result in unwanted mass transport between culture chambers, sensible leakage across the barrier was not observed in any of our biological testing.

As illustrated in **Fig. 2.6**, the radius of curvature of the oil/water interface in both the overhead and cross-sectional planes decreases with increasing flow rate. By measuring these radii of curvature, the pressure drop across the oil/water interface can be determined using the Young-Laplace equation,

$$\Delta p = \gamma\left(\frac{1}{R_1} + \frac{1}{R_2}\right) \tag{2.2}$$

in which Δp is the pressure drop, γ is the interfacial tension between water and FC-40 (52.07 mN/m) (Mazutis & Griffiths, 2012), and R_1 and R_2 are the radii of curvature in both planes. The pressure drop values calculated ranged from 0.33 kPa for the static case to 3.43 kPa for the max oil flow rate of 125 µL/min. For an oil flow rate of 150 µL/min, leakage of oil into the cell culture chambers was observed; thus, for an interfacial pressure drop of > ~4kPa, the surface tension force is overcome by the fluidic pressure in the oil phase, resulting in barrier failure. This analysis also suggests that by decreasing the microgroove dimensions and subsequently, the radii of curvature of the interface, the magnitude of the interfacial pressure drop that can be supported by the device will increase. Note that the pressure drop values calculated here are comparable to or better than those observed in previous virtual wall microfluidic platforms (~1.5-1.9 kPa) presented in the literature (Lai et al., 2011).

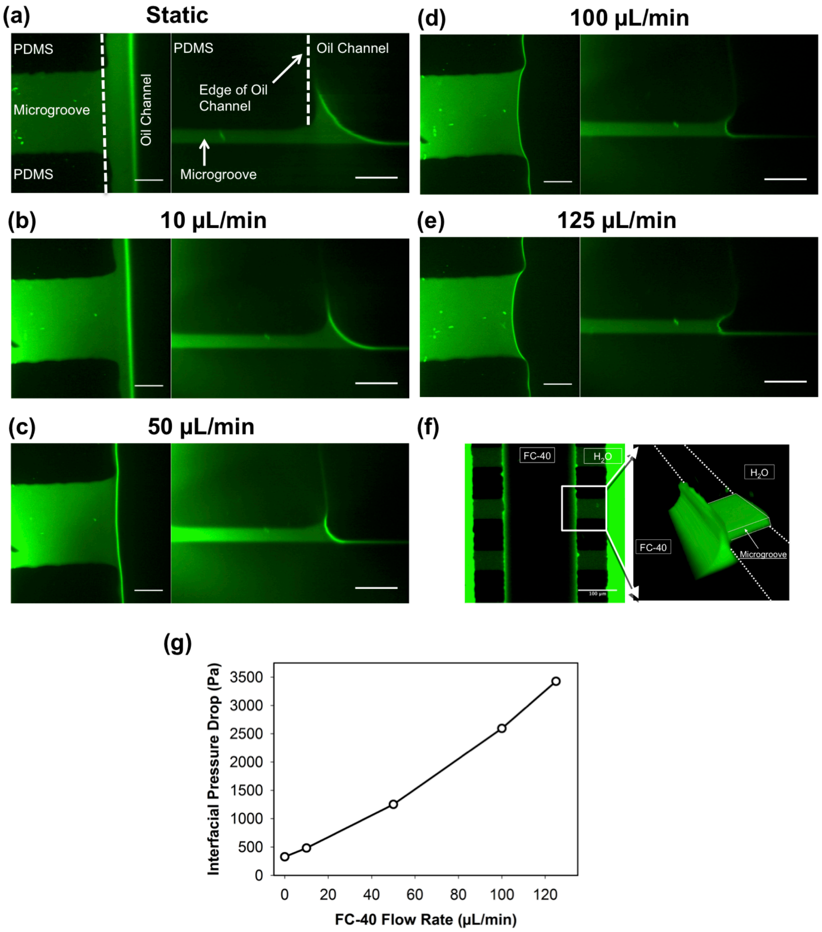

Figure 2.6: Top-view images and cross-sectional/three-dimensional reconstructions of the oil/water interface in both static and dynamic oil barrier devices. FITC was used to visualize the aqueous phase. **(a-e)** The oil flow rate was increased from 0 µL/min to 125 µL/min for each z-stack of images captured. The scale bar in all images is 20 µm. **(f)** A three-dimensional reconstruction showcases the oil/water interface along a section of the middle channel. **(g)** The interfacial pressure drop between the higher pressure oil phase and lower pressure aqueous phase as a function of FC-40 flow rate as calculated using the Young-Laplace equation.

Finite Element Modeling of Oil Barrier

In addition to experimentally evaluating the capabilities of the oil barrier platform, a finite element model was developed using COMSOL Multiphysics™ that roughly predicts the interfacial pressure drop that would induce barrier failure. A two-dimensional model employing the two-phase, laminar flow physics was used to simulate a static oil barrier device with a pressure difference between the two outer cell culture chambers. For computational simplicity, a single microgroove was examined. Note that three-dimensional models using the full geometry of the oil barrier were developed and tested, but the computational requirements and given resources made the model impractical for continued use. The two-dimensional geometry used is shown in **Fig. 2.7**, where the width of the barrier region is 200 µm and length and width of the microgroove are 50 µm and 100 µm, matching the geometry of the actual oil barrier device. A constant pressure, no viscous stress inlet condition was applied at position 1 (P_1) with a value varying from 0.1-10 kPa, and a constant pressure, no viscous stress outlet condition with a value of 0 kPa was applied at position 2 (P_2). The contact angle was defined at the boundaries of the microgrooves, while a no slip boundary condition was applied to the walls of the middle channel. Note that the top and bottom of the oil barrier middle channel is "capped," consistent with a static oil barrier platform that has been loaded with its tubing clamped. The interfacial tension between the water and FC-40 oil phases was assumed to be 52.07 mN/m (Mazutis & Griffiths, 2012).

The results of the parametric analysis in which the inlet pressure was varied from 0.1-5 kPa are summarized in **Fig. 2.8**. For differential pressures less than 2.5 kPa, the oil barrier region remains stable enough to successfully keep the two microgrooves (and subsequently, the cell culture chambers) fluidically isolated. However, at 5 kPa, the oil barrier fails and the water phases on each side of the barrier are connected. This breakdown pressure range of ~2.5-5 kPa agrees well with the previous experimental results obtained by analyzing the dynamic oil-water interface using confocal microscopy, as well as observations made when performing simple qualitative tests of the static oil barrier capabilities. Note, however, that in the real device the oil pressure is typically higher than what was used in the model, and minor amounts of oil leakage did not result in barrier failure. Thus, although this simple two-dimensional model is not useful for obtaining quantitative information regarding FC-40 oil barrier performance, it can be used as a qualitative guide when designing future variations of the oil barrier platform to gauge device capabilities before actually fabricating and testing the device.

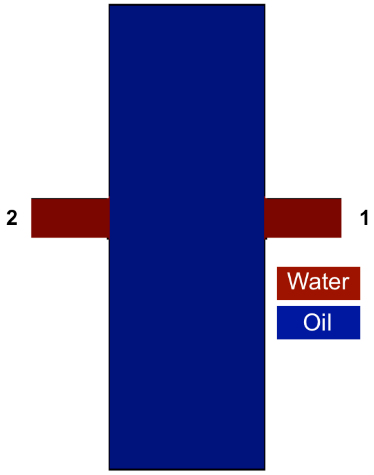

Figure 2.7: Geometry and boundary conditions of the two-dimensional COMSOL™ model predicting oil barrier stability under a differential pressure between cell culture chambers.

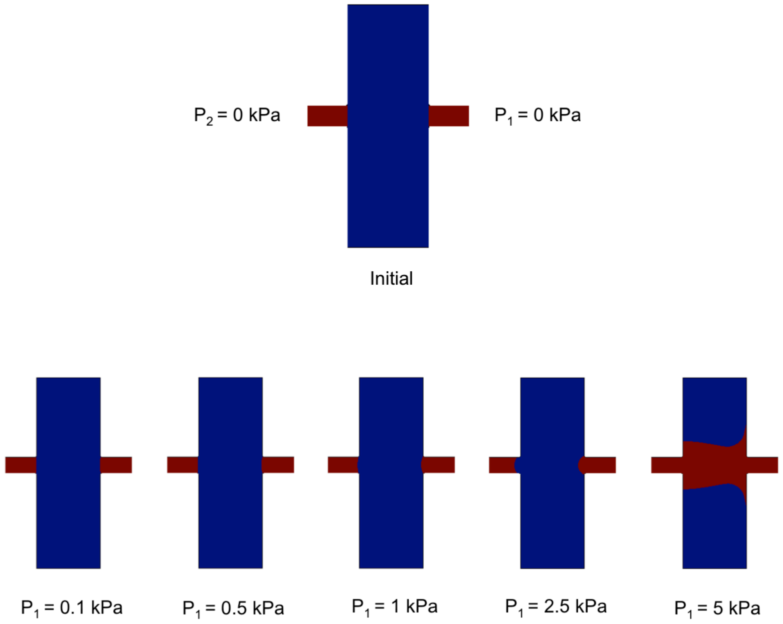

Figure 2.8: Results of two-dimensional COMSOL™ model for predicting oil barrier stability. P_1 represents the applied hydrostatic pressure from the right cell culture chamber via the microgroove, while P_2 is maintained at 0 kPa for all studies. Thus, the differential pressure between the two cell culture chambers on each side of the static oil barrier is equal to the applied pressure P_1.

Use of Alternative Fluids in the Barrier Region

In addition to standard FC-40, the use of alternative fluids in the oil barrier microfluidic device was explored. First, instead of using oil or another liquid, the barrier region was loaded using air. The same static barrier loading procedure as described above was employed, with air replacing the FC-40. A simple stability test was performed using FITC (as described in section **2.2.3**), and the results are shown in **Fig. 2.9**. The air barrier was easily loaded into the barrier region, and the air barrier initially appears to effectively separate the two cell culture chambers **Fig. 2.9(a)**. However, after only a few hours, small pockets of water are observed forming in the air barrier channel. Additionally, the width of the air phase in the barrier appears to shrink over time, as evidenced by the increase in thickness of the interface between the air and channel walls over time. Thus, unlike the FC-40 oil barrier, the air barrier does not remain stable over time as required for many cell culture applications; furthermore, multiple trials of the stability test indicate its degradation is not predictable. This behavior of air in the PDMS-based microfluidic device is most likely a consequence of the permeability of PDMS to air (Kang et al., 2008; Merkel et al., 2000). For a static air barrier, the gas phase is constantly leaking out of the barrier channel and into the solid PDMS. Eventually, enough air is removed from the barrier to allow the aqueous phases from each culture chamber to "squeeze" into the barrier region, forming water droplets between the air phase and the glass substrate. The loss of additional gas into the PDMS will result in complete barrier failure, allowing the two cell culture chambers to freely interact. As a result, air is not suitable for use in the static PDMS-based microfluidic platform over an extended time period. However, the interfacial tension between water and air is high enough to achieve the basic working mechanism of the "liquid" barrier platform; thus, the possibility of using air with devices made of materials that are not gas permeable or employing air in a dynamically operated barrier is feasible, although these situations were not explored.

Another fluid tested in the static oil barrier platform was FC-40 mixed with a surfactant. The presence of the surfactant served to reduce the surface tension between the aqueous and oil phases by roughly an order of magnitude. Again, a static oil barrier was loaded, this time using the low surface tension FC-40 + surfactant mixture. The barrier was quickly observed to be unstable; the addition of extra media or hydrostatic pressure in the culture chamber reservoirs resulted in leakage of water into the barrier region. Although the loading procedure can result in variability in barrier stability from device to device, creating a stable static oil barrier using FC-40 + surfactant was significantly more difficult than when using standard FC-40. This behavior is expected because as seen in Eq. (2.2), the curvature of the interface is inversely proportional to the interfacial tension for a given pressure drop. That is, for two systems with interfaces under the same pressure differential, the system with the lower interfacial tension will have a larger interface curvature (smaller radius of curvature). Close examination of the confocal microscope images for the 125 μL/min case (standard FC-40) in **Fig. 2.6(e)** reveals that the radius of curvature in the vertical dimension is approximately half of the height of the microgroove. Increasing the oil flow rate above 125 μL/min resulted in an unstable oil barrier; thus, we can assume that the maximum sustainable pressure differential in our oil/water system is limited by a minimum radius of curvature with a value of about half of the limiting geometric dimension, which in this case is the height of the microgroove. Additionally, the radius of curvature of the static oil barrier in **Fig. 2.6(a)** is slightly greater than an order of magnitude larger than the radius of curvature for the 125 μL/min oil flow rate scenario. Given that the addition of surfactant to the FC-40 reduces the interfacial tension by an order of magnitude and assuming that the interface curvature scales linearly with the interfacial tension, we would expect that even a static oil barrier formed with FC-40 + surfactant would be relatively unstable as the radius of curvature would be near its above described minimum limit. This prediction is consistent with our experimental observation and indicates that the interfacial tension between two fluid phases should be a primary concern when designing microfluidic barrier platforms like those described here.

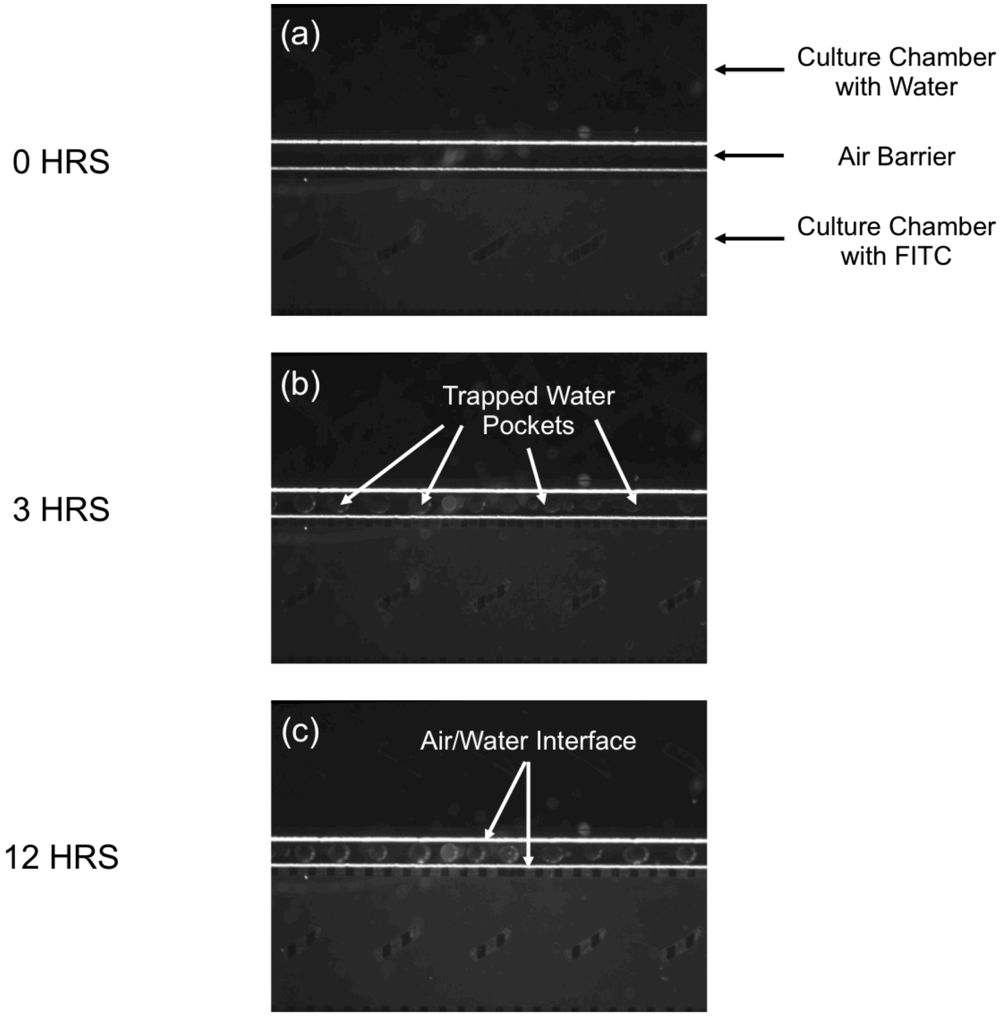

Figure 2.9: Evolution of the static air barrier over time. **(a)** Initially, the air barrier is stable and effectively separates the two aqueous phases. Note that the out-of-focus smudges are aberrations associated with imaging, not physical features. **(b)** After 3 hours, trapped water pockets are observed in the air barrier region, likely trapped between the glass substrate and the air phase. **(c)** After 12 hours, the air/water interface appears thicker, indicating a reduction in the volume of air in the barrier region. Also, the trapped water pockets have increased in size.

2.2.4 Transfection of Hippocampal Neurons and Observation of Synaptic Contact

Neuronal Cell Culture Protocols and Transfection Procedure

To demonstrate the usefulness of the FC-40 oil barrier platform for biological applications, primary hippocampal neurons were transfected separately with different fluorescent proteins in each culture chamber. Before use in biological study, all microfluidic oil barrier devices were sterilized under UV radiation in a laminar flow hood for 1-2 hours. After sterilization, the cell culture chambers were coated with 1 mg/mL poly-L-lysine (PLL) (Sigma-Aldrich, St. Louis, MO) in 0.1 M borate buffer (pH 8.5) for 12 hours in an incubator at 37°C. Excess PLL was removed from the chambers by flowing sterilized DI water through the channels for ~2 hours. The freshly coated chambers were then filled with B27-supplemented Neurobasal^{TM} media (GIBCO^{TM} Invitrogen, Carlsbad, CA) (neuronal media). After waiting 20-30 minutes for equilibration, hippocampal neurons isolated from dissected brains of E19 rat embryos (Goslin, K., Asmussen, H., Banker, 1998) were loaded into the FC-40 valve device (50,000 cells per culture chamber) at a density of $5x10^5$ cells/mL of neuronal media. Note that no oil was present in the middle channel at this point. The cells were allowed to attach to the PLL coated glass substrate of the cell culture chambers by incubating at 37°C with 5% CO_2 for 3 hours. After attachment, ~300 µL of B27-supplemented Neurobasal^{TM} media that had been conditioned for 24 hours over a confluent monolayer of glial cells (glia-conditioned media) was added to the inlet reservoirs of each culture chamber; about half of that volume was added to the outlet reservoirs to slow down the flow rate. The glia-conditioned media was replenished every 36 hours, along with the removal of the waste media collected in the outlet reservoirs.

Alternatively, in an effort to increase transfection efficiency, a co-culture of glia and neurons in the same device was also implemented by employing a four-chamber oil barrier device (Majumdar et al., 2011; M. Shi et al., 2013). First, the four-chamber devices were prepared for co-culture by using UV sterilization and coating with PLL as described above. The coated four-chamber devices were then equilibrated using Minimum Essential Medium (MEM) (Invitrogen, Carlsbad, CA) containing 10% horse serum and 0.6% glucose (glia culture media) for 20-30 minutes. Then, glia that were isolated from 2 day old rat pup brains (Goslin, K., Asmussen, H., Banker, 1998) were loaded into the two outermost culture chambers by adding 50 μL of glial cell suspension into the inlet of each chamber (25,000 cells/chamber). The devices were incubated at 37°C for 2 hours to permit cell attachment, after which they were filled with 400 μL of glia culture media and incubated for 4-5 days until confluence was achieved. Then, neurons were loaded into the two inner culture chambers using the above-described procedure. To ensure that media flowed from the glial chambers into the neuronal chambers after loading the neurons, 400 μL of fresh neuronal media was added to the glial reservoirs while 200 μL of the same media was added to each neuronal reservoir. This was repeated every 36 hours, along with the removal of waste media.

For both two-chamber and four-chamber oil barrier devices, after 3-7 days in culture neurons in each chamber were transfected with GFP and mCherry cDNAs using a modified calcium phosphate method (Zhang, Webb, Asmussen, & Horwitz, 2003). First, a static oil barrier was loaded as described previously. Note that special care had to be taken to keep the FC-40 oil at 37°C (the temperature of the incubator) as we observed that thermal expansion of the oil as its temperature increased from room temperature to 37°C resulted in oil leakage into the cell chambers. To accomplish this, the FC-40, syringe, and syringe tips were heated in the incubator before loading the oil; concurrently, the device was placed on a hot plate just above the incubator temperature (~39°C) while loading the oil to maintain a stable temperature. Note that in the four-chamber oil barrier platform, FC-40 was only loaded in the channel separating the two neuronal chambers. After a stable oil barrier was loaded, 50 μL of transfection mixture containing either GFP or mCherry cDNAs (3-6 μg each) were added to the two inlet reservoirs. A drop of culture media was added to the waste reservoirs after 10-15 minutes to reduce the fluid flow, and the device was placed in a 37°C incubator for 1 hour. The channels were then washed with HEPES-buffered solution (HBS) (pH 7.15) for an additional hour, after which 300 μL of fresh glia-conditioned B27 Neurobasal^{TM} culture media was added to each inlet reservoir. Finally, by releasing the AACO clips and injecting culture media into the inlet tubing of the middle oil channel, the oil barrier was removed by forcing the FC-40 out of the outlet tubing.

Confocal Microscopy Visualization and Dynamic Observation of Synaptic Contact

The separation of the two culture chambers by the oil barrier was verified by analyzing transfected neurons using confocal microscopy. First, neurons were prepared for live-cell imaging after 12-13 days in culture by replacing neuronal media with 50 mM HEPES containing B27-supplemented Neurobasal^{TM} media without phenol red, pH 7.4. Imaging was performed on the Quorum WaveFX spinning disk confocal system. Cells were imaged using a 10X ADL objective (NA 0.25), a Plan Fluor 40X objective (N.A. 1.3), or a PlanApo 60X TIRF objective (NA 1.49). GFP and mCherry images were obtained by exciting with 491 nm and 561 nm laser lines, respectively (Semrock, Rochester, NY). The resulting images were then analyzed to ensure that no cells were transfected with the inappropriate fluorescent protein.

By transfecting neurons in one chamber with the pre-synaptic marker mCherry-synaptophysin and neurons in the other chamber with GFP, synaptic contact between neurites originating from different culture chambers could be observed. The confocal microscope system was used to obtain two images (one each for mCherry-synaptophysin and GFP) at a given location within a culture chamber. For high magnification images of synapses, a PlanApo 60X TIRF objective (NA 1.49) was used. Images were acquired every 15 minutes for 12 hours using MetaMorph software. The regions along neurites where synaptic contact occurred were then determined by overlaying the images. In addition, the dynamic formation of synapses over time could be visualized using the time-lapse sequence of overlays. Note that both standard two-chamber oil barrier devices and four-chamber devices with glial co-culture were used to investigate synapse formation between the separately transfected neuronal populations.

The results of a typical transfection with GFP and mCherry tagged DNAs are shown in **Fig. 2.10**. Hippocampal neurons in each chamber were transfected with the appropriate fluorescent protein; more importantly, no neurons in the GFP chamber were transfected with mCherry, or vice-versa, indicating that the oil barrier was effective at separating the two chambers. The successful transfection of neurons with GFP and mCherry without any crossover indicates device functionality similar to previous successful microfluidic neurobiology platforms (Gao et al., 2011; Majumdar et al., 2011; M. Shi et al., 2013).

The successful separate transfection of primary hippocampal neurons with different colored fluorescent proteins allows for dynamic observation of synaptic contact between neurites originating from different culture chambers. In addition, by using the pre-synaptic marker mCherry synaptophysin instead of mCherry in one of the chambers, the location of potential synapses can be easily identified within a culture chamber. In **Fig. 2.10(c-e)**, an area of the cell culture chamber is presented that showcases the location of neurites originating from the two culture chambers. By examining the overlay of the images, the locations at which synaptic contact occurs can be readily identified. A sequence of images can also be captured over time, allowing for the observation of the dynamic formation of synapses. This functionality provides the potential to study molecules important to central nervous system synaptic development.

Again, both two-chamber oil barrier devices (using glia conditioned media) and four-chamber devices that contained a co-culture of glia and neurons were successfully used to separately transfect two different neuronal populations and observe synaptic contact. The four-chamber design was employed to increase the transfection efficiency, as improved transfection efficiency using neuron-glia co-culture has been previously demonstrated in the literature (Majumdar et al., 2011). In addition, the four-chamber platform could be useful for applications in which the interactions between several different cell types are to be investigated.

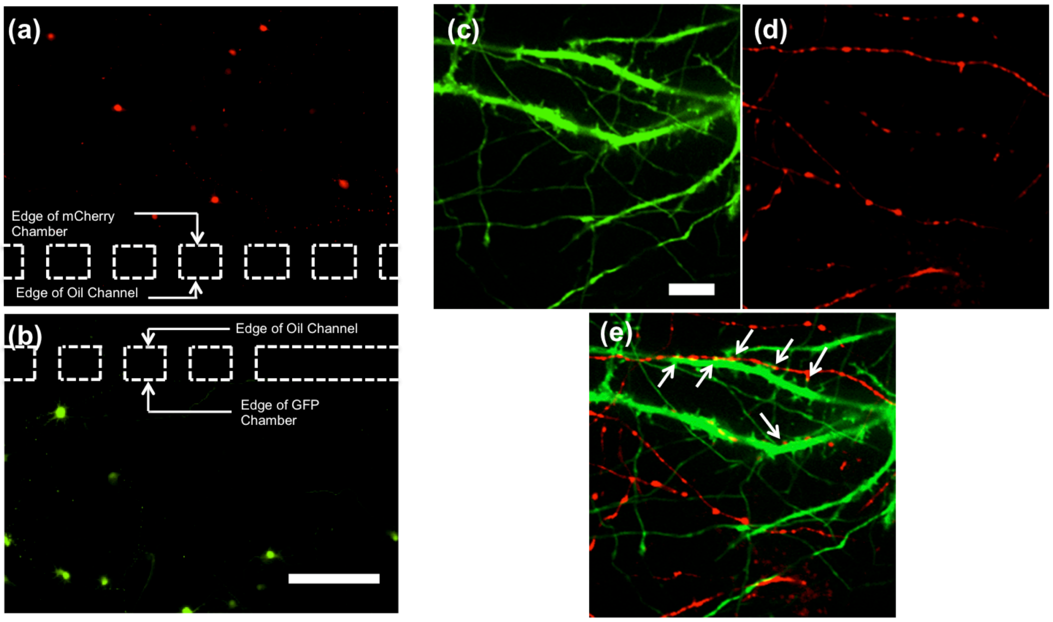

Figure 2.10: Separate transfection of primary hippocampal neurons with fluorescent proteins using the static oil barrier platform and the subsequent dynamic observation of synaptic contact. **(a-b)** Neurons were transfected with mCherry in the top panel and GFP in the bottom panel. The dashed lines illustrate the location of the microgrooves connecting the respective chambers to the oil channel. Note that no neurons in the mCherry chamber were transfected with GFP, or vice-versa. The scale bar is 200 µm. **(c-e)** Two images using different fluorescence filters were obtained at the same location, demonstrating contact between neurons from the adjacent chambers. Neurons in one chamber were transfected with **(c)** GFP, while neurons in the other chamber were transfected with **(d)** mCherry synaptophysin. **(e)** An overlay of the two images allows the locations of synaptic contact to be identified. The areas indicated by the white arrows are observed synaptic junctions. The scale bar is 10 µm for **(c-e)**.

2.2.5 Neuron Staining Using Cell Tracker Dyes

In addition to transfection with fluorescent proteins, cell staining with commercially available CellTracker dyes was also used to visualize hippocampal neurons in culture. The CellTracker dyes differ from the transfection proteins in that these molecules are much smaller and can penetrate the cell membrane more easily, resulting in staining of nearly 100 percent of the cells in culture. Previously, when staining hippocampal neurons in separate chambers with different colored CellTracker dyes using the solid-PDMS valve barrier device, crossover of the fluorescent molecules was often observed if no special treatment was used to create rounded corners on the microgrooves. Indeed, neurons in a chamber that were treated with CellTracker Red exhibited both red and green staining, indicating that the CellTracker Green molecules used in the other culture chamber leaked through the pressurized valve barrier.

To determine the effectiveness of the static oil barrier platform in blocking the transport of these smaller molecules between culture chambers, cells in each chamber were stained with CellTracker GreenCMFDA and RedCMTPX (Invitrogen, Eugene, Oregon) fluorescent dyes. As in the transfection protocol, primary hippocampal neurons were cultured for 3-7 days in the microfluidic culture chambers. Then, after loading a stable static oil barrier, 50 μL of fresh glia-conditioned B27 Neurobasal culture media with CellTracker Red (final concentration of 0.5 μM) was added to one inlet reservoir; the same volume of CellTracker Green was added to the other inlet. The device was allowed to incubate at 37°C for ~1 hour, after which the dyes were flushed using fresh glia-conditioned B27 Neurobasal culture media for 1 hour. This was followed by careful removal of the oil barrier and addition of Neurobasal media containing B27-supplemental without phenol red with 50 mM HEPES, pH 7.4 media. As a comparison of device performance, the protocol was repeated with a solid-PDMS valve barrier microfluidic device fabricated using previously detailed procedures (Gao et al., 2011).

A comparison of the performance of the static oil barrier and solid-PDMS valve barrier microfluidic devices is presented in **Fig. 2.11**. Unlike the solid-PDMS valve barrier device, no crossover of CellTracker dyes was observed when the static oil barrier was used to separate neuronal populations during staining. This result indicates that the oil barrier design could provide a better fluidic seal than the standard solid-PDMS valve barrier platform. Concurrently, no observed leakage of the small CellTracker dye molecules validates the claim that no significant diffusion occurs across the ultra-thin residual aqueous layer that may be trapped below the oil barrier in the middle channel. Thus, the microfluidic oil barrier platform presented here is an effective option for applications in which small molecules are used to treat separated cell populations.

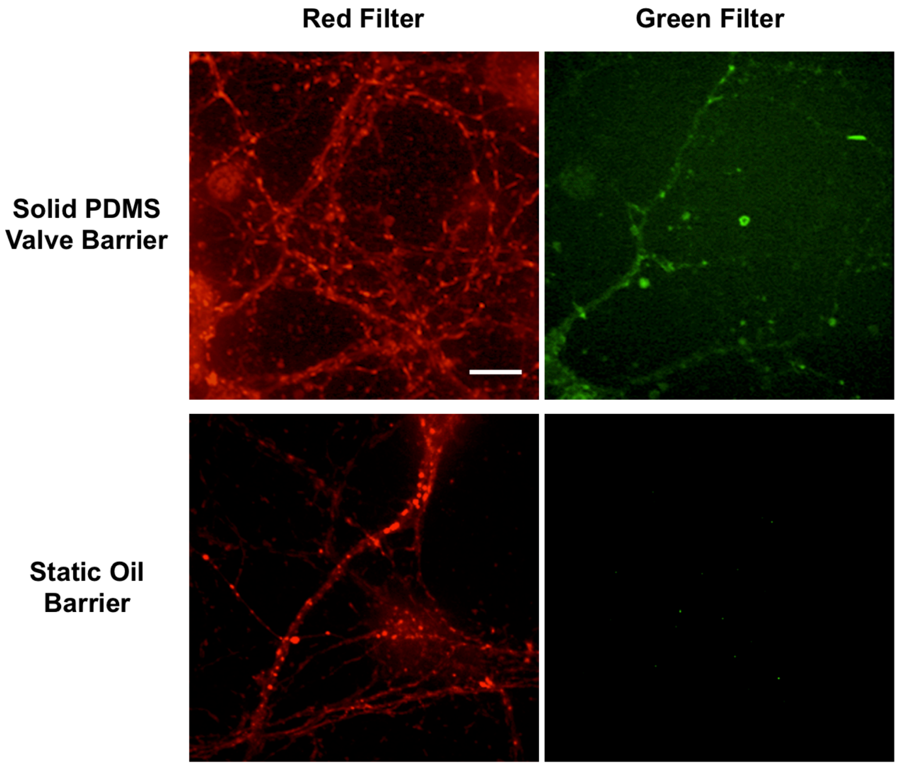

Figure 2.11: Using CellTracker Red and Green to compare leakage of the solid-PDMS valve barrier microfluidic platform to the static oil barrier device. For each device, neurons in one culture chamber were stained with CellTracker Red, while neurons in the opposite chamber were stained with CellTracker Green. In the top panels, confocal images were obtained at the same location in the culture chamber treated with CellTracker Red using both red and green filters. The results indicate that cell structure was stained with both CellTracker Red and Green, suggesting leakage of CellTracker Green across the solid-PDMS valve barrier. However, in the bottom panels, images taken in the chamber treated with CellTracker Red show cell structure stained red only; thus, the oil barrier appears to more effectively block the transport of small CellTracker molecules between culture chambers. The scale bar is 10 μm.

2.3 Three-dimensional Membrane Valve Device

2.3.1 Motivation

Although the solid-PDMS valve barrier platform and the oil barrier microfluidic device are useful tools, both are limited to two-dimensional cell culture studies in the barrier region, as the maximum allowed height of the PDMS barrier or microgroove gap while still maintaining proper valve function is ~20 μm. On the other hand, by suspending cells in a gel mimicking the extracellular matrix (ECM), a three-dimensional cell culture system is achieved that more closely resembles the *in vivo* cellular microenvironment (Tibbitt & Anseth, 2009). However, this cannot be achieved by simply injecting the cell culture chambers of the two-dimensional devices with a gel matrix; the cross-sectional area of the microgroove interface separating the cell culture chambers is too small to be truly considered three-dimensional as cells can sense and react to solid boundaries. Dimensions on the order of 100 μm are likely necessary to enable cell migration and interaction in three dimensions without unwanted influence from the channel walls and substrate. An additional difficulty in translating a cell culture system from two- to three-dimensions is achieving sufficient mass transport throughout the hydrogel matrix. The use of passive diffusion for perfusion of the nutrient-rich media necessary for sustaining cellular metabolic activity results in size-limitations for three-dimensional constructs, and the accumulation of waste products can be detrimental to cell viability and phenotypic expression (Cuchiara, Allen, Chen, Miller, & West, 2010; Ishaug et al., 1997). In fact, a decrease in metabolic density with distance from the nutrient source is often observed in artificial tissue scaffolds, with cells farther away becoming less active or even necrotic (Cuchiara et al., 2010). Thus, the development of three-dimensional cell culture schemes requires additional considerations when compared to two-dimensional systems.

We have modified our original valve-enabled cell culture platform to increase compatibility with three-dimensional cell co-culture. This was achieved by using a thin PDMS membrane that can be pressurized from an above control chamber to separate a large cell culture chamber into multiple smaller chambers. In one configuration, a single-membrane valve is used to separate one large chamber into two separate cell culture regions. Although this general microfluidic valving technique has been demonstrated before (Unger et al., 2000), our membrane valve design is effective at separating microfluidic channels an order of magnitude taller (~100-300 μm) than previously demonstrated devices. This added capability enables three-dimensional cell co-culture in a microfluidic platform while still providing all of the essential functionalities of the original two-dimensional valve-enabled cell culture device. In an alternative design, two membrane valves are employed to separate a large chamber into three separate regions: two large media channels and one smaller central channel in which cells embedded in a three-dimensional gel matrix are loaded. With this double-membrane valve scheme, a large cross-sectional area of the cell-laden hydrogel is exposed to the media channels after the valves are lifted, enabling enhanced media flow and nutrient transport within the gel. Here we present the fabrication and operational details of both of these platforms, as well as a parametric finite element modeling analysis that can be used to guide the design of future devices dependent upon specific application requirements. Finally, experimental results demonstrating the capabilities of each microfluidic system are showcased.

2.3.2 Membrane Valve Fabrication and Operation

The basic design features of the membrane valve device are shown in **Fig. 2.12**. The bottom device layer is either a thick PDMS film or an open channel thin-film containing a large cell culture chamber 100-300 μm tall that is connected to two inlet and two outlet channels. An upper pressure control chamber (~200-500 μm wide x 200 μm tall) is used to inflate a ~10 μm PDMS membrane sandwiched between the two layers until the membrane touches the glass substrate, effectively separating the large cell culture chamber into two separate chambers (**Fig. 2.12(b)**). The same design ideas apply to the double-membrane valve device (**Fig. 2.12(c-d)**), with the only difference being the presence of two pressure control chambers and three separate channels when the valve is actuated. Note that both pneumatic and hydraulic pressure can be used to pressurize the upper control chamber.

Fabrication of the membrane valve device involves the separate fabrication of each of the three layers. As mentioned previously, the bottom layer can be either an open-channel thin PDMS film or a standard thick PDMS layer. For the first case, the open-channel thin film layer is formed by sandwiching degassed PDMS between the SU-8 mold defining the channel features and a fluoropolymer coated polyester sheet. After curing the PDMS, the polyester sheet is used to transfer and plasma bond the PDMS thin film to a glass coverslip. For the second case, standard soft lithography methods are employed to make a 1-2 mm thick PDMS layer with the imprinted channel features that is then bonded channel side up to a glass coverslip. Next, the upper pressure control chamber is fabricated using standard soft lithography. PDMS is poured over an SU-8 mold and cured; the resulting piece is peeled from the mold, trimmed to the proper dimensions, and inlet/outlet holes punched in the appropriate areas. Finally, the 10 µm thick PDMS membrane is formed by spin-coating PDMS at 4000 RPM on another fluoropolymer coated polyester sheet. After curing, the membrane is plasma bonded to the upper pressure control chamber. Then, the control chamber/membrane combo is plasma bonded to the coverslip/bottom PDMS film layer. Tubing supports and tubing are finally added to the pressure control chamber to complete the device fabrication. (Note that further information regarding the attachment of tubing supports and tubing are described in Chapter III, while additional details regarding the fabrication of thin-films and membranes can be found in Chapter IV.)

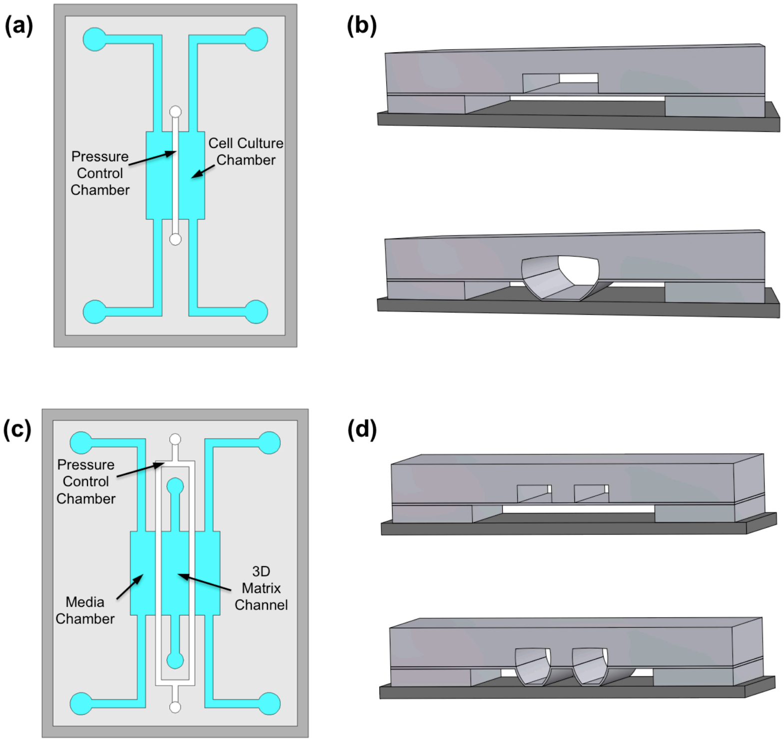

Figure 2.12: Schematic and operating principle of the membrane valve device design. **(a)** Top-view of the single-membrane valve showcasing the location of the cell culture chamber and pressure control chamber. **(b)** Cross-sectional view of the membrane valve device in the unpressurized (upper panel) and pressurized states (lower panel). **(c-d)** Identical views for the double-membrane valve device.

In addition to the standard fabrication described above, a slight modification must be made to the device to ensure proper operation. As mentioned, the height of the cell culture chamber is relatively large (100-300 μm). As a result, when the membrane is deflected downward to the substrate, a “sieve valve” effect occurs in which small openings remain at the corners formed by the deflected membrane and the chamber wall. To remove this undesirable leakage point, the channel walls must be angled to enable the formation of a tighter seal between the membrane and the channel wall (see **Fig. 2.13(a)**). The angled sidewalls required can be achieved by simply manually removing the edge of the wall using a sharp scalpel. Although this method is rudimentary and results in varying rugged edges at the channel wall, it is effective at fixing the leakage problem. Alternatively, by using a silicon dioxide mask (patterned using a buffered oxide etch) and KOH etching, a silicon mold can be fabricated in place of the SU-8 mold. The nature of wet KOH etching on silicon wafers with <100> orientation results in sidewalls with a 54.7° beveled edge. The etched silicon mold can then be used to fabricate the bottom cell culture chamber layer. Although mold fabrication using this technique is more time-consuming than the manual scalpel method, the resulting PDMS channels are significantly easier to reproduce at a functional quality. A summary of both the SU-8 and KOH etched silicon mold fabrication protocols are presented in **Fig. 2.13(b-c)**.

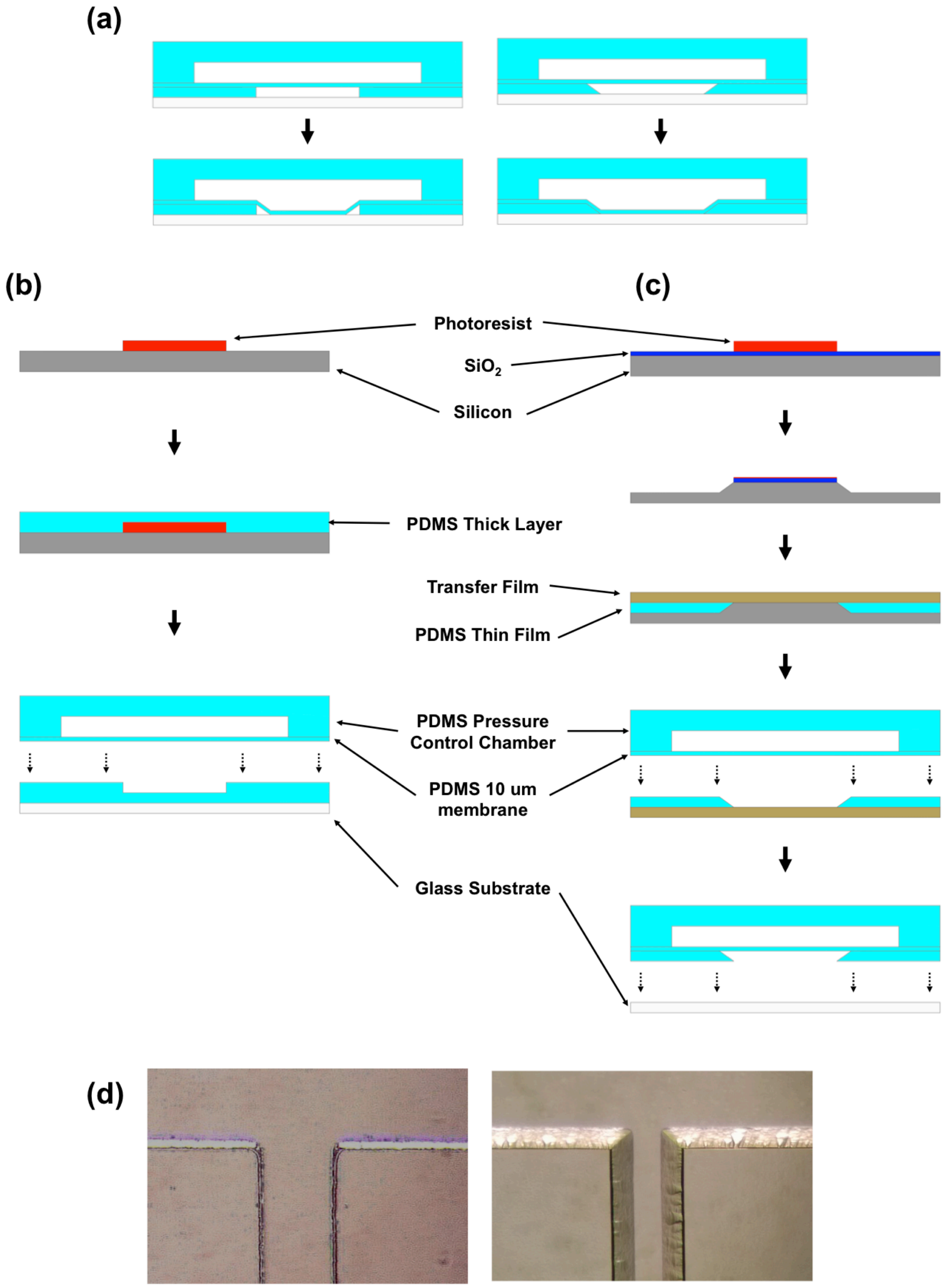

Figure 2.13: Comparison of vertical and beveled channel walls and the fabrication of the membrane valve platform. **(a)** A long-axis cross-sectional schematic view of a membrane valve device with vertical sidewalls shows a "sieve valve" effect upon pressure valve actuation (left panel). The same view for a device with beveled channel walls results in a membrane that conforms better to the sidewalls, creating a better fluidic seal. **(b)** A process flow demonstrates the fabrication steps for a membrane valve system with vertical sidewalls and a thick PDMS bottom layer. **(c)** A process flow demonstrates the fabrication steps for a membrane valve system with angled sidewalls and an open-channel thin PDMS film bottom layer. **(d)** A pair of optical microscope images showcases the difference in vertical (left panel) and beveled (right panel) channel walls.

2.3.3 Finite Element Modeling of the Membrane Valve

In order to better characterize the parameters governing the operation of the membrane valve platform, a two-dimensional finite element model was developed using COMSOL Multiphysics™. The Solid Mechanics physics module was employed to create a to-scale representation of the single-membrane valve device (**Fig. 2.14**). The PDMS domains were modeled using a Poisson's ratio of 0.45, a density of 965 kg/m^3, and Young's modulus values of 1.9 MPa for the thin membrane and 1.8 MPa for the rest of the domain. A pressure boundary condition was applied to the inner walls of the pressure control chamber, and the resulting maximum displacement of the center of the membrane was calculated. Using this model, a parametric study was performed that examined the effects of pressure chamber width (100-500 μm), membrane thickness (5-25 μm), and applied pressure (0.1-100 kPa) on the maximum membrane displacement. The results of this study are presented in **Fig. 2.14(a)**. As intuitively expected, the maximum displacement was observed to increase with increasing pressure chamber width, decreasing membrane thickness, and increasing applied pressure. Additionally, it is worth noting that for a constant membrane thickness and pressure chamber width, the maximum membrane displacement increased linearly with applied pressure. On the other hand, for a given applied pressure and constant value for either membrane thickness or pressure chamber width, the displacement displayed a non-linear dependence on the other geometric parameter. Finally, the data indicate that relatively minor alterations in the membrane thickness or pressure chamber width can produce orders of magnitude changes in membrane displacement. Collectively, these results provide a summary of predictable device performance under a variety of realistic operating conditions.

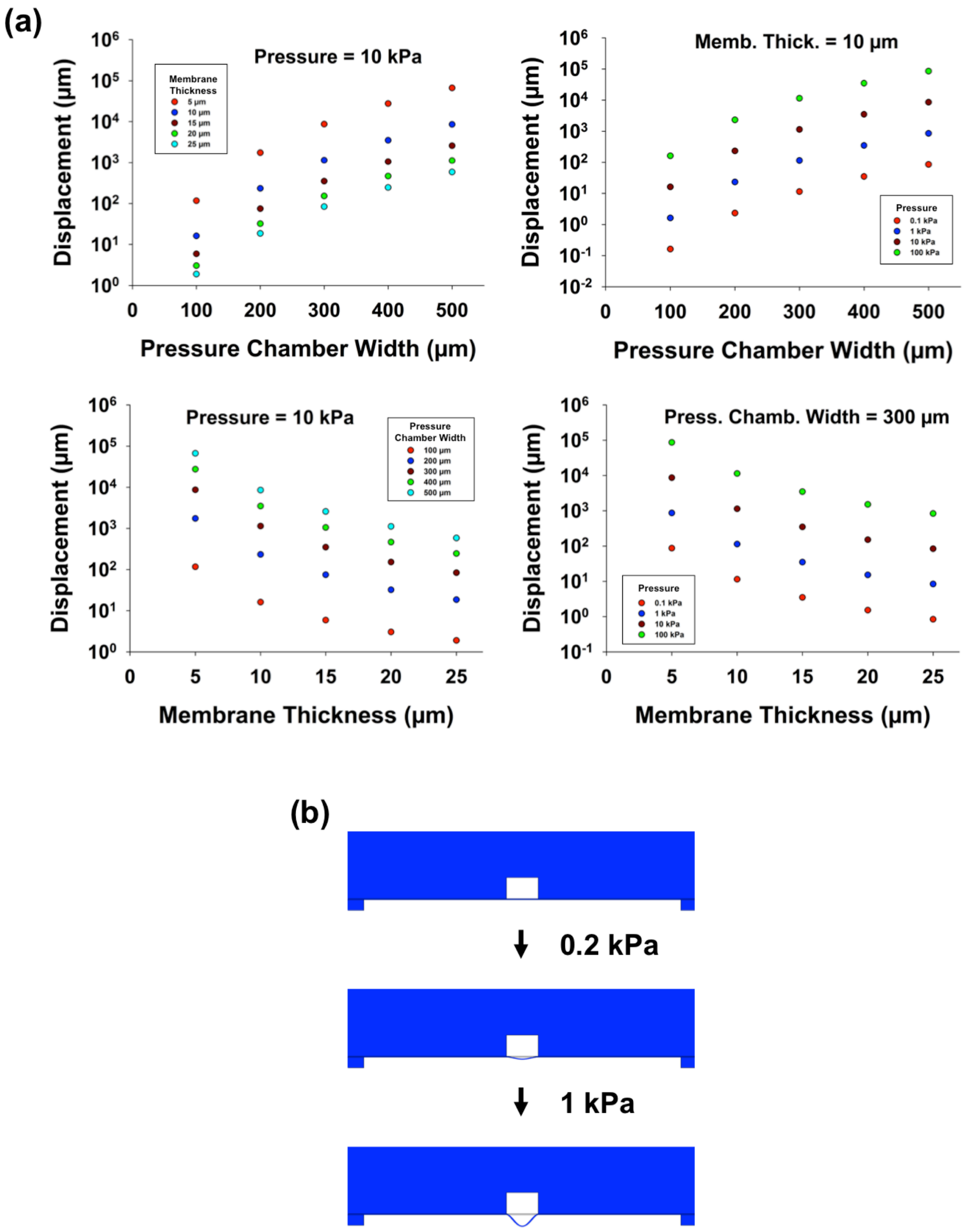

Figure 2.14: Parametric study of the single-membrane valve platform using COMSOL Multiphysics^{TM}. **(a)** Multiple scatter plots showcase the dependence of membrane displacement on pressure chamber width, membrane thickness, and applied pressure. Note the logarithmic scale used for displacement on the y-axis. **(b)** Model visualizations demonstrate the evolution of the membrane displacement with increasing pressure applied to the control chamber. The geometric domain presented here is cropped from the entire domain to better focus on the membrane deformation.

Although the raw data presented in **Fig. 2.14** provide some intuition about device performance, a more thorough analysis is required to develop the results into a more comprehensive set of guidelines for future device design. To accomplish this, an examination of the applicable solid mechanics is useful. First, we consider the governing differential equation for deflections of thin plates (Ventsel & Krauthammer, 2001):

$$D\left(\frac{\partial^4 w}{\partial x^4}+2\frac{\partial^4 w}{\partial x^2 y^2}+\frac{\partial^4 w}{\partial y^4}\right)=p \tag{2.3}$$

Here w is the displacement of the thin plate, p is the loading pressure, and D is the flexural rigidity given by

$$D=\frac{Eh^3}{12(1-\nu^2)} \tag{2.4}$$

where E is Young's modulus, ν is Poisson's ratio, and h is the thickness of the plate. Now, for the special case of a circular plate with radius a and constrained on its perimeter, the solution for the maximum displacement in the center of the membrane is given by (Schomburg, 2011)

$$w_0=\frac{3}{16}\frac{a^4}{h^3}\left(\frac{1-\nu^2}{E}\right)p \tag{2.5}$$

In the finite element model presented earlier, the two-dimensional geometric domain analyzed can be considered approximately equivalent to a central plane situated along the diameter of the circular plate described in Eq. (2.5), where the radius a corresponds to the pressure chamber width. Thus, the maximum displacement for a rectangular plate (as employed in the membrane valve) will take the same form as the solution for the maximum displacement of a circular plate. With this in mind, closer inspection of Eq. (2.5) reveals that the maximum displacement is directly proportional to the pressure and the "width" dimension to the fourth power, while it is inversely proportional to the cube of the membrane thickness. The linear dependence on pressure and non-linear relationship with the geometric dimensions presented here are consistent with the previous data presented in **Fig. 2.14**, further suggesting the validity of the model. More importantly, this solution provides a potential means of condensing the data shown in **Fig. 2.14** into a useful set of design guidelines for the membrane valve platform. To explore this idea, the displacement was plotted against the pressure chamber width to the 4th power divided by the cube of the membrane thickness. As shown in **Fig. 2.15**, well-behaved dependence appears for each applied pressure value that can be used to clearly predict the membrane valve device performance for a given set of parameters. For example, suppose the goal was to design a membrane valve to separate a chamber 300 μm tall, and the rupture pressure of the system is known to be 10 kPa. From **Fig. 2.15**, the relationship between pressure chamber width and membrane thickness required to achieve this functionality can be determined. Thus, the creation of future iterations of the membrane valve system can make use of these results to guide the beginning of the design process.

Note that Eq. (2.5) is a classic solution for the bending of a thin circular plate, and it is often applied to situations in which small deflections are to be analyzed. Obviously in the case of the membrane valve, the deflection can become rather large relative to the membrane thickness. In this scenario, the relationship among displacement, pressure chamber width, membrane thickness, and pressure could be different (e.g. $w_0 \alpha p(a^2/h)$ (Schomburg, 2011)). In addition, other factors not considered in this model could affect device performance in the real world, particularly the interaction of the membrane with the glass substrate. Although studying the deformation of the membrane after making contact with the substrate would be interesting and undoubtedly elucidate additional information that could be used to improve device performance, the application of a contact boundary condition was beyond the modeling capabilities of the COMSOL Multiphysics^{TM} package available to us and thus, was not pursued. Nonetheless, the model presented here is based on well-established solid mechanics theory and accurate values for the material properties of PDMS, and the resulting data presented in **Fig. 2.15** agree well with the solution provided in Eq. (2.5). Thus, within the realistic range of parameters likely to be encountered in the use of a membrane valve device, the model can be assumed to be a useful tool in predicting operational performance.

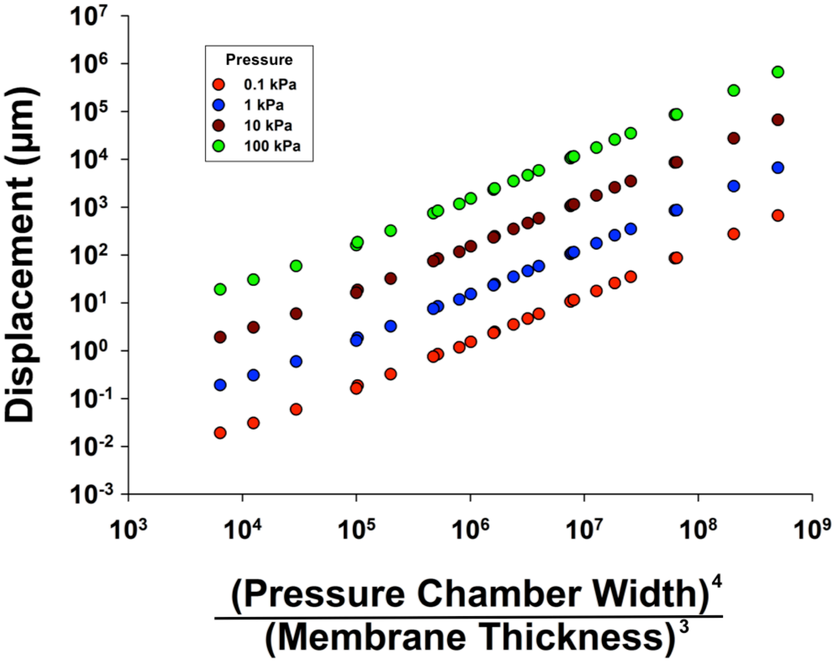

Figure 2.15: Summary of a parametric study of displacement in the membrane valve system for use in providing guidance for future designs.

2.3.4 Membrane Valve Demonstration

To demonstrate the operating principle of the device, a two-chamber membrane valve device was fabricated as described above using the open-channel thin film bottom layer design and the scalpel method of achieving beveled channel walls. Water was injected into the pressure control chamber to deflect the membrane to the glass substrate, separating the cell culture chamber into different smaller channels. Colored dye was then introduced into one of the new channels and allowed to diffuse into the entire chamber. After some time, the pressure was released and the dye began diffusing into the opposite side of the cell culture chamber. As exhibited in **Fig. 2.16**, the device effectively separated the culture chamber when pressurized while still allowing free transport of the dye after pressure was released. These results indicate the viability of the two-chamber membrane valve design for future use in three-dimensional cell culture studies.

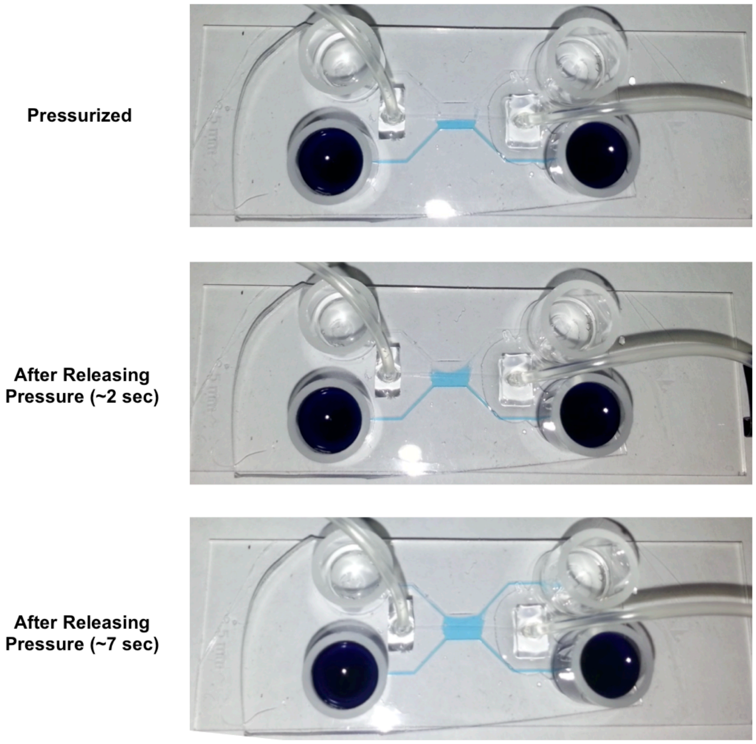

Figure 2.16: Demonstration of the single-membrane valve device. Dye was loaded into the lower channel of a pressurized device (upper panel). Just after releasing the pressure from the pressure control chamber, the dye began diffusing into the upper channel (middle panel). After ~7 sec, the dye covers nearly the entire cell culture chamber (bottom panel).

An additional set of tests was performed using a double-membrane valve platform. In these experiments, KOH etching was performed to produce a silicon mold with beveled edges. This mold was then used to produce a double-membrane valve device with a thick PDMS film bottom layer using the fabrication protocol detailed in the above section. Using this system, the colored dye test performed on the two-chamber membrane valve was repeated. For this case, the two actuated valves separated the large chamber into two large outer chambers and a smaller central channel, which was then filled with colored dye. As shown in **Fig. 2.17(a)**, the membrane valve was effective at preventing leakage of the dye into the outer chambers until the pressure was released, after which the dye freely flowed into the entire larger chamber area within a few minutes. A supplementary experiment was carried out that examined the efficacy of loading a three-dimensional gel construct into the central channel of a pressurized double-membrane valve system and investigated the resulting flow perfusion through the established matrix. After pressurizing the device, a high concentration collagen gel mixture containing 800 nm diameter polystyrene beads was loaded into the central channel. The gel was then cured in a humidified oven at 37° C for 30 minutes (more information about the collagen gel fabrication protocol can be found in Chapter III). The first panel of **Fig. 2.17(b)** is a microscope image of the polymerized gel in the central channel of the still pressurized membrane valve device. From this image, the uniform distribution of the polystyrene beads indicates a successful gelation step. The pressure was then released from the pressure control chamber, and the resulting change to the three-dimensional matrix is shown in the second panel of **Fig. 2.17(b)**. As seen here, the gel does slightly spread out after pressure release, likely as a result of the outer edges of the gel sticking to the membrane as it retracts back to the roof of the chamber. Nonetheless, the structural integrity of the majority of the gel appears to be intact. Finally, to test perfusion through the gel, colored dye was added to the bottom chamber and tracked as it passed through the gel barrier region. As exhibited in **Fig. 2.17(b)**, the dye flowed nearly uninhibited through the gel, indicating this platform could be an effective way of achieving adequate nutrient/waste exchange in a three-dimensional cell culture system. Altogether, these two experiments demonstrate the potential capabilities of the double-membrane valve platform.

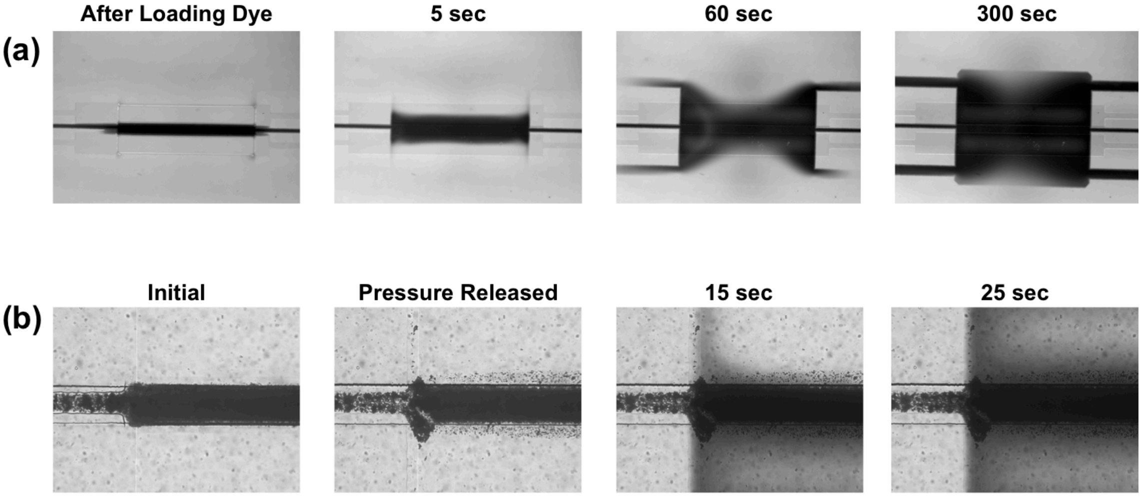

Figure 2.17: Experimental validation of the three-chamber membrane valve system. **(a)** A series of optical microscope images shows the progression of colored dye initially confined to a central channel formed by deflected membrane valves (leftmost panel) at various time points after the valves were opened. **(b)** A series of optical microscope images showcase a collagen gel/nanoparticle mixture after polymerization (first panel), after releasing the membrane valves (second panel), and at two time points after loading colored dye into the bottom chamber (third and fourth panels).

2.4 Summary

We have developed a microfluidic cell co-culture platform featuring a reversible liquid fluorocarbon (Fluorinert FC-40) barrier that enables separate culture and treatment of cell populations before and/or after allowing the populations to interact with one another. The physical capabilities of the device were characterized, showcasing that both the stability of the barrier and the maximum pressure drop across the oil/water interface were equal to or greater than that of similar microfluidic platforms reported in the literature. The biological relevance of the device was demonstrated by successful culture and separate transfection of primary hippocampal neurons with different colored fluorescent proteins, allowing for dynamic observation of synaptic contact. In addition, the liquid fluorocarbon oil barrier design appears to provide a greater fluidic seal between culture chambers, and it exhibits greater biocompatibility than previous solid-barrier based platforms. The improved functionality provided by the oil barrier microfluidic cell co-culture platform makes it well-suited for probing cellular and molecular interactions in cell biology studies.

In addition, we have demonstrated both single- and a double-membrane valve designs that are modified versions of the valve-enabled microfluidic co-culture platform and are compatible with true three-dimensional cell co-culture. A finite element model was developed and a parametric study performed using the model. Based on theoretical analysis of the study results, a set of design guidelines for future membrane valve systems was successfully established. Also, the valving ability of both the two-chamber and the three-chamber membrane valve devices was demonstrated using colored dyes. Additionally, the loading of a three-dimensional gel matrix into a double-membrane valve device was performed, and the resulting flow perfusion through the gel construct was shown. Together, both of these new iterations of the valve-enabled cell co-culture microfluidic platform will enable future cell biology investigations that more closely mimic the *in vivo* cellular environment.

CHAPTER 3

MICROFLUIDIC LIGAND TRAP FOR SELECTIVELY BLOCKING EXCHANGE OF MOLECULES IN CELL-CELL INTERACTIONS

3.1 Motivation

Communication and interaction among cells is an essential component of the growth, development, and maintenance of multicellular organisms (Skinner, 1991). Cell-cell communication may occur through direct contact or via soluble factors through paracrine, endocrine, or autocrine signaling (Lodish et al., 2000). For all modes of extracellular signaling via soluble molecules, a secretory cell produces a signaling molecule called a ligand that binds to a receptor protein on the surface of a target cell; this interaction between ligands and receptors causes a conformational change in the receptor protein that initiates a sequence of reactions that eventually leads to some type of cellular response (Lodish et al., 2000). Extracellular signaling plays an important role in many biological functions including the control of metabolic processes in cells (DeBerardinis, Lum, Hatzivassiliou, & Thompson, 2008), the growth of tissues in the body (Nelson & Bissell, 2006), the synthesis and secretion of proteins (Rhoads, 1999), and control over the composition of intracellular and extracellular fluids (Peterson, Meggyesy, Yu, & Miller, 1997). Thus, it is not surprising that the study of specific signaling pathways is a fundamental focus of cell biology research. In this type of investigation, researchers are often required to remove specific elements from a signaling pathway to determine the importance of its role in some observed cellular response.

Traditionally, blocking signal pathways has been accomplished using a couple of different methods. First, chemical inhibitors or neutralizing antibodies can be added to the cellular microenvironment to "neutralize" a specific ligand, disrupting signaling pathways that require the molecule. Although this method can effectively block the targeted ligand, other untargeted signaling pathways are often affected as well, as adding a cocktail of chemical inhibitors into a cell culture system modifies the cellular microenvironment (Even-Ram & Yamada, 2005). The second method of investigating signaling pathways employs the technique of gene knockout. In gene knockout, a specific gene(s) responsible for the production of a ligand is modified or removed from a cell or host organism using DNA technology (Brantley-Sieders et al., 2004). However, genes may have multiple functions, reducing the specificity of the technique (Wolfer, Crusio, & Lipp, 2002). Also, gene knockout is relatively time-consuming and expensive, and it also requires the comparison of a wild type and mutant sample, potentially skewing phenotypic expression. Therefore, a method of examining specific extracellular signaling pathways without the restrictions imposed by traditional methods is clearly needed.

Previously, our lab has demonstrated a microfluidic cell co-culture platform utilizing a nanoporous agarose gel barrier that allows separate populations of cells to communicate via soluble factors alone (Gao et al., 2011). However, the device was incapable of targeting specific signaling pathways via the removal of ligands from the cellular microenvironment. Using this previous design as a template, we have developed a new "ligand trap" device that employs embedded nanoparticles, functionalized with a desired protein receptor, in a semi-permeable collagen gel barrier that serves to selectively remove specific ligand signaling molecules from the microenvironment of a cell population. This new design has been demonstrated with several model ligand/receptor pairs and should eventually be useful for targeting a wide variety of signaling pathways.

3.2 Ligand Trap Design and Fabrication

3.2.1 Operating Principle

The ligand trap device is based upon a previously developed microfluidic cell co-culture platform that uses a nanoporous agarose gel barrier to investigate communication between cell populations via soluble factors alone (Gao et al., 2011). Three primary layers make up the device: (1) a thin glass coverslip that allows for device compatibility with high resolution confocal microscopy, (2) a bottom PDMS channel layer that contains two cell culture chambers and a central channel for the ligand trap, and (3) an upper PDMS pressure control chamber that is used during gel loading. An array of microgrooves connects the cell culture chambers and ligand trap channel in the bottom layer. The flexibility of PDMS allows the roofs of these connecting microgrooves to deform to the glass substrate when hydraulic pressure is applied to the upper pressure control chamber, effectively separating the three chambers. This feature is employed while loading and curing the ligand trap gel mixture in order to contain the gel in the trap channel only. After the device is completely fabricated, cells can be loaded into each of the outer cell culture chambers. The multitude of soluble molecules produced by each cell population over time can freely pass through the semi-permeable gel barrier, with the exception of a specific, targeted ligand. This specific ligand is trapped in the barrier region by its protein receptor, which is attached to nanoparticles embedded in the semi-permeable gel matrix. The use of receptor proteins attached to nanoparticles is necessary, as simply mixing the receptor with the porous gel would result in the receptor being washed away over time. On the other hand, the nanoparticles are large enough to be immobilized in the gel barrier, keeping all of the receptors in the trap channel. The result of this design scheme is the prevention of transport of a targeted molecule between separate cell populations. In this way, specific signaling pathways that depend on the ligand can be disrupted, and the subsequent effects of this disruption on the cell populations can be investigated.

3.2.2 Fabrication

Again, as shown in **Fig. 3.1**, the ligand trap device consists of a glass substrate, a bottom channel layer, and an upper pressure control chamber layer. A number of different designs were employed for the bottom channel layer; however, all versions of the ligand trap shared the same basic features. Two cell culture chambers 5 mm (*l*) x 1 mm (*w*) x 100 um (*h*) were separated by a 100 um tall middle "trap" channel that varied between 200 um and 700 um in width. Either a series of connecting microgrooves (similar to those employed in the oil barrier design of Chapter II) or a continuous barrier gap (5 um tall) connected the middle channel with the outer cell culture chambers. The distance between the middle channel and the outer culture chambers was 100 um for all designs. Additionally, a series of support pillars were used in some iterations of the ligand trap, ranging from circular pillars 75 um in diameter to elliptical pillars with radii of 150 and 75 µm. The pressure control chamber used was typically 400 um (*h*) x 8 mm (*l*) x 4 mm (*w*). Both the channel and pressure control chamber layers were made using standard PDMS soft lithography as described in Chapter II.

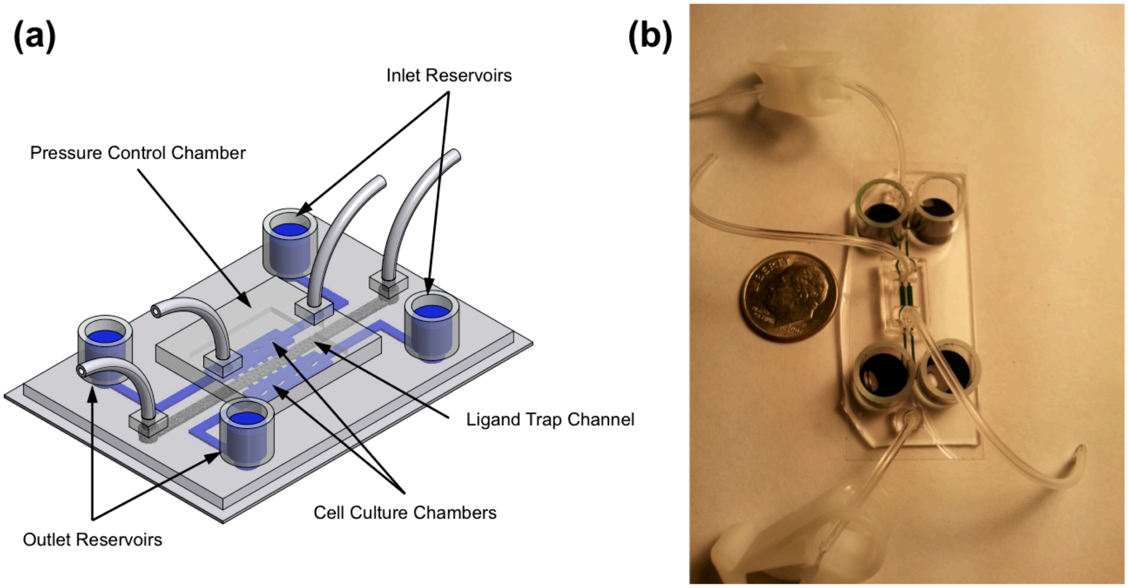

Figure 3.1: (a) Schematic of the ligand trap device and **(b)** a photo of the device with a U.S. dime for scale.

Before assembling the device, a couple of modifications needed to be made to the device components. First, the glass coverslips used for the device substrate (60 mm (*l*) x 24 mm (*w*) x 0.13 mm (*t*)) were soaked in 10% Nitric Acid (w/w in DI water) overnight in order to increase the binding between the collagen gel and the glass substrate after collagen polymerization. The coverslips were then washed with fresh DI water and soaked in 10% APTES ((3-Aminopropyl)triethoxysilane) overnight. A final wash step and drying completed the coverslip surface functionalization. Next, the bottom layer of PDMS channels were treated with Pluoronic® F-127 to facilitate easy release of the collagen gel from the PDMS channel walls after gel polymerization was complete and the pressure was removed from the upper control chamber. This was accomplished by loosebonding the PDMS channel layer to a glass slide, filling the channels with 5% Pluronic® F-127 (w/w in DI water), and incubating at room temperature for 1 hour. DI water was then used to flush the channels before removing the PDMS layer from the glass and further rinsing the entire piece with DI water. These two surface modifications to the glass substrate and bottom PDMS channel layer aided the prevention of the polymerized collagen gel from shifting or breaking after releasing pressure from the control chamber.

The ligand trap was assembled (**Fig. 3.2(a)**) by using air plasma to irreversibly bond the glass substrate and PDMS layers together. Additionally, 10 mm x 10 mm Pyrex® cloning cylinders and 0.2" I.D. Tygon microbore tubing were attached to the device using liquid PDMS as a glue to serve as inlet/outlet reservoirs for the cell culture chambers and an injection port for the ligand trap chamber, respectively. After assembling the device, the semi-permeable gel/nanoparticle mixture was loaded into the central ligand trap channel. Several different recipes were used to make the gel/nanoparticle mixture, depending on the type of receptor protein used in the trap, the desired collagen concentration, and the desired particle concentration. For example, both biotin and protein A were available pre-conjugated to polystyrene nanoparticles (Spherotech, Lake Forest, IL); on the other hand, interleukin-6 receptor alpha (IL-6Rα) needed to be first adsorbed to the polystyrene particles. The following protocol was employed to produce 500 μL of ~0.4 μm polystyrene particles (0.25% w/v) adsorbed to mouse IL-6Rα proteins:

1. Add 225 μL of phosphate buffer (0.1 M, pH 7.4), 25 μL PBS, 25 μg of mouse IL-6Rα recombinant protein, and 25 μL of 5% w/v 0.4 μm polystyrene particles to a centrifuge tube.
2. Vortex and incubate the mixture for one hour at room temperature.
3. Centrifuge at 3000x g for 15 minutes.
4. Remove the supernatant and add 500 μL of PBS to the tube.

5. Vortex well and centrifuge again at 3000x g for 15 minutes.
6. Remove the supernatant and add 500 μL of PBS and mix well to obtain the final solution.

Note that this procedure was modified as necessary to change the final particle concentration or total volume produced.

The next step was to mix the collagen gel/nanoparticle mixture. The following protocol was used to produce a mixture with a ~1.5 mg/mL collagen concentration:

1. Add 10 μL of PBS and 0.381 μL of NaOH (1.0 N) to a centrifuge tube.
2. Add 73 μL of the protein coated nanoparticle solution to the centrifuge tube and vortex well.
3. Add 16.6 μL of high concentration collagen I (~9 mg/mL) to the centrifuge tube and vortex well.
4. Keep the mixture refrigerated or on ice until use. All steps should be carried out using centrifuge tubes, pipette tips, and solutions that are chilled (2-8°C).

For this step, the same protocol was employed whether pre-conjugated or manually adsorbed protein receptor nanoparticles were used. After making the collagen/nanoparticle mixture, it could be loaded into the device. First, the upper pressure control chamber was hydraulically pressurized; this deformed the roofs of the connecting microgrooves to the glass coverslip, separating the central ligand trap channel from the outer cell culture chambers. A syringe was then used to inject ~50 μL of collagen/nanoparticle mixture into the inlet tubing of the ligand trap channel. The outlet tubing was closed using small acetal ratchet tubing clamps, followed by clamping of the inlet tubing. The device was then placed in a 37-40°C humidified incubator for 30 minutes. After removal from the incubator, the device was allowed to cool to room temperature for 15 minutes. The pressure was then released from the upper pressure control chamber, fluidically reconnecting the cell culture chambers with the central ligand trap channel. These steps are summarized in **Fig. 3.2(b)**. Inspection of the gel barrier for defects completed the fabrication of the ligand trap microfluidic platform.

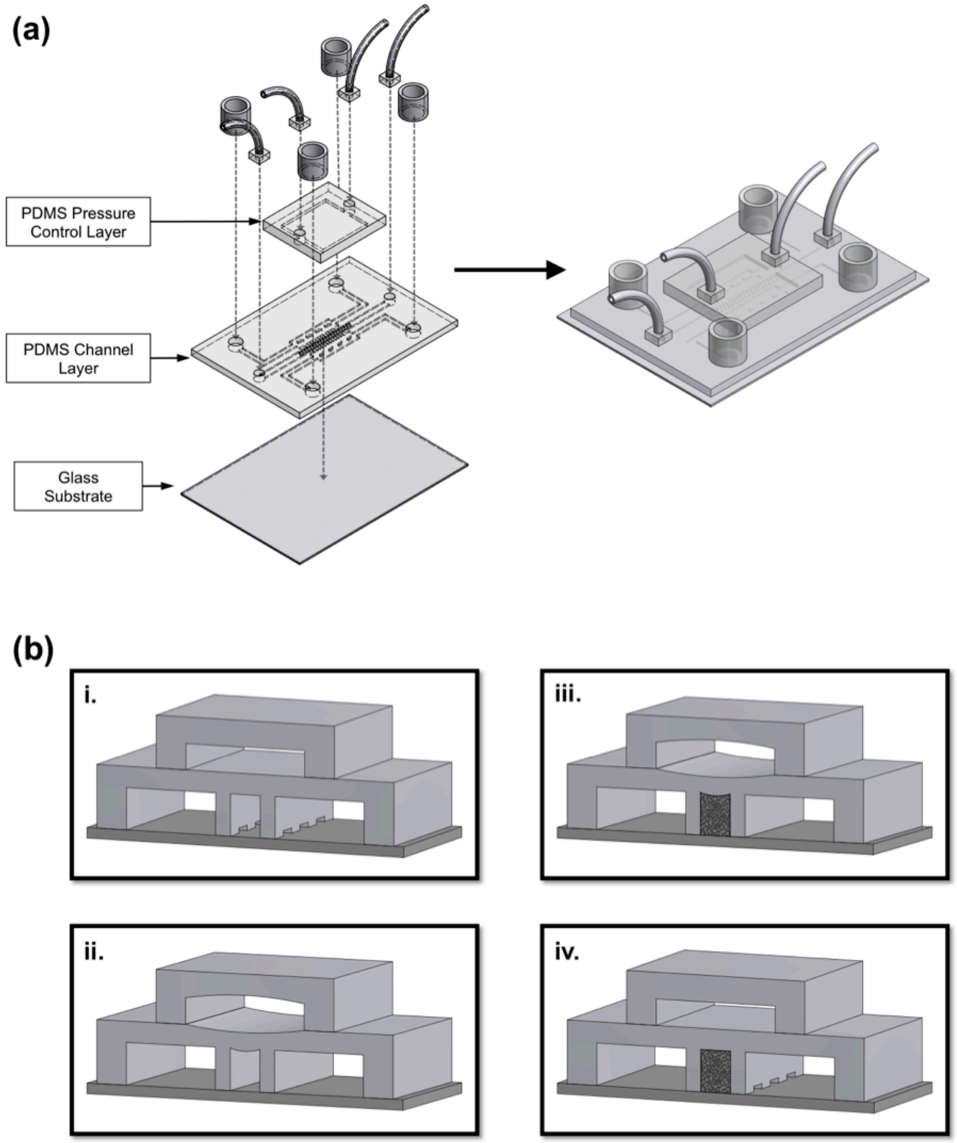

Figure 3.2: Fabrication of the microfluidic ligand trap device. **(a)** The glass substrate, PDMS channel layer, PDMS pressure control layer, and PDMS tubing supporters were bonded together using air plasma treatment. The inlet/outlet reservoirs and tubing were attached using liquid PDMS glue. **(b)** The collagen gel/nanoparticle mixture was loaded into the central ligand trap channel by (i-ii) pressurizing the control chamber, (iii) loading the mixture, allowing polymerization to occur, and (iv) releasing the pressure in the control chamber.

3.3 Demonstration Using Fluorescently Tagged Proteins

3.3.1 Avidin-Biotin

In order to test the effectiveness of the ligand trap, a model ligand/receptor pair was chosen: avidin (ligand) and biotin (receptor). Avidin and biotin have a dissociation constant (k_d) on the order of 10^{-15} M, one of the strongest non-covalent interactions between any ligand/receptor pair (Livnah, Bayer, Wilchek, & Sussman, 1993). Thus, this complex was ideal for the initial demonstration of the ligand trap device. Biotin-coated nanoparticles (~0.8 μm) at a concentration of 5% w/v were embedded in the collagen gel trap. Avidin molecules fluorescently tagged with Alexa Fluor® 488 were loaded into one of the culture chambers (source side). Additionally, Alexa Fluor® 647 tagged ovalbumin, another readily available protein that does not bind with biotin, was added alongside the avidin into the source side culture chamber (**Fig. 3.3(a)**). Fluorescence microscopy images were taken at different time points using separate filters to track the migration of both avidin and ovalbumin as it diffused into the barrier region. A summary of the resulting images is presented in **Fig. 3.3(b)**. From these results, two key differences in the migration of avidin and ovalbumin are readily apparent. First, the biotin conjugated nanoparticles appear to be effective in restricting avidin from diffusing through the barrier and into the opposite cell culture chamber (drain side). Significant fluorescence from ovalbumin is observed in the drain side chamber after 10 minutes, while almost no fluorescence from the avidin is visible. Second, the fluorescence intensity in the barrier region is much higher than in the culture chamber when viewed through the avidin Alexa® 488 filter. On the other hand, the fluorescence intensity in the barrier region is virtually identical to the culture chamber for the ovalbumin Alexa® 647 filter. This indicates that avidin molecules are aggregating at the biotin receptor sites in the barrier region, causing an increase in intensity, while little to no ovalbumin is undergoing unwanted non-specific binding in the trap channel.

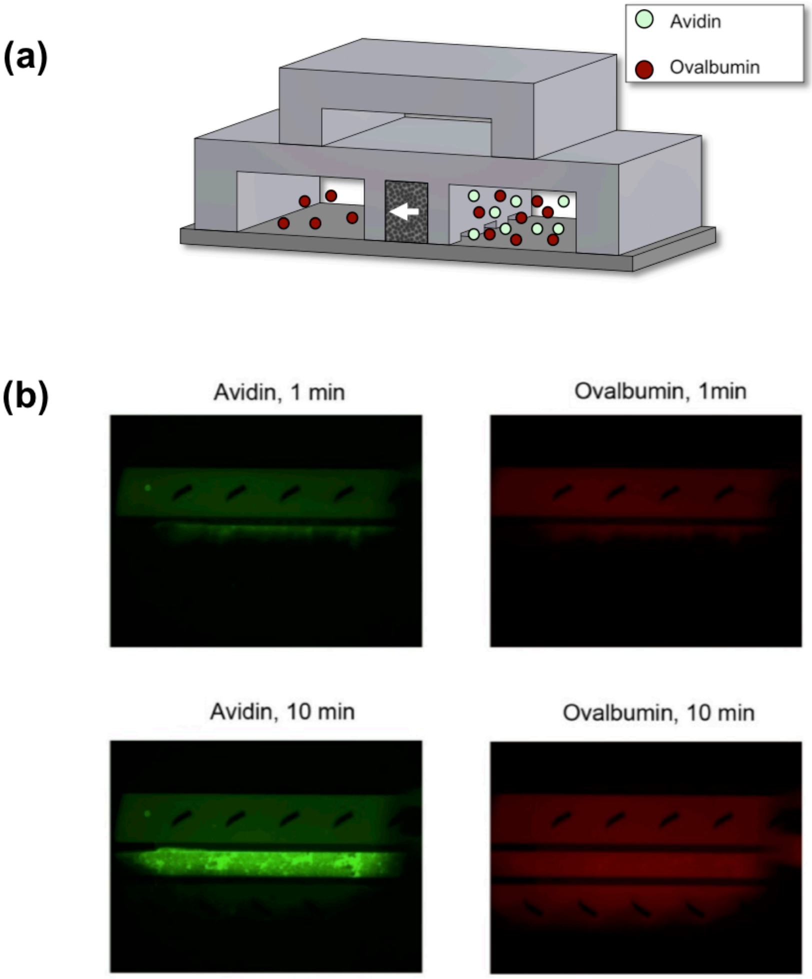

Figure 3.3: Initial demonstration of the ligand trap design using fluorescence microscopy. **(a)** Experimental setup in which fluorescently tagged avidin and ovalbumin were added to one of the cell culture chambers. Biotin-coated nanoparticles embedded in the semi-permeable gel barrier trapped the avidin in the central region while allowing ovalbumin to pass through. **(b)** Fluorescence images showcasing the migration of avidin and ovalbumin both 1 and 10 minutes after loading the proteins. Panel **(b)** is reprinted from (Gao et al., 2012).

Although the initial ligand trap experiment using avidin and biotin effectively demonstrated the validity of the device design, the time scale in which the device operated is not useful for typical cell culture studies. The barrier region appears to be nearly saturated with avidin molecules after only 10 minutes. A saturated ligand trap means that all of the biotin receptor sites in the barrier are occupied. When this occurs, any additional avidin that enters the barrier region will be able to move through the barrier without being blocked. Typical cell culture experiments may require the trap to work for time periods up to two weeks (Tourovskaia, Figueroa-Masot, & Folch, 2005). Thus, for the ligand trap platform to be practically useful, it needs to work for longer periods of time.

A relatively high concentration of avidin (32 μg/mL) was required in the initial experiment described above in order to actually visualize the avidin using the fluorescence microscope. Both intuition and theoretical analysis suggest that for lower ligand concentrations, the trap should retain its ability to block the targeted ligand for longer time periods. In reality, the concentration of soluble molecules produced by cells in culture is orders of magnitude lower than the concentration used in our first experiment. Thus, we improved the fluorescence microscopy setup to make it more sensitive to lower concentrations of the Alexa Fluor® 488 fluorophore, allowing us to monitor the trap performance with avidin concentrations closer to physiological relevance.

A second experiment was performed in which the concentration of Alexa Fluor® 488 tagged avidin was 1 μg/mL, significantly lower than the concentration used in our initial demonstration (note that this concentration is still a few orders of magnitude higher than would typically be found in cell culture). Additionally, the trap design was slightly modified by increasing its width from 200 μm to 700 μm and by adding pillars in the trap region to help prevent the roof of the barrier region from collapsing during gel loading. No ovalbumin was used in this experiment. Initially, 300 μL of DI water was added to the inlet reservoir of one culture chamber, followed by the addition of 300 μL of avidin solution to the other culture chamber. Additionally, 100 μL of each solution was added to the appropriate outlet reservoirs of each chamber. Periodically, 200 μL of each solution was added to the inlet reservoirs to compensate for evaporation. Fluorescence images were acquired at different time points for two days. The results obtained are summarized in **Fig. 3.4**. Note that the increase in intensity observed in the source side culture chamber is likely due to evaporation over time increasing the concentration of avidin in the chamber. From these images, it appears that the biotin-trap barrier does not approach saturation until after 48 hours. This suggests that the ligand trap platform can be potentially used for the longer time periods required by typical cell culture experiments.

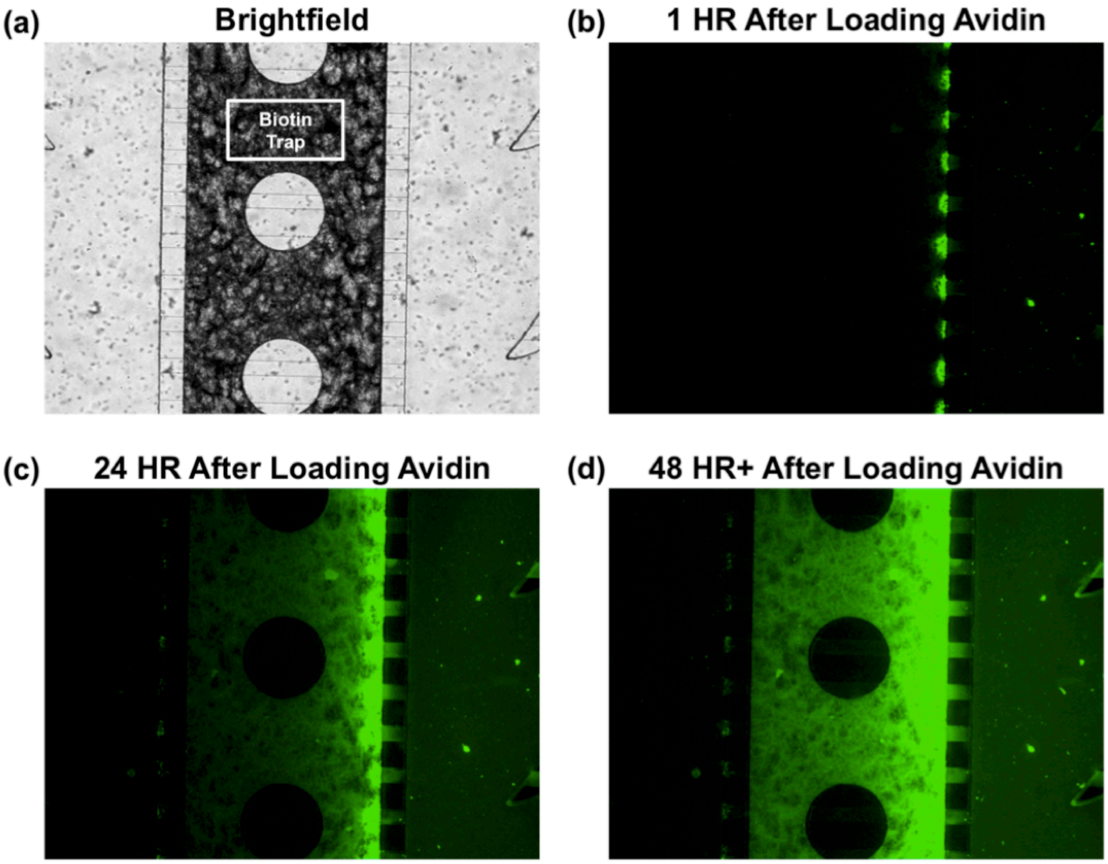

Figure 3.4: Demonstration of the long-term effectiveness of a ligand trap using avidin in a biotinylated trap. The circular PDMS pillars were needed for support in the 700 μm wide middle channel shown here. **(a)** Brightfield image showing the location of the nanoparticle gel, and fluorescence images demonstrating avidin penetration into the biotin trap after **(b)** 1 hour, **(c)** 24 hours, and **(d)** 48 hours.

3.3.2 Lower Binding Affinity Investigation with IgG-Protein A

Although lower concentrations of avidin allowed the ligand trap to remain effective for longer periods of time, other performance criteria must be achieved before using the platform in real cell culture assays. As mentioned above, the binding affinity of avidin and biotin is exceptionally strong. In fact, the avidin/biotin k_d value of ~10^{-15} M is several orders of magnitude lower than many ligand/receptor pairs typically found in cell culture (Nahshol et al., 2008). Thus, practical applications of the device would require the trap to work for ligand/receptor pairs that do not bind as strongly as the demonstrated avidin/biotin complex. To address this issue, a different ligand/receptor pair was chosen as a test model: goat immunoglobulin G (IgG) and protein A. The dissociation constant for goat IgG and protein A is ~10^{-10} M, which is similar to many other physiologically relevant ligand/receptor pairs of interest. Using the same setup that was employed in the long-term avidin/biotin experiment, the ligand trap device was tested using 4 μg/mL Alexa Fluor® 488 goat IgG and 0.8 μm protein A-coated nanoparticles. Note that the width of the barrier region in this device was 400 μm, and no support pillars were used. As seen in **Fig. 3.5**, the protein A trap was able to effectively block the transport of goat IgG between the culture chambers for at least 12 hours. Thus, these results suggest that the ligand trap platform can be effective even for ligand/receptor pairs with binding affinities representative of those found in many physiologically relevant ligand/receptor complexes.

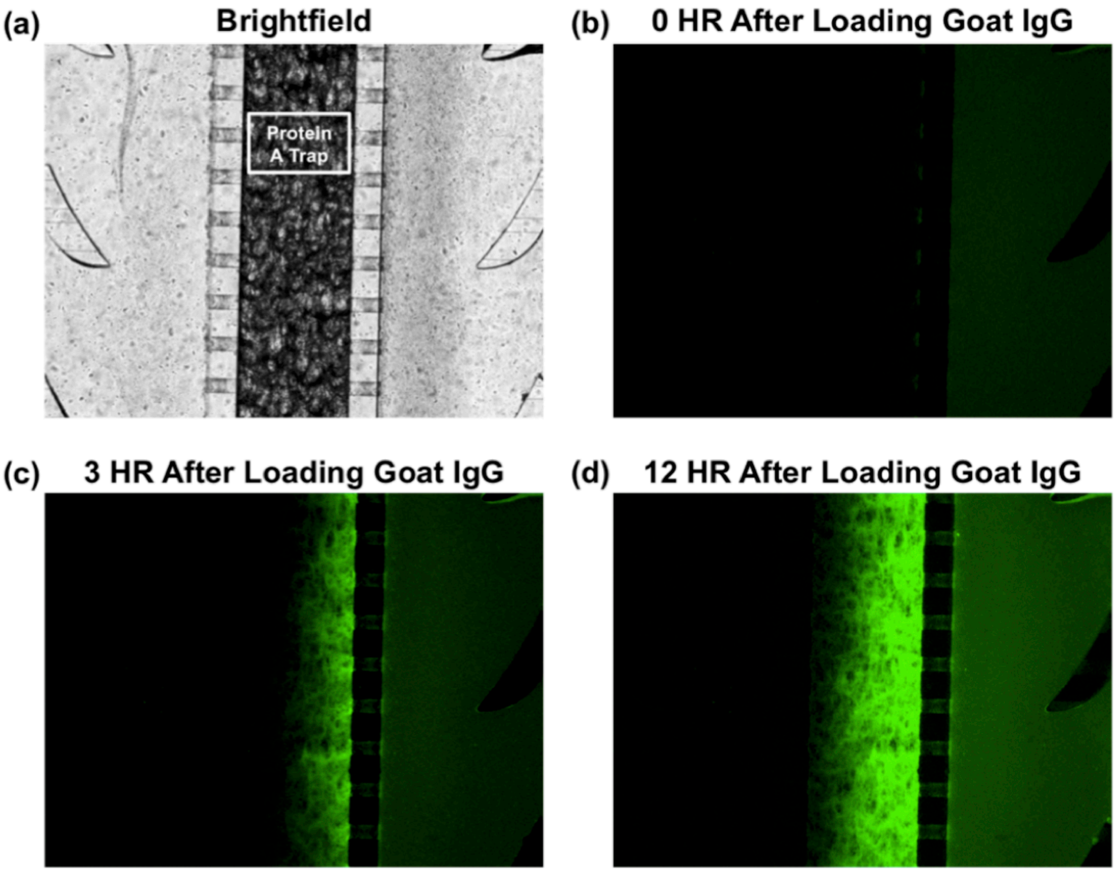

Figure 3.5: Demonstration of the viability of the ligand trap platform using the lower binding affinity goat IgG/protein A pair. No support pillars were used in this iteration of the device. **(a)** Brightfield image showing the location of the nanoparticle gel, and fluorescence images demonstrating goat IgG penetration into the protein A trap after **(b)** 0 HR, **(c)** 3 HR, and **(d)** 12 HR.

3.4 Investigation of Retinal Interleukin 6 Signaling

3.4.1 Motivation

The true value of the ligand trap platform in cell biology research will be governed by its effectiveness and usability with a multitude of relevant ligand/receptor pairs, not just model demonstration proteins. As such, we have chosen to employ our ligand trap design in the investigation of the protein interleukin 6 (IL-6). IL-6 is an important molecule in the human body, serving as both a pro-inflammatory cytokine and anti-inflammatory myokine (Ferguson-Smith et al., 1988). For example, IL-6 plays important roles in the immune response, particularly in cases of infection and inflammation due to tissue trauma (van der Poll et al., 1997). Additionally, IL-6 is an integral component of bone metabolism through its stimulation of osteoclast formation (Jilka et al., 1992) and is a molecule capable of crossing the blood-brain barrier (Banks, Kastin, & Gutierrez, 1994). We are specifically interested in IL-6 because of its role in the formation of neuroinflammatory microenvironments in the retina, which is an important component of the eye disease glaucoma. Previous studies have indicated that IL-6 related signaling events between astrocytes, microglia, and retinal ganglion cells in the retina may be important in the neuroinflammatory response (Mendonça Torres & de Araujo, 2001; Sappington, Chan, & Calkins, 2006; Sims, Holmgren, Cathcart, & Sappington, 2012). Intercellular signaling could occur via a variety of mechanisms, including direct cell-cell contact, classical signaling involving the binding of IL-6 with its receptor IL-6Rα, and trans-signaling that requires IL-6 to bind with soluble IL-6Rα, forming a complex that interacts with surface-bound sites expressing the signal transducer gp130 (Murakami et al., 1993). The ligand trap platform is well-suited for probing the contributions of each of these signaling processes to the overall formation of the retinal neuroinflammatory microenvironment since the device is capable of isolating each specific signaling pathway without disrupting the others. Therefore, we have pursued making the proper modifications to the ligand trap design to examine these signaling pathways

Before the actual investigation of the classical signaling pathway mentioned above that involves the binding of IL-6 with IL-6Rα could be conducted, the ligand trap design needed to be modified and its effectiveness with the new ligand/receptor pair evaluated. Instead of using the fluorescence microscopy imaging described above, an enzyme linked immunosorbent assay (ELISA) was chosen to assess device performance. An ELISA uses a series of antibodies and enzymes to trap a targeted ligand in a standard plate well, producing a visible signal. Spectrophotometric analysis can then be conducted to quantitatively determine the concentrations of the ligand present in each plate well. This method offers excellent detection (down to ~1 pg/mL) and often comes in ready-to-use kits that are relatively inexpensive, enabling multiple trials to be conducted. Therefore, this technique was an ideal means of evaluating the modified IL-6 ligand trap devices.

3.4.2 ELISA Sample Preparation and Protocol

Testing the effectiveness of the ligand trap using the mouse IL-6/IL-6Rα pair was achieved by first conjugating IL-6Rα proteins to ~0.4 μm polystyrene nanoparticles as described above. Then, using a recipe similar to the one previously described, a 3 mg/mL concentration collagen gel was prepared and loaded into a ligand trap device. Additionally, a control ligand trap device was also fabricated using nearly the same protocol, with the exception being that no IL-6Rα proteins were conjugated to the polystyrene nanoparticles. A 1 μg/mL solution of recombinant IL-6 was prepared by diluting 20 μL of a stock 100 μg/mL IL-6 solution in 1980 μL of PBS.

A schematic demonstrating the experimental design is shown in **Fig. 3.6**. By loading IL-6 solution into the source inlet of the control and test devices and periodically removing effluent from the drain outlet for analysis by ELISA, the effectiveness of the

IL-6Rα ligand trap at different time points could be determined. The following steps were performed to conduct this experiment:

1. Load 400 μL of PBS in the drain inlets of both devices, followed by 400 μL of 1 μg/mL IL-6 solution in each source inlet.
2. Load 100 μL of PBS in each drain outlet and 100 μL of IL-6 solution in each source outlet.
3. After 2 hours, remove 115 μL of effluent from the drain outlet of each device, followed by 115 μL of effluent from each source outlet. Each effluent sample is stored in a separate tube, and separate pipette tips should be used for each sample to avoid cross-contamination.
4. Reload 115 μL of IL-6 solution and PBS into the source and drain inlets of each device, respectively.
5. Repeat Steps 3 and 4 for each additional desired time-point.

Note that the devices were placed in Petri dishes sealed with Parafilm between sample loading/retrieval to prevent solvent evaporation.

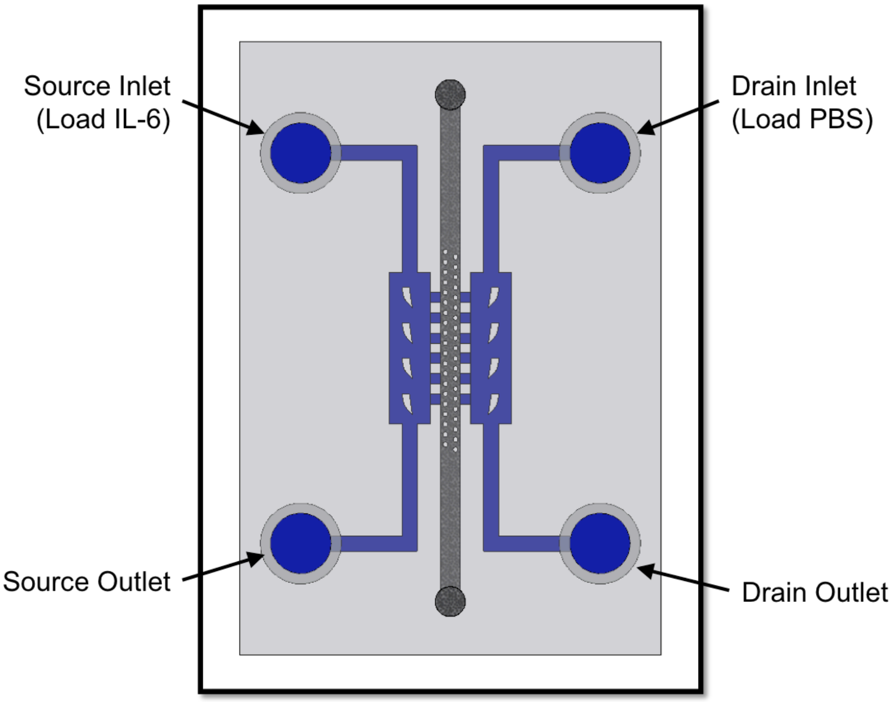

Figure 3.6: Experimental design used for ELISA testing of the IL-6/IL-6Rα ligand trap. Effluent retrieved from the drain outlet of the control and test devices was analyzed to determine the concentration of IL-6 that had migrated from the source side.

The samples were analyzed using a Mouse IL-6 Quantikine ELISA kit (R&D Systems, Minneapolis, MN). The plate wells containing each sample were prepared and treated according to the manufacturer's instructions. The concentration of IL-6 present in each sample was determined using a Spectramax Plus384 Absorbance Microplate Reader (Molecular Devices, Sunnyvale, CA).

3.4.3 ELISA Results

The relative concentrations of IL-6 in the drain outlets of the control and IL-6 trap devices after 2 hours are shown in **Fig. 3.7**. The concentration of IL-6 determined by ELISA in the control drain after 2 hours is ~164 times higher than the concentration observed in the device with IL-6Rα conjugated nanoparticles. These results indicate effective blockage of IL-6 in the actual ligand trap device when compared to the control device. However, the absolute concentration measured in the control device after 2 hours was in the 1-2 pg/mL range, a concentration near the lower limit of detectability for the ELISA test kit. Noting the 1 μg/mL concentration of IL-6 in the source side, it appears that little IL-6 is making it to the drain outlet, even in the control device in which no receptor proteins are present. This low observed concentration in the effluent is most likely the result of dilution from the extra PBS solution in the drain channel; nonetheless, the validity of ELISA data obtained at the extreme limits of the kit's detection capability must be questioned. Unfortunately, the results observed in this initial demonstration were difficult to consistently reproduce. As the aforementioned dilution issue continued to be a problem, several modifications to the experimental design were attempted to obtain usable effluent samples. The first, most obvious approach was to simply reduce the volume of buffer in the drain side channel to decrease the dilution effect. This was achieved by both reducing the volume of PBS added to the drain side and decreasing the actual size of the drain side channel dimensions. Using these techniques, a more concentrated effluent sample was collected from the drain side waste reservoir. However, the volume of effluent collected was reduced to ~2-5 μL, significantly less than the 50 μL of sample required for each ELISA test well. As a result, the collected samples had to be re-diluted before testing, reducing the actual measureable protein concentration back to a level near the lowest detectable value. This process also introduces some degree of uncertainty when comparing samples due to pipetting variations inherent in dealing with such minute volumes. Furthermore, the reduction of buffer volume in the drain side channel produces a significant cross-flow from the source to drain side. The transport of ligands into the gel region due to convection results in the receptor sites on the nanoparticles becoming saturated more quickly, reducing the length of time in which the ligand trap remains effective. Thus, applying the unrealistic operating conditions described here diminishes the effectiveness of the ligand trap while still failing to generate samples that can be quantitatively analyzed. Therefore, an alternative approach needed to be developed to continue characterization of the IL-6 ligand trap device.

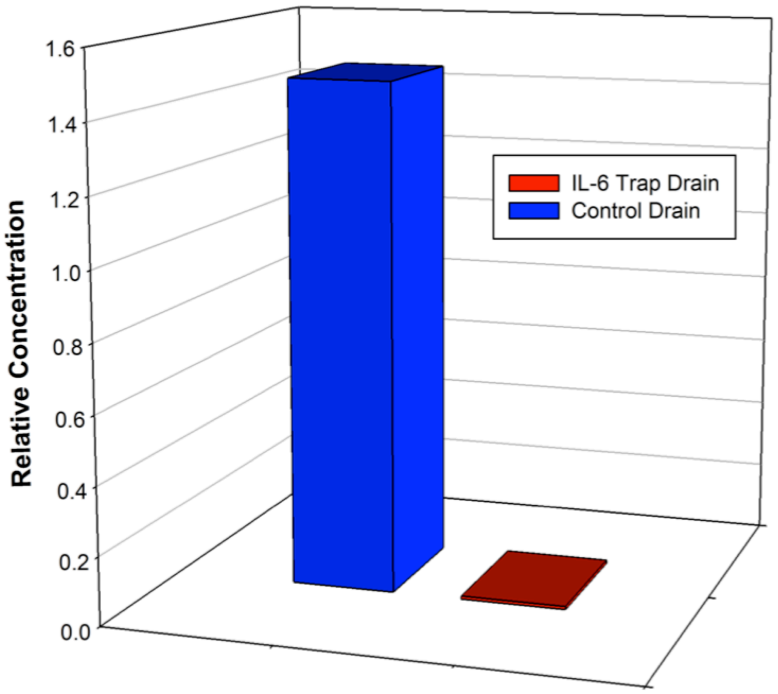

Figure 3.7: ELISA results comparing the concentration of IL-6 measured in the drains of the control and IL-6 trap devices after 2 hours.

3.4.4 Alternative Photopolymerizable Ligand Trap Approach

In order to achieve the desired quantitative evaluation of the ligand trap, an alternative approach was developed that replaced the high concentration collagen gel with a photopolymerizable poly(ethylene glycol) diacrylate (PEGDA) hydrogel. The fabrication of the PEGDA device is significantly simpler than the collagen gel approach and is summarized in **Fig. 3.8**. Briefly, the PEGDA solution is formulated based upon a previous protocol (Cuchiara et al., 2010) and contains 20% (w/v) PEGDA in PBS, the photoinitiator Irgacure 2959 (100 mg/mL in ethanol), and polystyrene nanoparticles. The device itself consists of a single layer of PDMS containing a large chamber with multiple inlet/outlet channels and an array of square PDMS pillars in the center of the chamber that provide structural support for the PEGDA gel barrier. After plasma bonding the

PDMS to a glass coverslip, the PEGDA gel mixture is loaded into the entire chamber and the inlets/outlets are covered with tape. A photomask of a single channel is then taped to the bottom of the coverslip, overlaying the center of the chamber where the array of square pillars is located. The device is then exposed to a 365 nm UV source at ~15 mW/cm^2 with the mask side up for 10 minutes. Finally, the unpolymerized PEGDA gel solution is flushed out of the chamber using DI water. An optical microscope image of the resulting PEGDA gel barrier is shown in **Fig. 3.9**.

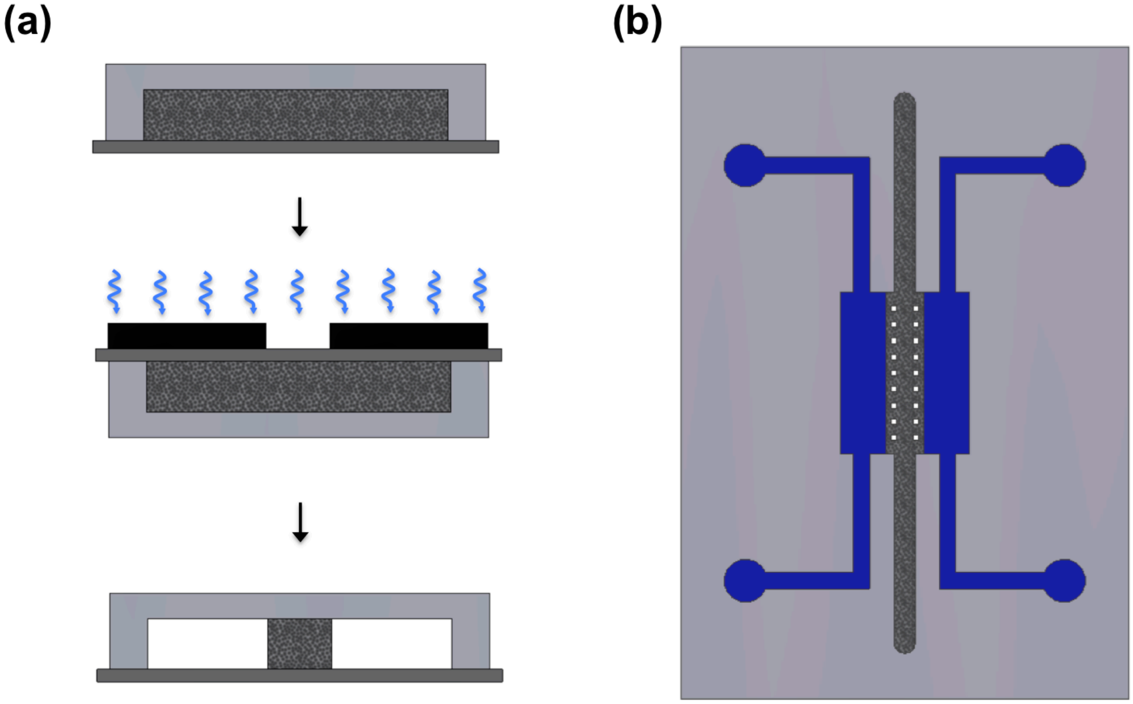

Figure 3.8: Fabrication of the photopolymerizable PEGDA ligand trap device. **(a)** A series of cross-sectional schematics demonstrates the photocuring process. The entire device is filled with the PEGDA/particle gel mixture (top panel), then exposed through a photomask (middle panel). Finally, the excess solution is washed out, leaving the PEGDA/particle gel barrier in the center (bottom panel). **(b)** Top-view schematic of the fabricated device.

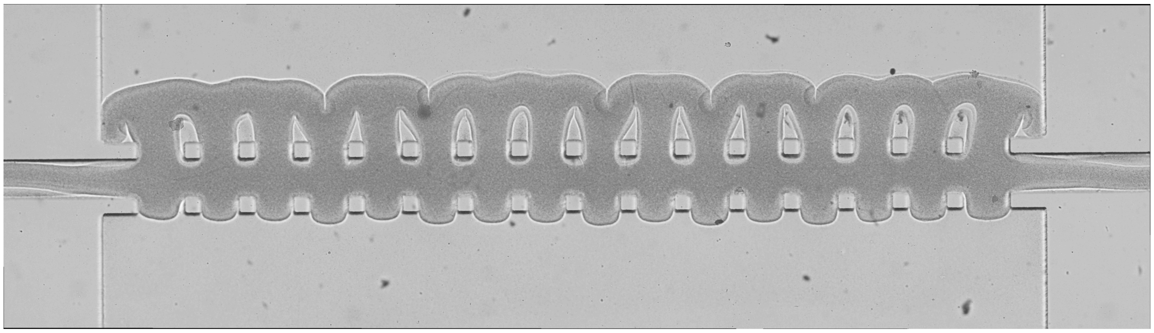

Figure 3.9: Optical microscope image of a photopolymerized PEGDA/nanoparticle gel barrier.

The photopolymerized PEGDA gel platform provides a couple of key advantages over the pressure valve collagen gel device. First, the device fabrication and operation is simpler. The pressure valve device requires an effective seal when loading the collagen gel, and the release of pressure after polymerization in the incubator can sometimes cause the newly formed collagen gel to shift around within the central channel or even separate. Furthermore, special coatings must be applied to the PDMS and glass substrate to ensure the gel does not peel off of the glass upon pressure release. On the other hand, PEGDA gel device does not require the use of a pressure control chamber or any special coatings; this results in a more straightforward device fabrication with a higher reproducibility. Second, the PEGDA gel system provides a functional advantage in that a larger cross-sectional area of the gel is exposed to the side cell culture chambers. This larger area means the entire volume of the gel barrier can uniformly work to trap ligands as they pass through to the other culture chamber. For the collagen gel device, all media must flow through the 5 μm tall microgrooves on the glass substrate, resulting in a gel barrier that becomes saturated more quickly at the bottom (near the substrate) with few ligand molecules reaching the top of the gel. Thus, for the same volume of the gel, the photopolymerizable PEGDA gel device should be able to trap more molecules, enabling the collection of larger sample volumes from the drain side channel. As mentioned earlier, a larger sample volume will increase the likelihood of obtaining reliable, quantitative ELISA data about device performance, validating this alternative approach to the ligand trap idea.

3.5 Summary

We have developed a microfluidic ligand trap platform that uses receptor-coated nanoparticles embedded in a semi-permeable barrier to selectively remove targeted signaling molecules from the microenvironment of a cell population. The device was tested and demonstrated using several proteins and methods. Fluorescence microscopy was used to show the potential of the device for use in long-term cell culture experiments with the high binding affinity ligand/receptor protein pair of avidin and biotin. Protein A and Goat IgG were also used to demonstrate the efficacy of the ligand trap with ligand/receptor pairs having binding affinities similar to those typically encountered in cell culture. Finally, the ligand trap design was modified for investigation of the important role that IL-6 signaling plays in the neuroinflammatory response in the retina. Although initial results obtained using ELISA were inconsistent, modifications to the fabrication approach were proposed that employ the photopolymerizable hydrogel PEGDA. The potential improvements indicated by early testing of this system suggests that with further optimization, the device will be well-suited for the investigation of IL-6 signaling pathways and adaptable for signaling studies with other cell types.

CHAPTER 4

MICROFLUIDIC STRETCHER PLATFORM FOR INVESTIGATING THE ROLE OF MECHANOTRANSDUCTION IN NAF/CAF TRANSFORMATION

4.1 Motivation

Although most cancers, and by definition all carcinomas, are derived from epithelia, interactions with other cell types in the surrounding host microenvironment (stroma) are crucial for tumor cell growth, survival, and metastatic spread (Bhowmick & Moses, 2005; Cirri & Chiarugi, 2012). For example, cancer-associated fibroblasts (CAFs) have been shown to induce and promote the invasion of initiated but non-malignant epithelium (Olumi et al., 1999), as well as cancer cells raised from the human colon (De Wever et al., 2004), breast (Orimo et al., 2005), prostate (Giannoni et al., 2010), and other organs. To date, most of these studies have focused on cancer-stroma interactions via paracrine biochemical mediation. In contrast, the role of mechanical stress in cancer cell invasion has not attracted much attention, even though mechanotransduction has been shown to be important in fibroblast functions such as the production and remodeling of extracellular matrix (ECM) components (Chiquet, Gelman, Lutz, & Maier, 2009; Z.-D. Shi & Tarbell, 2011).

The study of mechanical stress-induced fibroblastic responses can be traced back more than three decades. The pioneering work was conducted both *in vitro* and *in vivo* to examine periodontal ligament alteration upon exposure to mechanical forces (Carano, 1990; Lekic & Mcculloch, 1996). As the dominant cell type in the periodontal ligament, fibroblasts sense and react to altered mechanical environments by modulating the synthesis and fibrillar assembly of ECM components, including collagen and fibronectin (Chiquet, Koch, Matthisson, Tannheimer, & Chiquet-Ehrismann, 1996; Halliday & Tomasek, 1995). These observations in dentistry soon drew attention from the cardiovascular field in which mechanical stress is associated with cardiac dysfunction in hypertensive heart diseases. Increased mechanical stress was shown to cause myocardial hypertrophy, vessel wall thickening, and fibrosis (Bishop, 1998). An additional study showed that a 10% uniaxial stretch of cardiac fibroblasts resulted in an increased expression of fibronectin and collagen type III mRNA. Interestingly, when a 20% stretch was applied, mean levels of fibronectin and collagen III mRNA were lower than the unstretched control (A. A. Lee, Delhaas, McCulloch, & Villarreal, 1999). Similar force magnitude dependence was also found in trials of equibiaxial stretching (Steward, Cheng, Ye, Bellin, & LeDuc, 2011).

The reorientation of fibroblasts under uniaxial cyclic stretch has also been a subject of research. Stretched fibroblasts were reported to migrate faster and farther than their unstretched counterparts while also aligning themselves perpendicular to the direction of stretching (C. Huang et al., 2013). Fibroblast morphology is also affected by the application of mechanical stress. For example, a study that examined the stretching of whole tissues both *in vivo* and *ex vivo* found that fibroblasts in the stretched tissues exhibited larger, “sheetlike” cell bodies with shorter processes, while fibroblasts in unstretched tissues demonstrated a more dendritic morphology with smaller, more globular cell bodies and longer processes (Langevin, Bouffard, Badger, Iatridis, & Howe, 2005).

Mechanical force is also considered to be an important factor in the formation of activated fibroblasts called myofibroblasts (MFs) (Daskalopoulos, Janssen, & Blankesteijn, 2012). Characterized by their contractile activity, MFs are commonly found at injury sites, where their primary function is to close the wound (Gabbiani, 2003; Sarrazy, Billet, Micallef, Coulomb, & Desmoulière, 2011). These cells are also an important component of the reactive stroma found at sites of chronic inflammation, fibrosis, and surrounding a variety of malignancies (Gonda, Tu, & Wang, 2009; Phan, 2010; De Wever & Mareel, 2003). In fact, many myofibroblast characteristics, such as smooth muscle actin (SMA) expression, the acquisition of contractile stress fibers, *de novo* expression of the extra domain-A (ED-A) alternative splice variant of fibronectin, the formation of cell-cell contacts through gap junctions (Tomasek, Gabbiani, Hinz, Chaponnier, & Brown, 2002), and the secretion of higher levels of cytokines and chemokines are also observed in another population of activated fibroblasts referred to as CAFs (Ao et al., 2007). Heterogeneous populations of CAFs are found in abundance in the stroma of numerous tumors, including breast, prostate, and pancreatic carcinomas (Cirri & Chiarugi, 2012). It is also worth noting that although CAFs were once thought of as a discrete population, it is now becoming clear that the CAF phenotype in the tumor microenvironment represents a downstream consequence of the interactions among multiple fibroblastic populations (Franco, Shaw, Strand, & Hayward, 2010; Kiskowski et al., 2011). Nonetheless, both MFs and CAFs alter the production, digestion, and organization of the ECM (Allen & Jones, 2011), and these properties have been shown to contribute to CAFs' role in the promotion of cancer invasion and metastasis (Cirri & Chiarugi, 2012; Franco & Hayward, 2012; Hu et al., 2013). The phenotypic similarities between these two cell types suggests that, just as it is for MFs, mechanical force may also be an important factor in the formation of CAFs.

Although a multitude of studies have attempted to characterize CAF gene expression, signaling pathways, and tumor promoting functions, the mechanisms by which CAFs are actually generated in tumors are still not well understood; however, normal tissue-associated fibroblasts (NAFs) are thought to be one of the major sources for CAFs (Kalluri & Zeisberg, 2006; Polanska & Orimo, 2013; Xing et al., 2010). Surprisingly, no work has yet demonstrated the direct influence of mechanical stress on CAF genesis, although a growing body of evidence suggests that mechanical changes in the tumor microenvironment are induced by the expansion of tumor cells (Shieh, 2011). As a tumor grows, it exerts forces on the surrounding tissue, inducing local compressive stresses (in the direction of tumor growth) and circumferential tensile stresses (Shieh, 2011). These forces could have important effects on the non-tumor cells in the microenvironment.

Considering the fact that mechanical stress exists in the tumor microenvironment and is an important factor in many fibroblast activities, it is possible that mechanical stress plays a role in the activation of fibroblasts, resulting in the formation of CAFs and leading to ECM remodeling of the tumor microenvironment and the promotion of cancer cell migration. To test this hypothesis, we used a microfluidic platform to stretch NAFs and observed their responses to the external mechanical stimulus (Ao et al., 2015). We show here that mechanical stretching can modify NAF-produced fibronectin alignment and stimulate the fibroblasts' ability to direct cancer cell migration in a persistent way.

These data suggest that mechanical stress plays a significant role in the genesis of CAF phenotypes and thus may contribute to the subsequent promotion of cancer progression.

4.2 Stretcher Device Operation and Fabrication

The microfluidic stretcher platform used in these studies is based on the work by Huh et al., which developed a microdevice capable of reconstituting the alveolar-capillary interface of the human lung (Huh et al., 2010)**.** A three-dimensional schematic of the device is shown in **Fig. 4.1(a)**. Applying a negative pressure to the two vacuum channels on each side of a middle chamber with a suspended PDMS membrane causes the side walls of the middle chamber to deflect outward, imparting a mechanical stretch on cells attached to the suspended PDMS membrane (**Fig. 4.1(b)**). Both the top and bottom layers of the central cell culture chamber are 5 mm in length (*l*), 1 mm wide (*w*), and 100 μm in height (*h*). On the other hand, the inlet/outlet channels for the central chamber are only 400 μm wide. The wider cell culture chamber serves to reduce the flow velocity in that region, which helps to slow down cells that have been loaded through the inlet reservoir and facilitate attachment of the cells to the suspended PDMS membrane (10 μm thick). Each layer of the vacuum channel region is 550 μm (*w*) x 100 μm (*h*) and spans the length of the cell culture chamber region. Finally, the thickness of the wall between the outer vacuum channels and the central cell culture chamber is 75 μm. It was determined through trial and error that this wall thickness allowed for easy manual alignment of the top and bottom layers during fabrication while still yielding desired membrane strains.

Several important modifications were made to the original microfluidic stretcher design outlined by Huh et al. to simplify fabrication, enhance functionality, and improve reproducibility. First, no etching of the PDMS membrane in the vacuum channels was performed. The etchant used to etch PDMS membranes, a mixture of tetrabutylammonium fluoride (TBAF) and N-methylpyrrolidinone (NMP), is highly flammable, can cause severe skin burns and eye irritation, and is carcinogenic (Sigma-Aldrich, 2013), which makes working with the chemical less than ideal. More importantly, it is difficult to control the final thickness of the channel walls from device to device, as the PDMS etching rate is relatively high (~5 μm/minute) and etchant loading and removal must occur through the inlet and outlet reservoirs. This becomes problematic when consistent strains need to be applied in multiple assays using different devices, as the deflection of the PDMS sidewalls is inversely proportional to the thickness cubed. Thus, small changes in channel wall thickness in the devices could result in significantly different membrane strains for a given applied vacuum pressure. For our devices, instead of etching the PDMS membrane, small holes were punched in the suspended membrane in each vacuum channel using a 30-gauge needle. This connects the top and bottom channels, which yields uniform vacuum pressure in the vacuum channel while improving the consistency among devices. This is because without the etching step that is difficult to precisely control, only the dimensions of the SU-8 mold govern the thickness of the channel sidewalls. Note that the punching is only performed in the vacuum channels on each side, and in the cell culture chamber, we have a solid PDMS membrane as opposed to the porous membrane employed by Huh et al. Unlike the "lung-on-a-chip" device, our microfluidic platform does not require any permeability between cells cultured on the top and bottom of the suspended membrane; thus, we chose to use a simple solid, stretchable PDMS membrane for the application of mechanical stress to fibroblasts cultured only on top of the membrane. For the second modification, an open channel thin PDMS film was used as the bottom layer of the device as opposed to a thick PDMS piece identical to that used for the top layer of the device (see **Fig. 4.1(c)**). Combined with a thin glass coverslip, the 100 μm thick bottom layer renders the device more compatible with advanced confocal microscopy and live-cell imaging. Additionally, this fabrication technique allows for the detachment of the top layer/thin membrane assembly after device use and subsequently enables imaging of fixed cells at even higher magnifications, which is extremely important for examination of fine structures such as the alignment of secreted fibronectin fibers.

The microfluidic stretcher platform consists of three primary components: a 2-3 mm thick polydimethylsiloxane (PDMS) (SYLGARD 184 Silicone Elastomer Kit, Dow Corning, Midland, MI) top layer, a ~10 μm thick spin-coated PDMS membrane, and a 100 μm thick thin-film PDMS bottom layer. Different protocols were used in the fabrication of each piece. For the thick PDMS top layer, traditional soft lithography methods were employed (McDonald & Whitesides, 2002; G M Whitesides et al., 2001). A 100 μm thick SU-8 (SU-8, Microchem Inc., Newton, MA) mold outlining the key channel features was fabricated on a silicon wafer using photolithography. PDMS mixed at a ratio of 10:1 (base polymer : curing agent) was poured on the SU-8 mold, degassed for ~1 hour, and cured in a 70°C oven for at least 2 hours. The ~10 μm thick PDMS membrane was prepared using a spin-coating process. A small amount of mixed, degassed PDMS was dropped on the treated side of a 3″ x 3″ plastic fluoropolymer coated polyester (PE) transfer sheet (Scotchpak™ 1002 Release Liner, 3M™, St. Paul, MN) that was taped to a Petri dish lid. Using a spin-coater, the PDMS was spun at 4000 RPM for ~1 minute, which was then cured for ~4 hours at 70°C. The 100 μm thick PDMS bottom layer was fabricated using the method described by Hsu et al (Hsu, Chen, & Folch, 2004). A small amount of PDMS was spread thinly over an SU-8 mold and covered with a 3″ x 3″ fluoropolymer coated PE sheet. The mold-PDMS-PE sheet stack was then degassed for ~1 hour. A small plastic squeegee was used to push out any remaining air bubbles, after which 1 mm thick glass slides were pressed on top of the PE sheet to ensure clean contact between the PE sheet and the top of the SU-8 mold features. Five pounds of weights were added on top of the glass slides, and the whole package was placed in a 70°C oven for at least 4 hours to cure.

After completing the fabrication of each individual device layer, the three components were assembled into the final microfluidic stretcher platform. First, the thick PDMS top layer was attached to the spin-coated PDMS membrane using plasma bonding. After bonding, the PE transfer sheet was removed from the backside of the thin PDMS membrane layer, and holes were punched in the inlet/outlet of the central cell chamber channel and in the inlets of the two outer vacuum chamber channels. A 30-gauge needle was then used to make small tears in the PDMS membrane above the vacuum chamber regions. Next, the 100 μm thick PDMS bottom layer was plasma bonded to a 24 mm x 60 mm x 0.13 mm glass coverslip, after which the PE transfer sheet was removed. Finally, the two newly formed components were bonded together, with care taken to align the upper and lower channels. Inlet/outlet reservoirs and tubing were then attached to the device using liquid PDMS as glue.

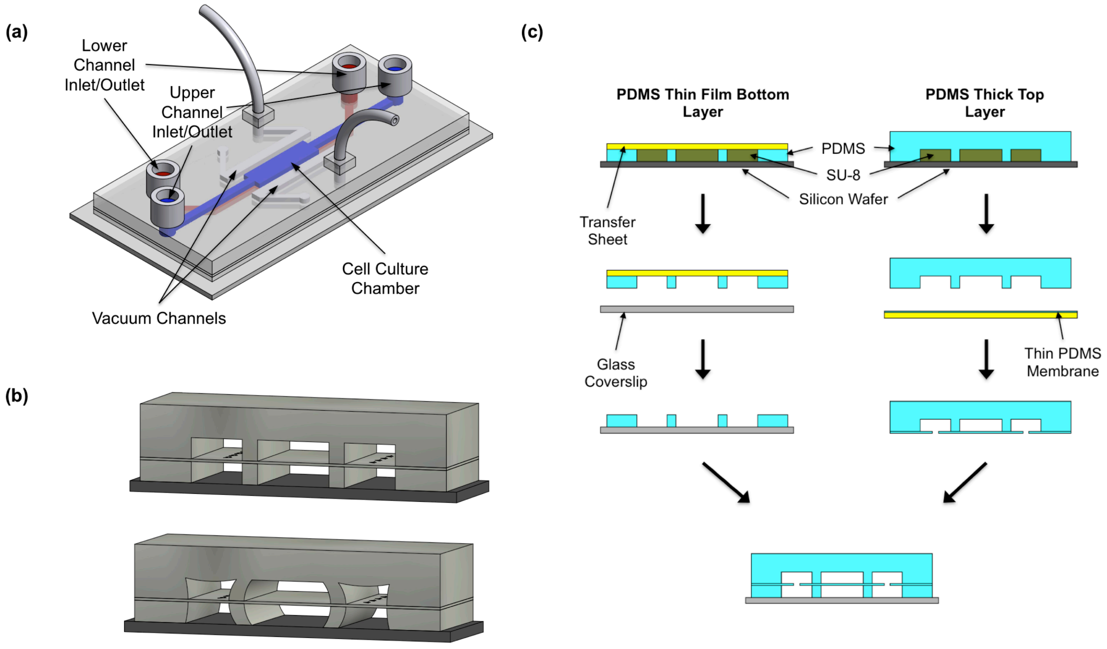

Figure 4.1: Schematic of a microfluidic stretcher device and its fabrication. **(a)** A three-dimensional schematic (not to scale) of the stretcher platform showcases the key device features. **(b)** A cross-sectional view of the device in the relaxed state (top) and stretched state (bottom) after a vacuum has been applied in the outer chambers. **(c)** The fabrication of the device involves constructing a bottom thin-film layer, a thick top layer, and a thin membrane. These components are assembled using plasma bonding and reside on a thin glass coverslip substrate.

4.3 Experimental and FEM Characterization of Device Performance

Both the performance of the stretcher platform and device-to-device consistency were investigated using confocal microscopy. To correlate the induced strain in the stretched membrane of the microfluidic device with the applied vacuum pressure, a Quorum WaveFX spinning disk confocal system equipped with a Nikon Eclipse Ti microscope was employed. Fluorescein isothiocyanate (FITC) was introduced into the upper chamber of the device, rendering the channel features clearly visible when excited by a 491 nm laser line. A stack of images (0.2 μm spacing between planes) was obtained at both the left and right edges of the cell culture chamber using a Plan Fluor 40X objective (NA 1.3) and a Hamamatsu ImagEM EM-CCD camera. Images were obtained from five separate stretcher devices with four different vacuum pressures applied: 0 kPa, 25 kPa, 50 kPa, and 75 kPa. An orthogonal view of each stack was reconstructed using ImageJ, which showcased exactly which plane of the stack represented the bottom of the channel/top of the membrane. The identified "top of the membrane" image in each stack was compared to the corresponding images at different vacuum pressures for a given stretcher device and position. The change in displacement of the outer edge of the membrane for increasing vacuum pressures was then measured. Strain (ε) was computed according to its definition as $\varepsilon = \Delta L/L$, in which ΔL is the combined change in displacement of the left and right sides of the membrane and L is the original width of the membrane (1000 μm). The data for the five devices were averaged and the standard deviation calculated at each vacuum pressure. Examples of these confocal microscopy images are shown in **Fig. 4.2(a)**, and the measured strains are shown in Fig. **4.2(c)**. As demonstrated by the error bars on this plot (representing standard deviation), the strains observed among the five devices were reasonably consistent, which indicates that our fabrication technique of punching holes to balance the vacuum pressures in the upper and lower vacuum channels is an effective approach for constructing stretcher devices with reproducible performance.

In addition to the experimental investigation performed, the stretcher device was also characterized using FEM with COMSOL Multiphysics™. Finite element modeling (FEM) of the stretcher device was conducted using the Solid Mechanics module in COMSOL Multiphysics™. A two-dimensional model was first constructed, mimicking the dimensions of cell and vacuum chambers in the center of the device. Additional analysis using a three-dimensional representation of the device yielded results similar to the two-dimensional model, but required an increased computational load; thus, the two-dimensional model was deemed sufficient for use in this study. A density of 965 kg/m^3 and a Poisson's ratio of 0.45 were chosen for PDMS. Of particular importance in this model is the value chosen for the Young's modulus. A range of Young's moduli for PDMS have been reported in the literature, varying from 12 kPa to 6.61 MPa (Brown, Ookawa, & Wong, 2005; Choi & Rogers, 2003; Gates, Xu, Love, Wolfe, & Whitesides, 2004; Gray, Tien, & Chen, 2003; Liu, Sun, Sun, Bock, & Chen, 2009). The PDMS dimensions, processing conditions, and measurement techniques all appear to affect the determined moduli values in the literature. Thus, in order to more accurately represent the mechanical properties of PDMS in the model, the geometry was divided into three domains with different Young's moduli. In the bulk PDMS areas of the geometry, a modulus of 1.8 MPa was employed, which reflects the modulus reported for large slabs of PDMS (Choi & Rogers, 2003; Gates et al., 2004). However, for the side walls (75 µm thick) and the suspended membrane (10 µm thick), Young's modulus values of 1.14 MPa and 1.9 MPa were chosen, respectively. These values more accurately represent modulus values reported for thinner PDMS components that have been shown to be thickness-dependent (Liu et al., 2009). From this two-dimensional model, the displacement was calculated for various applied vacuum pressures, as shown in **Fig. 4.2(b)**. The extracted strain from the modeling, plotted in **Fig. 4.2(c)**, agrees well with the experimental data obtained using confocal microscopy. Therefore, this two-dimensional model with low computational requirements could be an effective tool for designing future stretchers with different strain and dimensional requirements.

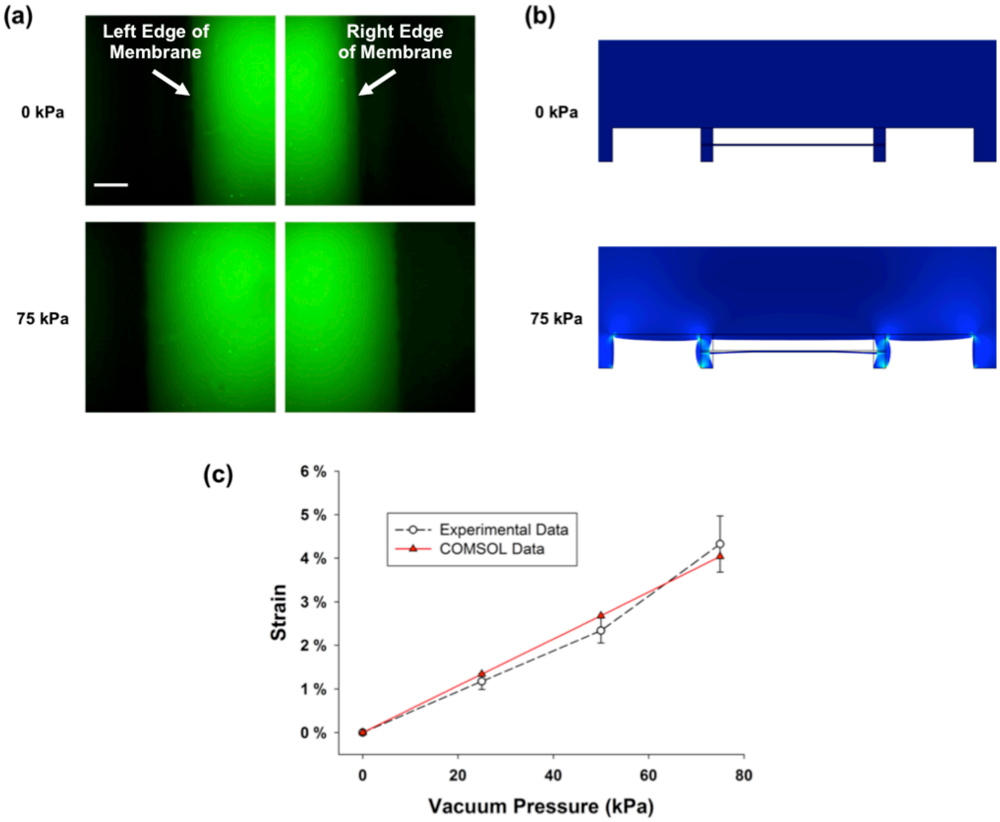

Figure 4.2: Experimental and FEM characterization of the microfluidic stretcher platform. **(a)** Characteristic images of the top of the PDMS membrane under different applied vacuum pressures obtained using confocal microscopy. Scale bar is 20 µm. **(b)** Magnified visualization of the displacement of the PDMS membrane and sidewalls at different vacuum pressures determined using COMSOL Multiphysics™. **(c)** A scatter plot compares the strains observed at different vacuum pressures using both experimental and modeling characterization techniques. The error bars associated with the experimental data represent standard deviation (68% confidence). Five separate devices were tested to generate the experimental data.

4.4 Investigation of NAF/CAF Transformation Using the Stretcher Platform

4.4.1 Biological Methods

NAF and CAF Cell Generation

Human prostatic CAFs and NAFs were prepared as previously described (Olumi et al., 1999). For this study, CAFs and NAFs from five separate patients were used to ensure consistency. Following preparation, cells were qualified using a tissue recombination bioassay to confirm that CAFs induced tumor formation from BPH1 cells and NAFs did not elicit tumorigenesis. Aliquots of CAFs and NAFs were frozen in liquid nitrogen for later use. Cells were used at low passage (less than passage 10) to ensure proper function in ECM production and communication with cancer cells.

Cell Maintenance and Co-Culture in Microfluidic Devices

Prostatic CAFs and NAFs were cultured and maintained in Roswell Park Memorial Institute medium (RPMI) 1640 with 10% fetal bovine serum (FBS) and penicillin–streptomycin as described previously (Ao et al., 2007). Human head and neck cancer cells SCC61 were maintained in Dulbecco's Modified Eagle's /F12 Medium (Life Technology, Carlsbad, CA) supplemented with 10% FBS and penicillin–streptomycin.

A week before co-culture, cancer cells were adapted to RPMI medium gradually. Cell growth and random migration assays were conducted to confirm that there was no significant change due to the medium switch. In each microfluidic device, ~5 x 10^3 NAF cells suspended in 20 μL of RPMI medium were loaded in the inlet reservoir. After incubating ~2 hours at 37°C to allow NAFs to attach to the suspended PDMS membrane, both inlets of the vacuum chambers on the stretcher device were attached to a vacuum line that had been inserted into the incubator. A vacuum pressure of 67.7 kPa was applied, and the device was incubated overnight at 37°C in a cell culture incubator with 5% CO_2. When studying cancer cell migration in the presence of NAFs (both stretched and unstretched), ~5 x 10^3 SCC61 cells labeled with CellTracker^{TM} Green (Life Technology, Carlsbad, CA) were suspended in 20 μL of RPMI and loaded on top of the

NAFs growing inside the devices. The devices were then incubated overnight before being subjected to live-cell imaging. For studies using CAFs, cells were loaded into the inlet reservoir of a simple single-layer microfluidic cell culture chamber with dimensions similar to that of the stretcher platform. However, the cells were plated directly on a glass coverslip, not on a suspended PDMS membrane. Otherwise, tests involving CAFs were carried out identically to those using NAFs.

Immunofluorescence staining

Both CAFs and stretched/unstretched NAFs were fixed with 4% paraformaldehyde in 0.12 M sucrose dissolved in PBS for 15 minutes at room temperature, then permeabilized with 0.2% Triton-X-100 in PBS for 5 minutes at room temperature, and finally blocked in 10% normal goat serum. Platelet derived growth factor receptor α (PDGFRα) expression was probed with rabbit polyclonal antibody (D1E1E, Cell Signaling Technology, Danvers, MA) and followed by Alexa Fluor® 555 goat anti-rabbit secondary antibody (Life technology, Carlsbad, CA). For fibronectin staining, an antibody against fibronectin (610077, BD Bioscience, San Jose, CA) was used, followed by Alexa Fluor® 488 goat anti-mouse secondary antibody (Life Technology, Carlsbad, CA). Primary antibodies were diluted at 1:500 and secondary antibodies at 1:2000 in PBS with 0.2% Triton-X-100. Primary antibodies were incubated for 2 hours; secondary antibodies were incubated for 45 minutes. Excess, unbound antibody was completely washed out of the channel with PBS. The entire staining process was conducted at room temperature.

Microscopy and Live Cell Imaging in Microfluidic Devices

Both fixed and live-cell imaging were performed as described previously (Jean et al., 2013). A Quorum WaveFX spinning disk confocal system was used that was equipped with a Nikon Eclipse Ti microscope, a Plan Fluor 20X objective (NA 0.75), a Plan Fluor 40X objective (NA 1.3), and a Hamamatsu ImagEM EM-CCD camera. To image fixed cells at 40X magnification, the top PDMS layer/membrane was cut and detached from the bottom layer, and the membrane was placed directly on a thin glass coverslip. This allowed for better images at higher magnification using the 40X objective. Images were acquired using MetaMorph software (Molecular Devices, Sunnyvale, CA). For migration assays, images were obtained every 5 minutes for 12 hours. Cells were maintained at 37°C using a temperature-controlled chamber (Live Cell Instrument, Seoul, Korea). CellTracker^{TM} Green and a red fluorophore (Alexa Fluor$^{®}$ 555) were excited with 491 nm and 561 nm laser lines, respectively. Emission filters for these fluorophores were 470/24 and 525/50 (Semrock, Rochester, NY).

Quantification of Fibronectin Alignment and Cancer Cell Migration

To quantify fibronectin alignment, the angles between individual fibronectin fibers were measured to quantify fibronectin alignment. A template with nine points evenly distributed in a round plane was designed as previously reported (Yang, Mosher, Seo, Beebe, & Friedl, 2011). Confocal images of fibronectin were overlaid with the template and then subjected to analysis. For each of the nine points, the fiber closest to the point was identified, and then the intersection angle of the nearest crossing fiber was determined using ImageJ. A minimum of 50 angles were analyzed for each condition.

To quantify directional cancer cell migration, the total migration distance (T) for individual cells was measured from time-lapse images and the net (D) distance was calculated. The directionality index (D/T) was determined by taking the ratio of the net (D) to total distance migrated (T), as previously described (Pankov et al., 2005). Association was determined by calculating the angle σ between the axes of migration of cancer cells and fibroblasts. The association index was defined as the cosine of σ. An association index of 0 denotes cells that are migrating perpendicular to each other, whereas an index of 1 indicates that cells are migrating parallel to each other. Note that for all quantification methods, a Student's t-test was used to determine significant differences in the data.

4.4.2 Results

Effect of Mechanical Stimulus on Fibronectin Organization of NAFs

To observe the effects of mechanical force in the activation of fibroblasts, we first examined the ECM produced by human prostatic NAFs. We employed the microfluidic stretcher device to exert mechanical force on NAFs by loading the cells onto the suspended membrane and then stretching it (**Fig. 4.3(a)**). NAFs cultured on the PDMS membrane were stretched overnight under a consistent strain of ~4%, after which the stress was released and the NAFs were incubated for another ~24 hours before immunofluorescence staining was performed. Incubation for an additional ~24 hours was necessary to allow the fibroblasts time to deposit and assemble enough fibronectin for clear imaging. Note that even though the extra 24 hour incubation period was performed after the stretch was removed, the fibronectin organization discussed below was still observable immediately after releasing the stretch, indicating that it was the stretching mechanical stimulus that initiated the phenotypic change, not the removal of the strain.

Organization of the fibronectin produced by the NAFs that had been stretched was noticeably different from the fibronectin organization from the control, i.e., unstretched NAFs. The fibronectin produced by unstretched NAFs formed a random network, while the fibronectin secreted by stretched NAFs formed a more aligned, linear network (**Fig. 4.3(c)**). As a comparison, we also examined the fibronectin produced by prostatic CAFs (unstretched) and found that the alignment of CAF-produced fibronectin was similar to that produced by stretched NAFs (**Fig. 4.3(c)**). To quantitatively characterize the fibronectin alignment, we calculated the average angle between fibronectin fibers. The results in Fig. **4.3(d)** reveal that the average angle between fibronectin fibers produced by unstretched NAFs is 60.5°, whereas the angle between fibronectin fibers produced by stretched NAFs was 23.5°, which is comparable to the 17.5° average measured for CAFs.

It is worth noting that the fibronectin alignment observed in stretched NAFs was not along the stretch direction, but rather along the long axis of the fibroblasts themselves, which were oriented in a random manner (**Fig. 4.3(b)**). This behavior is different from previous studies showing that fibroblasts exhibit a global alignment perpendicular to the stretch direction (C. Huang et al., 2013; Weidenhamer & Tranquillo, 2013). Most likely, the lack of global alignment could be attributed to two reasons. First, the magnitude of strain applied in our experiments is less than that used for previous investigations (C. Huang et al., 2013). As discussed earlier, varying stretch magnitudes may induce different fibroblast responses (A. A. Lee et al., 1999). Second, a sustained, constant stretch was applied to NAFs in our experiment. In contrast, observations of global fibroblast alignment typically occur upon the application of cyclical stretching (Buck, 1980; Carver, Nagpal, Nachtigal, Borg, & Terracio, 1991; Dartsch, Hämmerle, & Betz, 1986; A. A. Lee et al., 1999; Neidlinger-Wilke, Grood, Wang, Brand, & Claes, 2001; Steward et al., 2011). Thus, both the magnitude and the manner of exerting the stretch may produce different global fibroblast responses. Note that in these experiments, neither immediately after releasing the stretch nor after the 24 hour post-stretch incubation period was global alignment observed. Nonetheless, these results suggest that the altered fibronectin morphology produced by stretched NAFs is not a simple realignment of the fibronectin fibers under the applied mechanical strain to the substrate, but rather a consequence of a mechanical stimulus causing a fundamental biological change in individual fibroblasts.

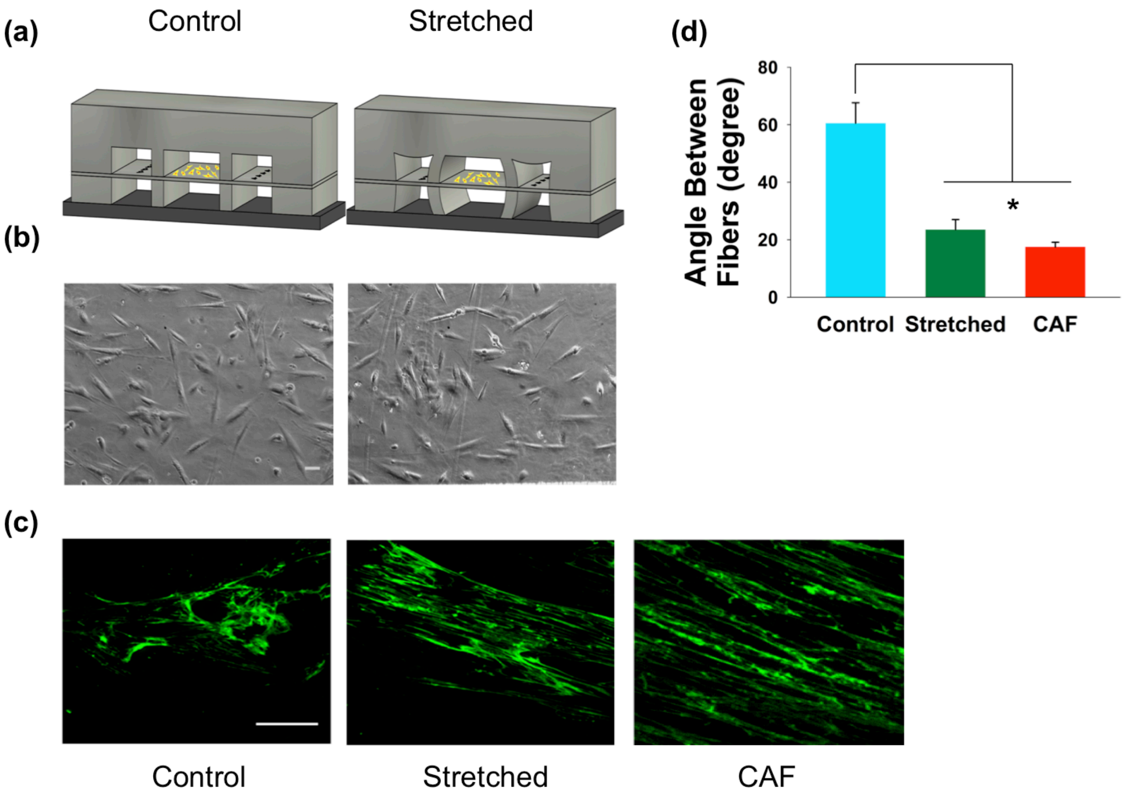

Figure 4.3: Stretched NAFs deposit fibronectin in an organized format. **(a)** NAFs (yellow) were grown in control (unstretched) and stretched devices. **(b)** Representative phase images of NAFs grown in control or stretched devices (after stretching), illustrating the random orientation of the cells attached to the PDMS membrane. **(c)** Characteristic images demonstrating the immunostaining of fibronectin produced by unstretched NAFs, stretched NAFs, as well as CAFs (scale bar is 50 μm). **(d)** Average angles between fibronectin fibers measured as reported (Yang et al., 2011) to compare fibronectin alignment. Both CAFs and stretched NAFs produced fibronectin with smaller angles than the fibronectin produced by unstretched NAFs. Error bars represent S.E.M for 50 cells from three individual experiments (*p < 0.002).

Directed Cancer Cell Migration with Stretched NAFs

The above study of fibronectin morphology indicates that a mechanical stimulus activates NAFs in such a way as to induce more CAF-like fibronectin organization. Concurrently, it is known that modified ECM in the tumor microenvironment facilitates cancer cell migration (Friedl & Gilmour, 2009)**.** That is, cancer cells tend to migrate in the aligned direction of modified ECM. Thus, it is reasonable to ask whether cancer cells co-cultured with stretched NAFs migrate in a manner similar to cancer cells co-cultured with CAFs. To answer this question, we co-cultured cancer cells with stretched/unstretched NAFs and CAFs, and assessed cancer cell migration for each case. A co-culture was set up by introducing equal amounts of SCC61 head and neck squamous carcinoma cells into the devices (after the overnight stretching period for the stretched NAFs trial). From time-lapse microscopy images, SCC61 cells in the stretched device appeared to migrate toward and along the NAFs (**Fig. 4.4(a)**, middle panel), which is similar to that observed in a co-culture of SCC61 cells and CAFs (**Fig. 4.4(a)**, lower panel). In contrast, SCC61 cells do not migrate toward NAFs in the control experiment (**Fig. 4.4(a)**, upper panel). These results suggest that stretching alters the influence of NAFs on the migration of cancer cells. Indeed, quantification shows that SCC61 cells have a higher association index (the cosine of the angle between the migration axes of fibroblast and SCC61 cells) with stretched NAFs and CAFs when compared with unstretched NAFs (**Fig. 4.4(b)**). Moreover, the directional migration index (directionality), which is the ratio of the net (D) to total distance migrated (T), is significantly higher for SCC61 cells cultured with stretched NAFs and CAFs (**Fig. 4.4(c)**). Since one important function of CAFs is to facilitate cancer cell migration, the similarity of cancer cell migration among stretched NAFs and CAFs indicates that stretched NAFs display an important CAF phenotype, which is in contrast to unstretched NAFs. This further underscores the importance of mechanical stress in NAF activation. It is worth noting that the directional migration could be closely related to the aligned fibronectin secreted by stretched NAFs and CAFs, as it has been suggested that the well-organized fibers in the ECM of cancers help promote cancer metastasis (Goetz et al., 2011).

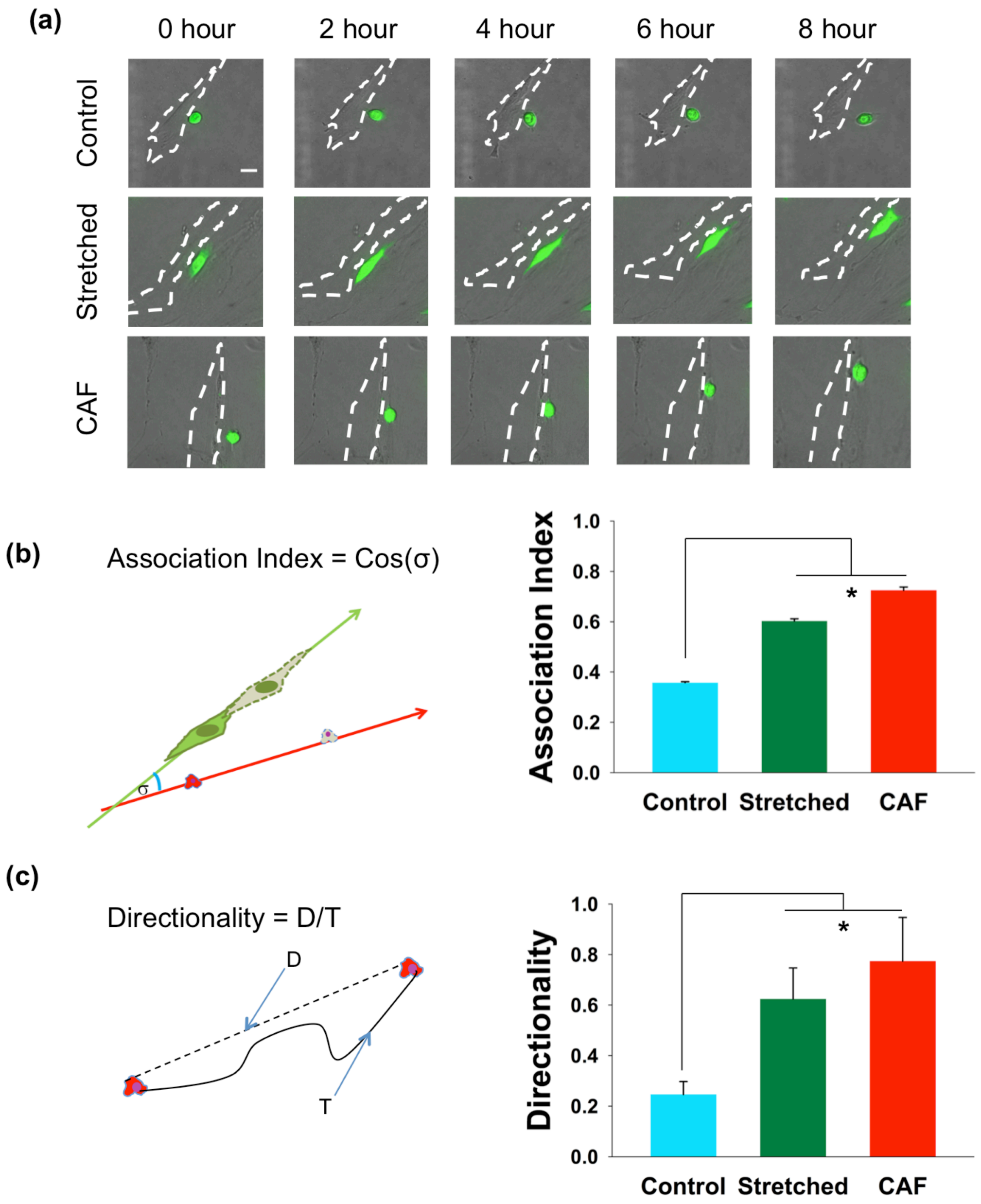

Figure 4.4: Stretched NAFs direct the migration of cancer cells. SCC61 cancer cells (green) were co-cultured with NAFs and CAFs, whose contour is shown with white dashed lines. **(a)** Time-lapse images show SCC61 cells move randomly when co-cultured with unstretched NAFs (upper panel), but they move along stretched NAFs and migrate in a persistent way (middle panel) similar to SCC61 cells co-cultured with CAFs (lower panel). The scale bar is 50 µm. **(b)** Quantification of the association index shows a significant difference when SCC61 cells are co-cultured with stretched NAFs or CAFs vs. unstretched NAFs. Error bars represents S.E.M from 40 cells from six individual experiments (*$p < 0.002$). **(c)** SCC61 cells show a higher directionality migration index when co-cultured with stretched NAFs or CAFs compared with unstretched NAFs. Error bars represents S.E.M from 40 cells from six individual experiments (*$p < 0.001$).

PDGFRα Expression in Stretched NAFs

Our observations indicate that there is no general alignment of the fibroblasts with respect to the stretch direction; however, the deposited fibronectin does form an ordered structure around each fibroblast locally. These results strongly suggest that the applied mechanical stress, instead of simply introducing a direct biophysical response, triggers complex biochemical signaling cascades that affect how fibroblasts construct ECM. To confirm that this is indeed the case, we observed whether there is a biochemical change in stretched NAFs when compared with unstretched NAFs. Particularly, we examined whether stretched NAFs express PDGFRα, a molecule found in reactive tumor stroma (Östman & Heldin, 2007, 2001)**.** We observed a significantly enhanced level of PDGFRα in stretched NAFs as compared with the unstretched controls (**Fig. 4.5**). The expression level of stretched NAFs is very similar to that of CAFs (**Fig. 4.5**), suggesting that the mechanical stress triggered a biochemical response consistent with activation of the NAFs. It is worth noting that even though many biochemical factor changes have been detected from stretched fibroblasts in the literature, we have not found a report showing altered PDGFRα expression in stretched fibroblasts. Therefore, our investigation discloses another biochemical factor that can be affected by mechanically stretching fibroblasts.

The activation of PDGF receptors may directly drive tumor growth via autocrine PDGF stimulation or through receptor mutations. However, it is also possible that the PDGF produced by cancer cells, which typically do not respond to PDGF themselves, may also affect nearby non-tumor cells such as fibroblasts through paracrine signaling (Östman & Heldin, 2007; Pietras et al., 2003). As a result, the enhanced expression of

PDGFRα observed in CAFs and stretched NAFs indicates that PDGF could be an important mediator in activating NAFs exposed to mechanical stress in the tumor microenvironment and in changing NAFs' biological behavior, such as altered fibronectin secretion/organization.

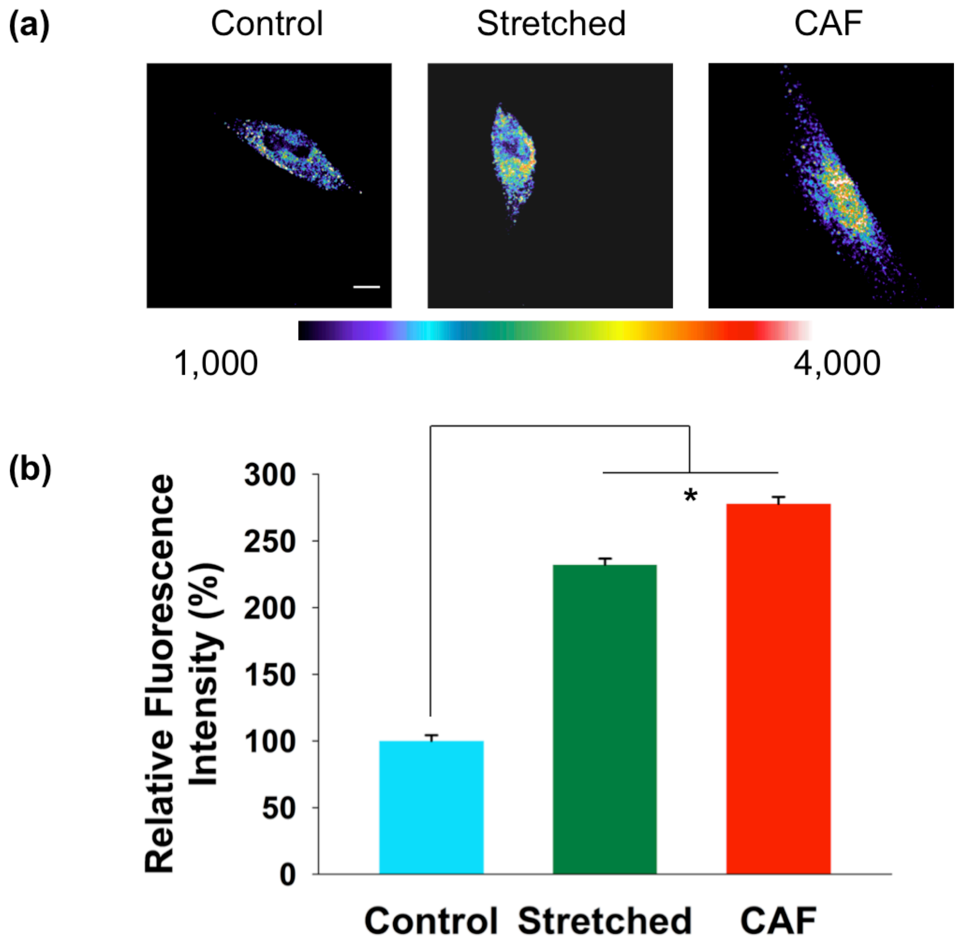

Figure 4.5: Stretched NAFs show higher PDGFRα expression than unstretched NAFs. **(a)** Images are shown in pseudocolor which indicates the range of fluorescence intensities for the assigned color. CAFs and stretched NAFs have higher PDGFRα expression than unstretched NAFs. Scale bar is 50 µm. **(b)** Quantification of PDGFRα expression of unstretched NAFs, stretched NAFs, and CAFs. Error bar represents S.E.M from 40 cells from six individual experiments (*p < 0.005).

4.5 Summary

In summary, we adapted and further improved a microfluidic platform that not only enables repeatable, consistent mechanical stretching of fibroblasts, but also allows for microscopic imaging of cancer cell migration in a co-culture system. We used this platform to study the effects of exerted stress on prostatic NAFs. Results indicate that mechanical force leads to aligned fibronectin in secreted ECM from stretched NAFs. Moreover, co-culture of stretched NAFs with SCC61 cells significantly enhanced the migration association index and directionality. These stretched NAF phenotypes are similar to those exhibited by CAFs but different from those observed in control cells, i.e., unstretched NAFs. Furthermore, we found that the expression of PDGFRα in stretched NAFs is increased to a level that is similar to that of CAFs, indicating that mechanical stress triggers complex biochemical reactions in stretched NAFs. These results provide insight into the important role that mechanical factors may play in NAF activation/CAF genesis. Although biochemical factors have been widely studied in the genesis of CAFs and their interactions with cancer cells, currently little is known about the role that biophysical factors, such as mechanical stress, play in this process. Therefore, the reported study, which examines the important function of mechanotransduction in the tumor microenvironment, should trigger more interest in the role of biophysical effects in the NAF activation/CAF genesis process.

CHAPTER 5

GRAPHENE-BASED MICROFLUIDIC PLATFORM FOR OPTOELECTRONIC PROBING OF SYNAPTIC STRUCTURE AND ACTIVITY

5.1 Motivation

As discussed earlier in this dissertation, neurons communicate with one another through highly specialized junctions called synapses that are composed of pre-synaptic axonal terminals and post-synaptic dendritic regions (M. Shi et al., 2013). The post-synaptic regions may take the form of dendritic spines whose morphology, number, and size can regulate synaptic plasticity and play a role in cognitive functions such as learning and memory (Ethell & Pasquale, 2005). Additionally, numerous neurological diseases and disorders are associated with dendritic spine abnormalities (Chechlacz & Gleeson, 2003; Ferrer & Gullotta, 1990; Z. Li & Sheng, 2003; Smith et al., 2009). Although the importance of spine and synaptic plasticity in both the developing and mature brain is apparent, technological limitations prevent researchers from dynamically probing these structures at the single synapse level and elucidating detailed information about the molecular mechanisms that regulate the morphological changes.

Currently, synaptic activity is primarily investigated using electrophysiology measurements, optical imaging, and multi-electrode arrays. For example, in the patch clamp technique, a micropipette filled with electrochemically conductive saline is sealed to a patch of cell membrane via suction, enabling small currents across ion channels in the membrane to be recorded (Py et al., 2010). Although this electrophysiology technique is a high temporal resolution approach that can detect pico-ampere current, most recording electrodes are too large (greater than 1 μm) to effectively investigate single synapses. Additionally, the patch-clamp process is a laborious process requiring high technical skill (Py et al., 2010). On the other hand, optical imaging techniques that employ fluorescently tagged calcium sensors and voltage sensitive dyes are an effective approach that allows the simultaneous examination of multiple axons/dendrites and synaptic contacts with high spatiotemporal resolution. However, the activity-dependent signal is typically low when compared to the surrounding noise, reducing the practical sensitivity of these methods (Shoham et al., 1999). Multi-electrode arrays (MEAs) are another widely employed strategy for exploring the activity of neurons and neuronal processes. MEA coupled substrates contain a number of planar metallic (usually gold or platinum) electrodes arranged in a matrix on which neurons can be cultured (Biffi et al., 2012). This technique effectively enables the extracellular stimulation and recording of electrical neuronal activity (Claverol-Tinturé, Ghirardi, Fiumara, Rosell, & Cabestany, 2005). However, the opaque nature of gold or platinum electrodes prohibits microscopic observation of the neurons and neurites under investigation, limiting the functionality of the MEA-based microfluidic system. Alternatively, the transparent material indium-tin oxide (ITO) has been used in the fabrication of MEA electrodes (Oka, Shimono, Ogawa, Sugihara, & Taketani, 1999), allowing simultaneous electrical probing and visual observation. However, ITO is a relatively expensive material that is brittle in nature and difficult to pattern, limiting its use with flexible microfluidic components (Wang, Geng, Zheng, & Kim, 2010). Finally, the spatial resolution of these systems is not sufficient for isolating and studying individual synapses and synaptic structures. Therefore, there is an urgent need for a new neurobiological sensing platform that can examine synaptic processes at the single synapse level across neuronal circuits with high spatiotemporal resolution and electrical sensitivity.

Graphene is a two-dimensional material consisting of a monolayer of carbon atoms arranged in a honeycomb lattice structure (Blake et al., 2007; Geim & Novoselov, 2007; Novoselov et al., 2004). Due to its exceptional mechanical and electronic properties and its inherent transparency and flexibility, graphene is an ideal candidate for a new, powerful sensor capable of investigating synaptic structures and processes. In fact, graphene-based probes have the capability of detecting individual adsorbed molecules and measuring electrical and optical events in the time scale regime of tens of picoseconds (Bonaccorso, Sun, Hasan, & Ferrari, 2010; Schedin et al., 2007). In addition, the strength and flexibility of graphene (C. Lee, Wei, Kysar, & Hone, 2008) enable it to adhere well to cell membranes, tissue slices, or other morphologically diverse biological materials, eliminating the thin electrolyte layer between them and increasing the graphene probe's electrical sensitivity. Finally, single layer graphene sheets transmit over 97% of incident light (Nair et al., 2008), making them highly compatible with traditional methods of optical imaging of neurons and neuronal structures (N. Li et al., 2011; Park et al., 2011). All of these unique properties of graphene make it a well-suited material for use in scanning photocurrent microscopy, a technique in which electrons and holes are locally created by photons from a scanning laser spot, producing an electrical current that can be recorded. The magnitude of the induced photocurrent is a direct measure of the local, in-plane electric field at a particular location within the device (Xia et al., 2009) and can vary in value at sites in which structures (such as neuronal processes) interact electrically with the graphene substrate. Graphene-based scanning photocurrent microscopy can also achieve a spatial resolution limited only by the diffraction limit of the laser spot (~500 nm) and uses fast raster scanning to quickly map the photocurrent of a large area, enabling the examination of large neuronal networks with high spatiotemporal resolution. By combining this unique sensing scheme with a version of our previously demonstrated microfluidic neuronal cell co-culture platform (M. Shi et al., 2013), we have developed a graphene-based microfluidic platform for the optoelectronic probing of individual synapses and the monitoring of changes in membrane potential upon chemical stimulation. The initial experiments detailed here demonstrate the viability and potential of this platform for investigating individual synaptic development and activity as well as mapping complex neuronal networks.

5.2 Device Design, Fabrication, and Operation

5.2.1 Design

A schematic showcasing the graphene-based microfluidic scanning photocurrent microscopy platform is presented in **Fig. 5.1**. The device consists of two key components: (1) a multi-layer valve-enabled PDMS microfluidic cell co-culture system and (2) a thin glass coverslip substrate containing patterned gold electrodes covered by a large (~1 cm^2) piece of graphene. The microfluidic component is similar in design to the valve-enabled co-culture system described in Chapter II as well as the microfluidic platform employed in a previously published investigation of the role of glia in neuronal co-culture (M. Shi et al., 2013). This four-chamber valve-enabled microfluidic co-culture device consists of a bottom cell culture chamber layer and an upper pressure control chamber. In the bottom layer, four cell culture chambers are connected by an array of microgrooves 100-500 µm long x 75-100 µm wide x 5 µm tall that can be closed by hydraulically pressurizing the upper control chamber using the connected inlet/outlet tubing. The four-chamber design was chosen to allow for glia co-culture with the neurons, which has been shown to increase neuron transfection efficiency (Majumdar et al., 2011) as well as enhance both the number of synaptic contacts and the stability of formed synapses (M. Shi et al., 2013). Additionally, when pressure is applied, this scheme allows each chamber to be treated in isolation and prevents the microgroove (and photocurrent sensing) regions from being exposed to substrate coatings like PLL and collagen.

For the second component of the system, a series of gold electrodes are patterned on a glass coverslip and covered by a large, single-layer graphene film. As demonstrated in **Fig. 5.1(b)**, the electrodes are arranged in a configuration forming over 20 individual graphene transistors in the microgroove regions with a source electrode, drain electrode, and a connecting graphene layer. In scanning photocurrent microscopy, a laser spot scans over each of these sensing regions, generating photocurrent through the creation of electron-hole pairs. Furthermore, the membrane potential of any neuronal processes in these sensing regions will act as a gate to locally alter the conductance of the graphene, resulting in a local photocurrent change. In this way, a photocurrent map can be constructed of significant neuronal activity in each graphene transistor sensing region (**Fig. 5.2**).

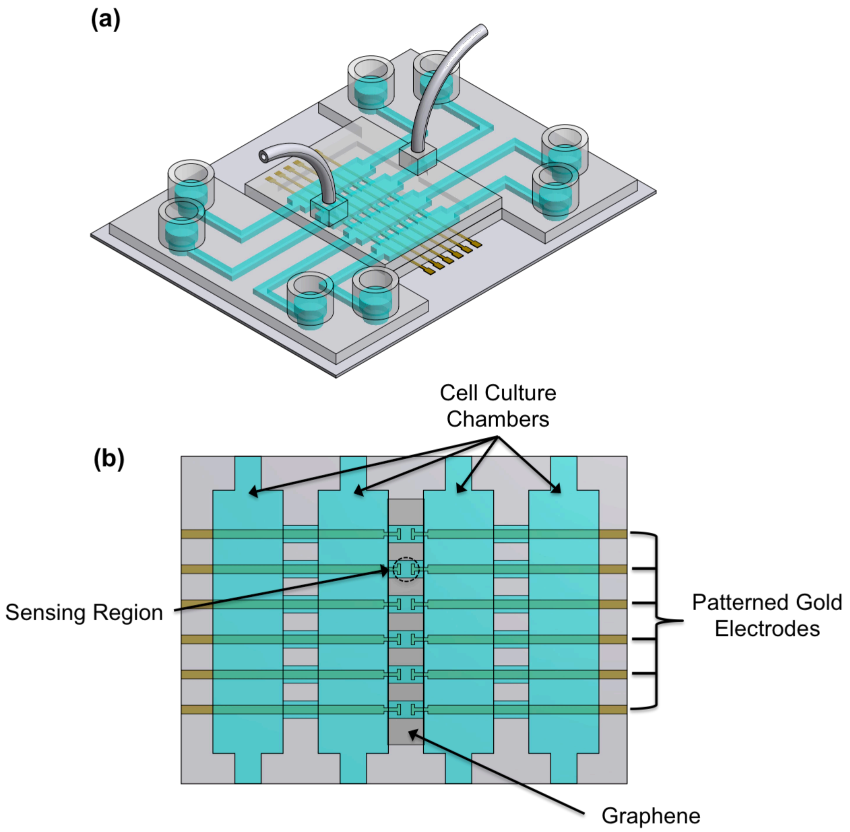

Figure 5.1: Schematic demonstrating the microfluidic graphene photocurrent system. **(a)** A three-dimensional schematic of the assembled microfluidic platform used for photocurrent measurements. **(b)** Detailed overhead view of the cell culture region of the device showcasing the graphene/electrode photocurrent sensing region in the connecting microgrooves.

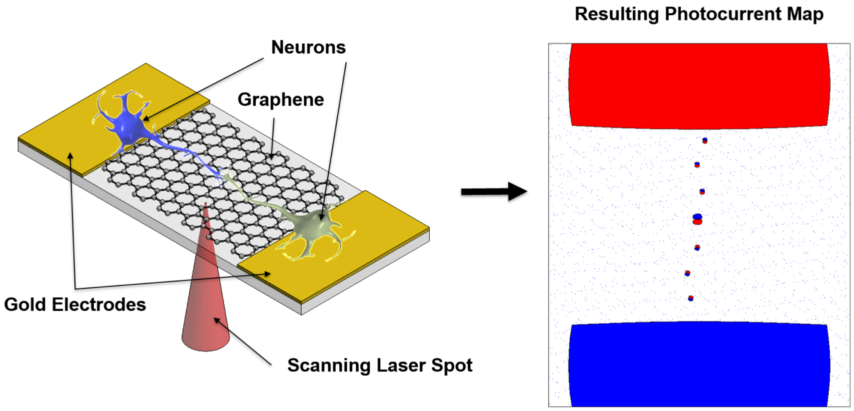

Figure 5.2: Schematics demonstrating the use of the graphene scanning photocurrent microscopy technique to detect neuronal processes and synaptic contacts.

Note that in order to locally induce conductance changes in the graphene, the neuronal processes must be in direct contact with the graphene film. However, for standard primary hippocampal neuronal cultures, PLL (or some other attachment factor) is coated on the substrate before the cells are plated. This PLL layer would obviously prevent the neurites from contacting the graphene, but culturing neurons on bare glass is not an option, as it results in unhealthy, bundled neuronal cell bodies. To solve this issue, the PDMS microgrooves in which the graphene transistors are located can be selectively deformed using hydraulic pressure during the PLL coating protocol (**Fig. 5.3**). The closed microgrooves prevent PLL from covering the majority of the graphene in the sensing regions while still allowing the cell culture chambers to be coated. In this way, the neuronal cell bodies can be healthily cultured in the PLL-coated chambers, leaving the neuronal processes to branch out into the microgrooves and make direct contact with the graphene transistors. The implementation of this innovation is crucial for observing significant photocurrent signal.

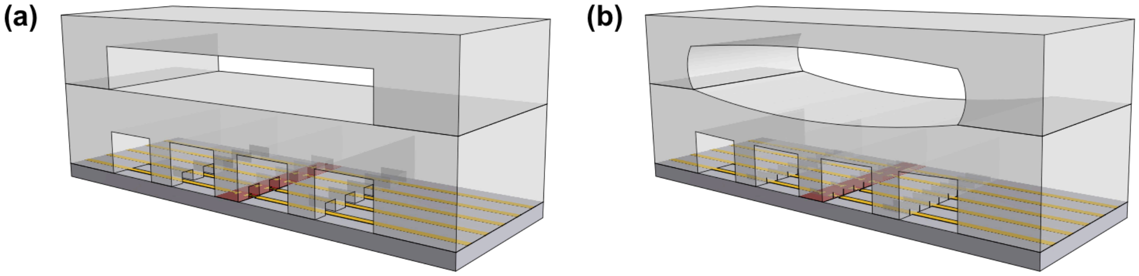

Figure 5.3: Selectively coating PLL in the cell culture chamber regions. **(a)** A cross-sectional slice demonstrating the culture chamber and microgroove regions in the unpressurized state. **(b)** After pressurizing the upper control chamber, the microgrooves will deform and touch the substrate. PLL can then be selectively coated in the cell culture chambers.

An additional design consideration was the orientation of the gold electrodes. As shown in **Fig. 5.1**, the default electrode configuration in the graphene sensing region is characterized by electrodes whose widest edge is perpendicular to both the microgroove sidewall and the direction of neurite growth. Furthermore, the electrodes extend through the center of the microgrooves into the cell culture chamber. We hypothesized that the small height difference between the substrate and top of the gold electrodes (40-100 nm) could result in areas in which graphene was partially suspended. If this were the case, neurons could potentially be sensitive to the changing topography and substrate mechanical properties in those areas, inhibiting healthy growth. To address this possible effect, we changed the location and orientation of the patterned gold electrodes to provide a more unhindered and topographically uniform path on which the neurons could extend processes. In this new approach demonstrated in **Fig. 5.4**, the widest edge of the electrode in the sensing region has been rotated 90°. Additionally, the thicker leg of the electrode is concealed underneath the PDMS barrier between each microgroove, not in the groove itself. This minimizes the total surface area of gold that neurons encounter during growth through the microgrooves. Qualitative observations of the implementation of this technique suggest improved neurite growth and health with the “parallel” electrode configuration. Both configurations were employed for actual photocurrent studies.

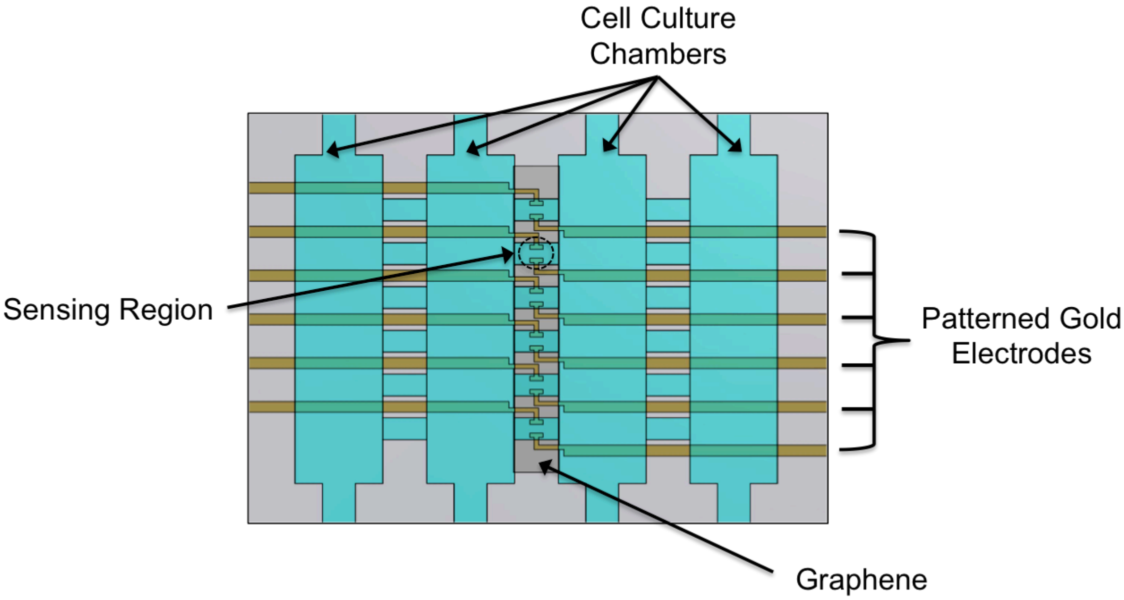

Figure 5.4: Overhead view of the cell culture region demonstrating patterned gold electrodes in the “parallel” orientation.

5.2.2 Fabrication

Fabrication of the graphene-based microfluidic scanning photocurrent microscopy system involves several steps. First, graphene is grown via chemical vapor deposition on a copper substrate using methane as previously described (X. Li, Cai, et al., 2009). Then, using a wet transfer method (X. Li, Zhu, et al., 2009) that employs a thin coating of polymethyl methacrylate (PMMA) as a transfer film, the graphene is placed on a glass coverslip on which gold electrodes have been patterned using standard photolithography and e-beam evaporation techniques. After transfer, a series of washes with acetone, isopropyl alcohol, and DI water is performed to remove the PMMA layer. The next fabrication step involves constructing the PDMS microfluidic channel layers. Standard soft lithography methods similar to those described in previous chapters are utilized to create the four-chamber valve-enabled microfluidic co-culture device components consisting of a bottom cell culture chamber layer and an upper pressure control chamber. However, one key modification was required for this particular device design: the bottom PDMS cell culture chamber layer was cured at room temperature over several days, not the typical 2 hours in a 70°C oven. A thermal expansion coefficient mismatch between PDMS and the SU-8 mold results in PDMS features that are slightly smaller than the dimensions of the master mold. Thus, room temperature curing of the bottom PDMS layer is necessary to produce accurately dimensioned features, enabling proper alignment between the PDMS microgroove channels and the patterned gold electrodes of the glass substrate. Clean, well-aligned placement of the graphene transistors in the microgrooves is essential for directing neurite growth over the photocurrent sensing regions.

After the two PDMS layers are fabricated, they are assembled into a single piece (along with PDMS tubing supports) using air plasma bonding; access "windows" are then cut into the edges of the device to allow for later wire bonding of the gold electrode contact pads. The next step is to plasma bond the PDMS microfluidic device to the graphene/electrode patterned glass substrate. Note that only the PDMS layer is plasma treated in this process, as the air plasma treatment will etch away the graphene on the coverslip and ruin the device. After plasma treatment, the PDMS device is placed on the sample holder of a custom alignment microscope (**Fig. 5.5**). This microscope employs a micrometer stage capable of manipulating the graphene/electrode substrate by both rotation and translation in all three dimensions. A separate X-Y-Z micrometer stage allows for the independent control of the objective position. Together, the microscope system can be used to precisely position the graphene transistors on the glass substrate underneath the suspended PDMS layer before bonding the two components by raising the stage and bringing the substrate into conformal contact with the PDMS.

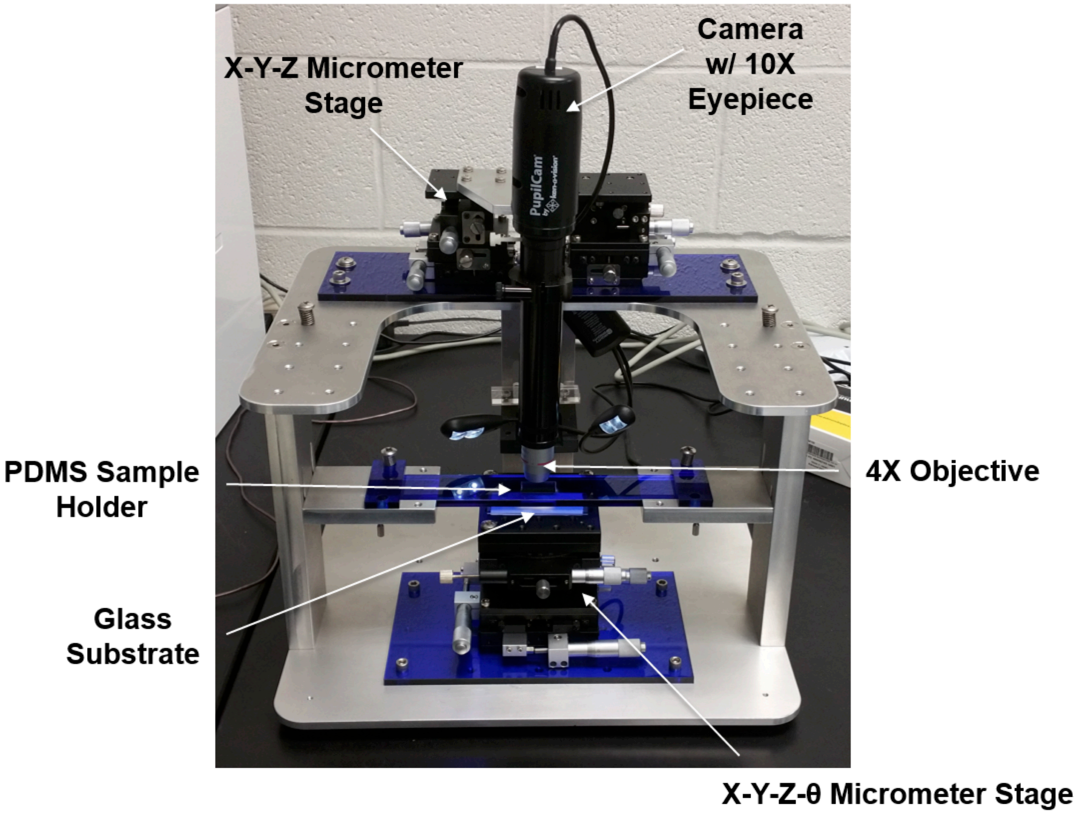

Figure 5.5: Photograph of the custom built alignment microscope.

The bond holding the two device components together is not as strong as a typical plasma bonded PDMS-glass interface primarily because of two reasons: The coverslip was not plasma treated, and the alignment process results in several minutes elapsing between plasma treatment of the PDMS and actual bonding with the glass. A stronger bond is preferred in order to better prevent device leakage, particularly when the control chamber is pressurized. To address this concern, we developed a modified version of the plasma bonding protocol in which a thin film of water is applied between the plasma treated PDMS and the glass substrate and then allowed to evaporate in an oven. As shown in **Fig. 5.6**, the rupture pressure for a plasma treated PDMS chamber bonded to an untreated glass coverslip is significantly larger when a film of water is applied between the two layers (versus a typical dry bond). This data is also qualitatively reinforced by the observation that dry bonded PDMS could be cleanly peeled from the glass, whereas the water bonded PDMS was difficult to detach without ripping the PDMS. To take advantage of this effect for our device fabrication, a small volume of water was pipetted into each inlet/outlet after the initial alignment bond. Then, the edges of the bottom PDMS layer were gently lifted using a scalpel to allow water to flow in between the PDMS and glass substrate. Note that special care was taken not to disrupt the precisely aligned cell culture chamber region. Next, Pyrex reservoirs were attached to each inlet/outlet as previously described, and the device was placed in a 70°C oven until all of the excess water evaporated (> 1 hour), after which the device was removed from the oven and each reservoir filled with ~200 μL of water. The device was then placed in a vacuum to remove any trapped air from the channels. Finally, tubing was attached to the tubing supports as previously described, and the PDMS glue was cured at 70°C for at least an hour to complete the device fabrication.

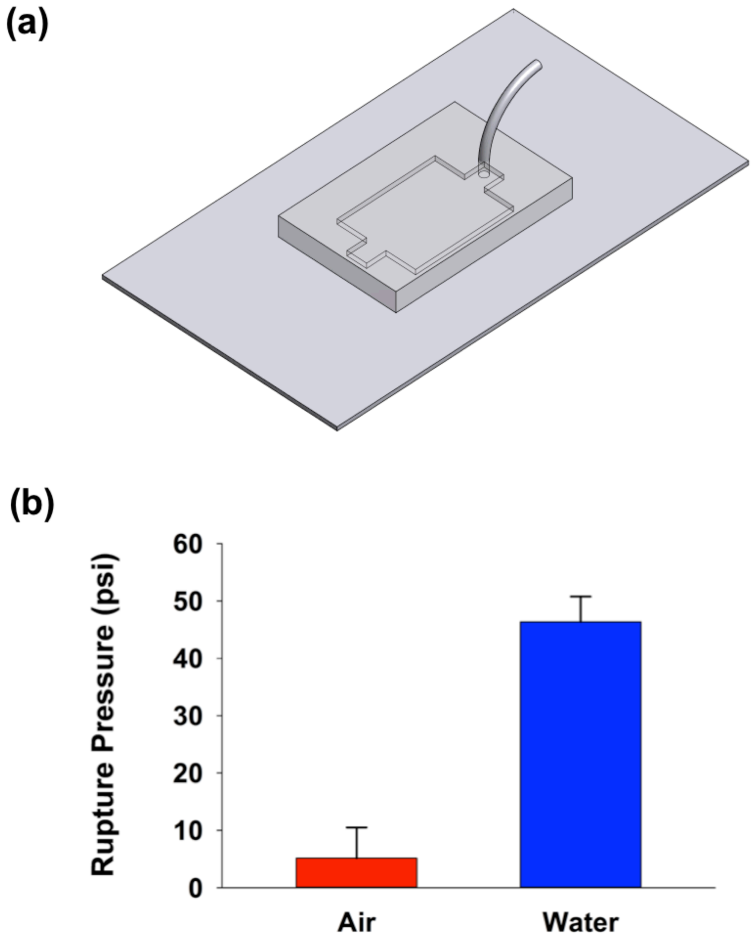

Figure 5.6: Plasma bonding with a delay between treatment and attachment is enhanced by a thin lubricating water layer. **(a)** A three-dimensional schematic depicting the water bonding test setup. A PDMS pressure chamber was bonded to a glass coverslip and pneumatically pressurized via the attached tubing. **(b)** The water bonding technique results in a rupture pressure ~9 times greater than air bonding when attaching a plasma treated PDMS layer to an untreated glass coverslip ten minutes after plasma treatment. The data represents the average of four independent trials, and the error bars are standard deviation.

5.2.3 Operation

General Protocol

Although the graphene-based microfluidic optoelectronic platform can be used for a variety of neurobiology studies and experiments, the following general protocol steps were required in all of our studies. After fabrication, the device was sterilized via UV exposure and all channels and reservoirs were filled with sterile DI water. Next, the control chamber was hydraulically pressurized to separate all four channels and to protect the microgroove areas as described above. The two outer glia channels were then coated with collagen, and the two inner neuron channels were coated with PLL. After coating, glia were loaded and cultured for 3-5 days to reach confluence. Then neurons were loaded into the device as described in Chapter II. The cells were then co-cultured for several days, after which the neurons were transfected with the desired probes and/or transfection proteins.

Once neurons had been cultured in a device between 8 and 13 days, they were ready for examination using confocal fluorescence microscopy and scanning photocurrent microscopy. Using confocal microscopy as previously described, the neuronal processes in each graphene transistor sensing area were inspected. Typically, six to ten transistors on which the healthiest neurites (with obvious spines and protrusions as evidenced by the fluorescence images) were found were noted for more detailed study using scanning photocurrent microscopy. The gold bonding pads for each of these electrodes were then wire bonded to a custom sample holder that serves as an interface to the scanning photocurrent system. Finally, scanning photocurrent microscopy was conducted to investigate the neuronal processes in each graphene sensing region and to explore the desired neuronal phenomena.

Special Considerations for Cell Culture in the Graphene-based Microfluidic Optoelectronic Probing Platform

In the course of developing the operational protocol for the graphene scanning photocurrent microscopy experiments, a couple of unique issues were encountered that were either detrimental to the health of the cells or prevented the device from working properly. First, we observed that a high rate of cell death resulted in limited or even no photocurrent signal from neuronal processes observed in the sensing region using fluorescence microscopy. The high rate of cell death was associated with the use of an alternative transfection protocol employing a higher transfection efficiency Rat Neuron Nucleofector® kit (Lonza, Switzerland), implemented in an effort to improve the likelihood of transfected neurites growing onto the graphene sensing region. Although this technique did result in a higher percentage of transfected neurons, the percentage of neurons that were damaged or killed also increased. As a result, more non-living cellular debris was found in the microfluidic device cell culture chambers and microgrooves. The debris did not prevent healthy neurons from developing and producing spine-bearing neurites, but it did lead to an absence of detectable scanning photocurrent signal. We speculated that the waste material accumulated in the microgroove areas, forming a film on top of the graphene transistor sensing region. This film effectively separated the neuronal processes and the substrate, preventing the neurites from inducing detectable conductance changes in the graphene. In fact, examination of the transfected neuronal processes using confocal microscopy revealed that the focal planes of the patterned gold electrodes and the neurites were significantly different, sometimes by a couple of microns. This observation further suggested that the neurons were growing on top of a layer of debris, and not directly on the graphene. Consequently, we abandoned the alternative transfection protocol and reverted back to the standard transfection procedure that reduced cell death and resulted in cleaner graphene sensing regions. A comparison of different focal planes for a "junky" graphene sensing region is presented in **Fig. 5.7**.

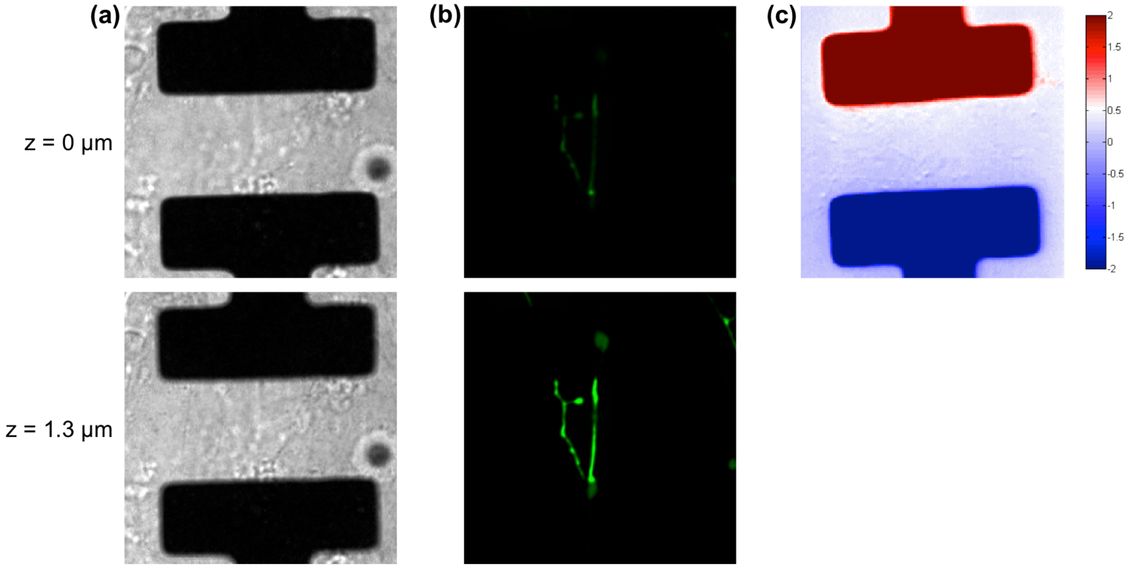

Figure 5.7: Photocurrent response for neurites not in contact with the graphene transistor. **(a)** DIC images of the sensing region at the reference electrode plane (z = 0 μm) and at a plane 1.3 μm above the electrodes. **(b)** Fluorescence images of the same location showcasing the GFP transfected neurites at the reference electrode plane and at the plane in which the neurites exhibited the best focus and fluorescence intensity (z = 1.3 μm). Note that for both DIC and GFP images, the brightness and contrast settings are identical for images from both planes. **(c)** Scanning photocurrent map of the sensing region demonstrating a lack of photocurrent signals in the areas containing neuronal processes.

The second quandary we encountered while developing the operational protocol involved the health of the supporting glial cells in the microfluidic device. As mentioned earlier, culturing glia with neurons can improve neuron transfection efficiency and increase both the number of synaptic contacts and the stability of formed synapses. Glial cells also serve to provide inflammatory support for neurons, and as such are typically a robust cell type. Thus, the degradation of glial health in our graphene-based microfluidic platform was unexpected. In fact, glia had been cultured problem-free in a similar four-chamber microfluidic system for a previous study and in the graphene-based microfluidic platform for several months of experiments before any health issues were observed. Additionally, plating glia from the same batch that had cell death issues in traditional cell culture dishes did not result in any unusual behavior. However, since unhealthy glia are detrimental to the neurons in the microfluidic device, they eventually lead to neuronal death. Therefore, in order to proceed, both the specific problem and a solution for culturing healthy glia in the device needed to be identified. After troubleshooting for three months, the source of the problem was determined to be an anomaly in the harvesting and loading of glia into the microfluidic device. The standard protocol involves retrieving glial cells from rat pup brains and freezing individual aliquots in a solution containing 10% DMSO for later use. Then, each individual aliquot can be thawed and pipetted directly into the microfluidic device (or cell culture dish). Now, for many cell types that are frozen for later use, the thawed aliquots are centrifuged before use to separate the cells and supernatant. The supernatant can then be removed and the remaining cells suspended in culture media. However, in the case of glia, there was concern that the centrifuge process could damage the glia, so this step was skipped and the cells were pipetted directly from the thawed aliquot vial. Using this method, the glia in the devices began degrading 4-5 days after loading them. Again, the glia were plated in the cell culture dishes using the same protocol, with the exception of one key difference: the volume of media added to the dishes after plating is on the order of several mL, whereas the volume of media accessible by glia in the microfluidic chambers is on the order of a few μL. Thus, it is reasonable to assume that the greater dilution used for glia in culture dishes was responsible for maintaining their health. Likely, an anomaly occurred during the process of extracting glia from the rat brains, resulting in the cells being frozen in a solvent that was exceptionally toxic to the cells. Once this issue was identified, two solutions were implemented to resolve it. First, glia were plated in culture dishes directly from the frozen vial, then transferred to the microfluidic devices. In this way, the "toxic" anomaly could be diluted to the point of insignificance. Alternatively, the traditional technique of centrifuging the cells and replacing the supernatant with fresh media was attempted with glia. A visual comparison of the two new techniques with the direct loading from a thawed frozen vial approach is presented in **Fig. 5.8**. The direct loading from a thawed frozen vial method resulted in a high rate of cell death after six days. However, both of the alternative techniques resulted in healthy glia after six days, indicating that the centrifuge method is not too detrimental to the glia, and both approaches could be used should future batches of frozen glia exhibit the same health difficulties. Although both of the above-described unique issues encountered in the development of the graphene-based scanning photocurrent microscopy protocol were initially a source of perplexity, the process of identifying the specific problems and constructing effective solutions provided enhanced operational acumen for future studies.

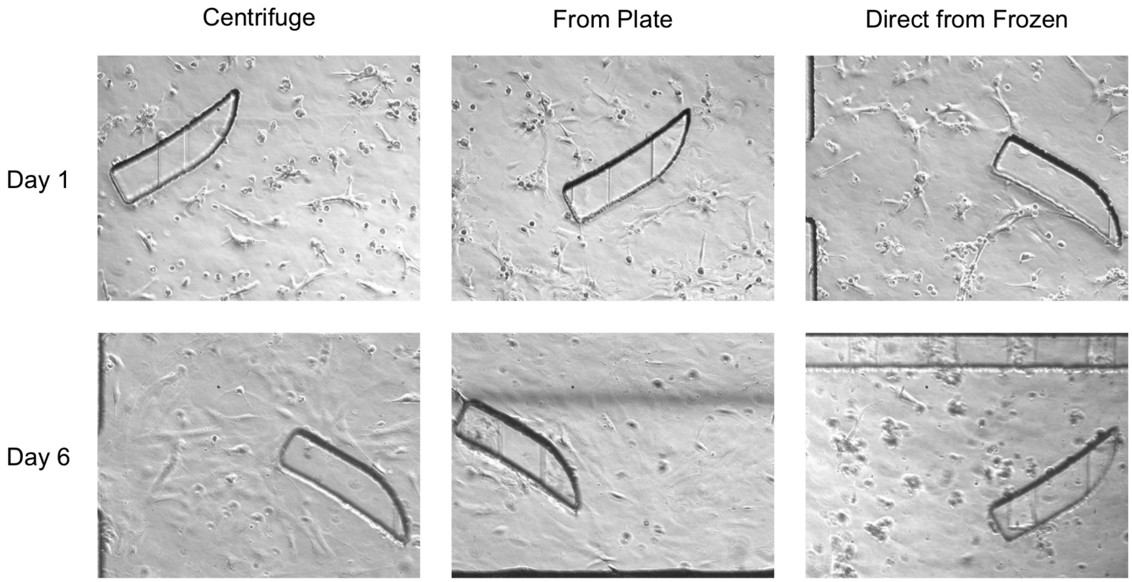

Figure 5.8: Qualitative cell viability comparison of the centrifuge, plating, and direct from frozen techniques for preparing glia for device loading. Representative images of glial cells in the graphene microfluidic platforms are presented both one day and six days after loading.

5.3 Experimental Results

5.3.1 Scanning Photocurrent Microscopy for Mapping Active Spine and Synapse Locations

In order to establish the feasibility of the graphene-based microfluidic optoelectronic sensing platform, we first attempted to demonstrate a photocurrent map that corresponded spatially with fluorescence images of neuronal processes in the same sensing region. To accomplish this, the general protocol described in the previous section was used to co-culture neurons and glia in a graphene-based microfluidic device. At the transfection stage, one neuronal chamber was transfected with GFP (for visualizing dendritic protrusions), and the other chamber was transfected with mCherry-synaptophysin (a pre-synaptic marker). After several more days in culture, confocal microscopy and scanning photocurrent measurements were performed; the resulting photocurrent map and corresponding optical images of one of the graphene transistor regions in the device are presented in **Fig. 5.9**.

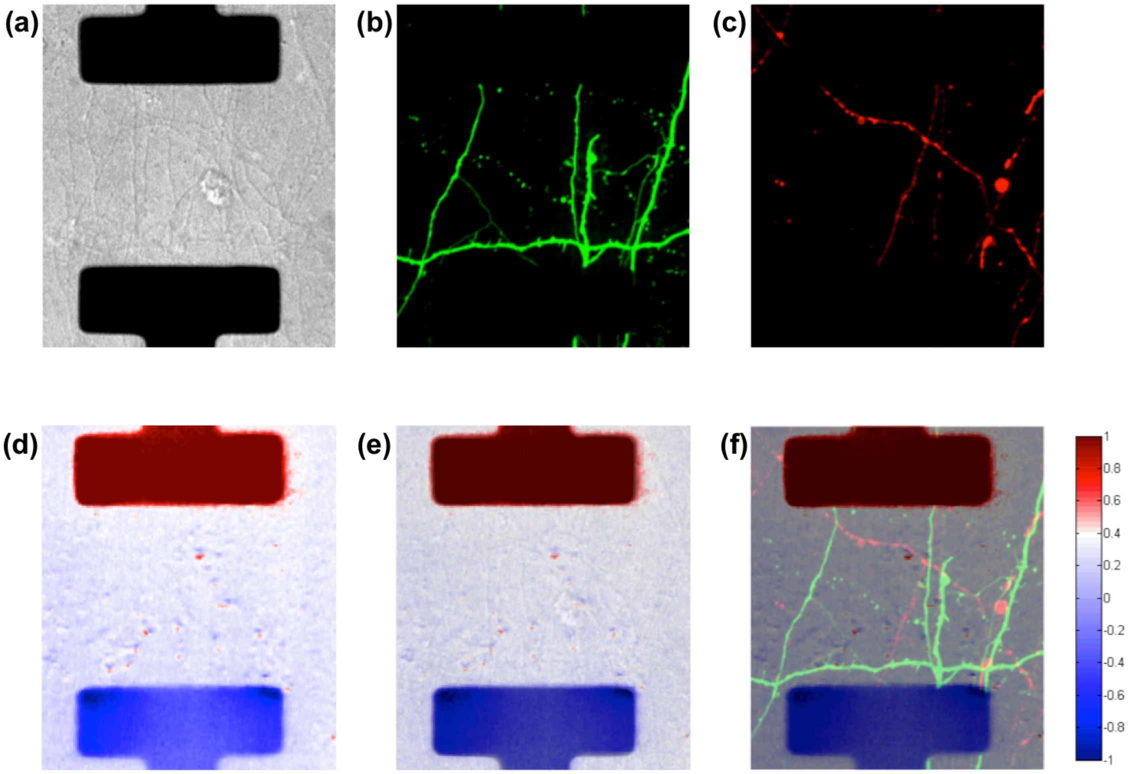

Figure 5.9: Mapping dendritic spines and synapses using scanning photocurrent microscopy. **(a-c)** Confocal microscopy images focused on a graphene transistor region of the microfluidic device show the location of neuronal processes and dendritic spines in **(a)** DIC, **(b)** GFP, and **(c)** mCherry-synaptophysin images. **(d)** Scanning photocurrent map of the same graphene transistor region reveals the location of the polarized, high-intensity photocurrent "dots" in the area between the gold electrodes. **(e)** Overlay of the photocurrent map with the DIC image. **(f)** Overlay of the photocurrent map with a combined GFP/mCherry-synaptophysin image.

In the overlays of the photocurrent map with both the DIC and fluorescence images in **Fig. 5.9**, an overlap of localized "dots" of high photocurrent intensity with neuronal processes/features can be noted. Closer inspection of the images reveals three key observations. First, not all photocurrent dots appear to match up with areas of GFP or mCherry-syanptophysin fluorescence. However, most of the dots do align with neuronal features detailed in the DIC image. This indicates that the relatively low transfection efficiency typically achieved in our microfluidic neuronal cultures (< 25%) results in non-transfected cells producing significant photocurrent signal in the sensing region. Next, not all spines, processes, and regions of synaptic contact seen in the confocal microscopy images produce significant photocurrent signals. One potential explanation for this is the previously mentioned photocurrent detection requirement of close contact between the graphene and neuronal processes. Even minute topographical variations in a neuronal process could result in areas with a gap of several nanometers that would screen the neurite from the graphene substrate and inhibit local changes in conductance. Thus, not all locations with spines and protrusions would necessarily produce a significant photocurrent signal. The final observation is that the size and intensity of the strong photocurrent dots appear to vary within the mapping area. Several factors could contribute to this inconsistency among photocurrent dots including the actual sizes of the different neuronal features, variance in the local membrane potential at different locations, and incomplete or partial contacts between the neuron and the graphene. Nonetheless, although a perfect one-to-one correspondence between the photocurrent map and optical images was not achieved, the results of this experiment do indicate the potential of this microfluidic platform for investigating synaptic activity at the single-synapse level using scanning photocurrent microscopy.

5.3.2 Observation of Local Membrane Potential Changes

General Approach

The next step toward evaluating the capability of the graphene-based microfluidic scanning photocurrent microscopy platform was to use the system to probe electrical activity of individual spines and synapses. Again, the standard cell culture protocol was followed to generate a healthy neuron/glia co-culture in the device. However, the transfection protocol was modified for this study. In both neuronal cell culture chambers, mCerulean was transfected as a filler alongside GFP-GCaMP6s, a GFP-tagged fluorescent Ca^{2+} indicator. Ca^{2+} indicators are widely used to measure synaptic input, as glutamate receptor activation during synaptic transmission leads to Ca^{2+} transients in dendritic spines (Takechi, Eilers, & Konnerth, 1998). With this type of Ca^{2+} probe, electrical activities of synapses occurring in response to a global stimulus can be probed by monitoring changes in fluorescence intensity. Now, just as described in the previous section, neurons in the device were cultured for several days after transfection, followed by imaging using confocal microscopy and scanning photocurrent microscopy. The resulting data were examined to determine which graphene transistor in the device had the best combination of fluorescence imaging, photocurrent signal, and overlap between the two. Then, chemical stimulation of the neuronal membrane potential was performed (described below), and the transistor region was monitored using both scanning photocurrent and fluorescence microscopy. In this way, any observed photocurrent signal alterations in response to the membrane potential changes could be compared with corresponding changes in fluorescence intensity of the GFP-tagged Ca^{2+} indicator.

Chemical Stimulation Protocol

Chemical stimulation was achieved by perfusion of Hank's Balanced Salt Solution (HBSS) containing a higher-than-normal potassium ion (K^+) concentration into the neuron culture chambers and microgrooves. The high K^+ concentration served to depolarize the neurons, triggering electrical activity. By cycling the media in the microfluidic device with buffers of high and low K^+ concentration, the photocurrent and fluorescence intensity response to changing membrane potentials could be elucidated. However, the media exchange in our microfluidic system is non-trivial when compared to switching media in single channels or traditional cell culture dishes. The graphene photocurrent microfluidic device is accessible by multiple inlets/outlets and consists of four channels of non-uniform dimensions connected by arrays of microgrooves. Thus, achieving flow perfusion that could be effective in producing the desired cyclical chemical stimulation requires careful analysis and experimental testing.

Fluid flow in microfluidic systems can typically be characterized by the Hagen-Poiseuille law $\Delta p = R_{hyd}Q$ where Δp is the pressure drop, Q is the flow rate, and R_{hyd} is the hydraulic resistance. Although in our microfluidic platforms the pressure drop is primarily determined by the difference in height between the media in the inlet/outlet reservoirs, any disparity in the shape of the media menisci in each reservoir can also affect the flow because of surface tension effects. The problem is further complicated by the varying sizes of the channel/chambers, making it difficult to precisely predict the flow resistance. Moreover, eight total inlets/outlets result in a number of potential flow paths that must be considered.

To simplify the problem, we consider two essential goals in the experimental design process. One goal is that new media added to the system should perfuse throughout the majority of at least one neuronal cell culture chamber and throughout the entire microgroove region; the second requirement is that the process should occur in a reasonably short time period (on the order of single minutes). With these guiding principles in mind, consider two flow paths: one from the inlet of neuron channel A to the outlet of neuron channel A ($P_{A\text{-}A}$) and the second from the inlet of neuron channel A to the inlet or outlet of neuron channel B ($P_{A\text{-}B}$). Assume all reservoirs are empty except for the inlet of neuron channel A, to which 300 μL of media has been added. Using the fact that for a straight rectangular channel (Bruus, 2008)

$$R_{hyd} = \frac{12\eta L}{1-0.63\left(\frac{h}{w}\right)}\left(\frac{1}{h^3 w}\right) \tag{5.1}$$

where L is the length of the channel, h is the channel height, w is the channel width, and η is viscosity, the hydraulic resistance for $P_{A\text{-}A}$ can be calculated to be about an order of magnitude less than that of $P_{A\text{-}B}$. This translates into a $P_{A\text{-}A}$ volumetric flow rate roughly an order of magnitude greater than that of $P_{A\text{-}B}$. Thus, the media will clearly perfuse through neuron channel A more quickly than it would through neuron channel B. Importantly, the calculated flow rates result in flow velocities throughout both flow paths ranging from hundreds of microns per second to millimeters per second. Therefore, the perfusion scheme presented here should result in sufficient flow and complete media exchange in the desired time frame.

To confirm that the above analysis is valid, a test microfluidic device was monitored under a low-resolution optical microscope as 300 μL of dye was added to a single inlet reservoir. The time evolution of the cell culture region of the device is presented in **Fig. 5.10**. Note that the length, width, and height of the microgrooves in this device are 200 µm, 100 µm, and 5 µm, respectively. As shown in the figure, perfusion of the dye in the majority of both neuron chambers and the microgrooves is clearly achieved within a minute of loading the dye. Thus, this perfusion method can be implemented as a valid means of chemically stimulating neurons in our graphene photocurrent microfluidic system.

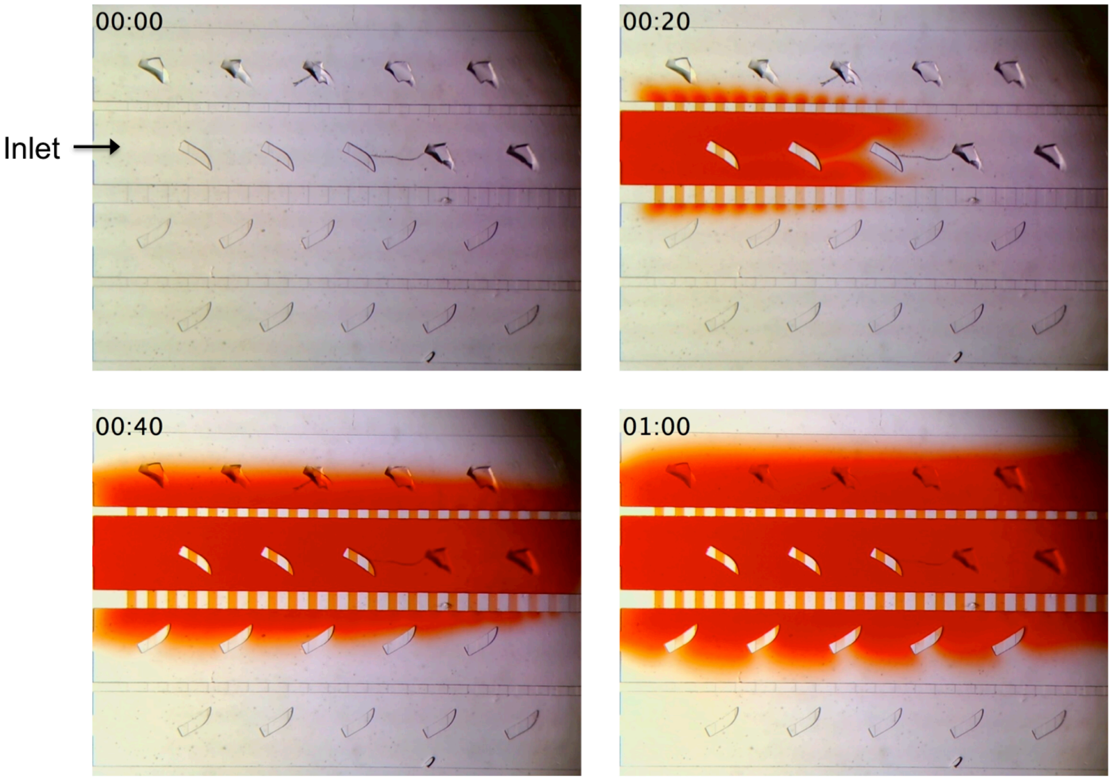

Figure 5.10: Demonstration of media perfusion in the four-chamber microfluidic device. 300 µL of dye was added to the channel marked “Inlet” at time 00:00. Images were captured periodically demonstrating the flow of dye through the two inner neuron chambers and the connecting microgrooves.

For actual stimulation experiments, the general operational protocol was as follows. Before the initial photocurrent mapping, 4 mM K^+ concentration HBSS was loaded into the device. This concentration is similar to the actual neuronal culture media used during the cell culture phase of the experiment and served as the reference. Then, excess media was removed from all inlet/outlet reservoirs and baseline photocurrent maps and fluorescence images were obtained. Next, 300 μL of 60-90 mM K^+ concentration HBSS was added to one of the neuron channel inlets. After 30-60 seconds, photocurrent maps and fluorescence images were taken, followed by the removal of media from all inlets/outlets. Then, 300 μL of 4 mM K^+ media was added to all of the neuron channel inlets to remove the high potassium concentration media from the neuron channels and microgrooves. The next round of photocurrent maps and fluorescence images could then be obtained. This process was repeated for as many cycles as desired. After completion of the stimulation experiment, the resulting data were processed and analyzed for any changes in photocurrent and fluorescence intensity with each stimulation cycle.

Stimulation Results

Using the above-described operational protocol, three different stimulation experiments were performed. First, in order to ensure that the GFP-tagged Ca^{2+} indicator changed in fluorescence intensity upon chemical stimulation in our microfluidic platform, a test device was chosen that exhibited healthy, transfected neuronal processes in the microgroove region. In this device, a stimulation cycle was performed and fluorescence images were obtained with each concentration change. For this stimulation test, no photocurrent measurements were taken. Representative images for one stimulation cycle are presented in **Fig. 5.11(a)**. From this figure, the increase in fluorescence intensity between the baseline 4 mM K^+ image and the depolarized 90 mM K^+ image is apparent. Likewise, the increased fluorescence intensity is reduced back toward the baseline level when 4 mM K^+ concentration media is reintroduced into the device. It is worth noting that the observed increase in intensity is not uniform throughout the neuronal processes, but rather appears to mostly aggregate around spines and protrusions. This observation is reasonable considering that synaptic transmission is responsible for the increased presence of Ca^{2+}. Nonetheless, this fluorescence test confirmed both the effectiveness of the Ca^{2+} indicator in visualizing changes in synaptic activity and the efficiency of the flow perfusion scheme.

A second test was performed on a device in which clear photocurrent signal features were observed but only aligned with neuronal processes in the DIC image and not with any neurites transfected with fluorescently-tagged proteins. For this scenario, we obtained high resolution maps that were focused on a couple of photocurrent dots for each stage of the stimulation cycle. A summary of one stimulation cycle is shown in **Fig. 5.11(b)**. In this test, 60 mM K^+ was chosen as the stimulation concentration. As seen in the figure, the two photocurrent dots reduce in size and intensity when 60 mM K^+ media is added. When 4 mM K^+ is re-added, the size and intensity of the dots return to a state similar to the baseline. The observed photocurrent signal change is likely the result of an increase in the local membrane potential in response to the depolarizing chemical stimulus. This increase in membrane potential will result in the local reduction of photocurrent intensity on the p-type graphene transistor. Subsequently, the reduction in membrane potential upon removal of the high K^+ concentration media allows to photocurrent intensity to return to a higher value. Nevertheless, regardless of the manner of change, this test demonstrated that the developed chemical stimulation protocol does indeed produce detectable and consistent changes in the photocurrent signal.

Finally, we simultaneously probed changes in fluorescence intensity and photocurrent signal upon chemical stimulation of the neurons in the microfluidic device. The results of a stimulation cycle for two photocurrent dots aligned with GFP-GCaMP6s transfected neuronal processes are presented in **Fig. 5.11(c)**. In agreement with **Fig. 5.11(a-b)**, the data demonstrate an increase in fluorescence intensity and a decrease in the intensity of photocurrent signals in the higher K^+ concentration media. Taken together, these results suggest that the graphene-based microfluidic optoelectronic sensing platform can be effectively used as a tool to probe neuronal activities at the individual synapse level.

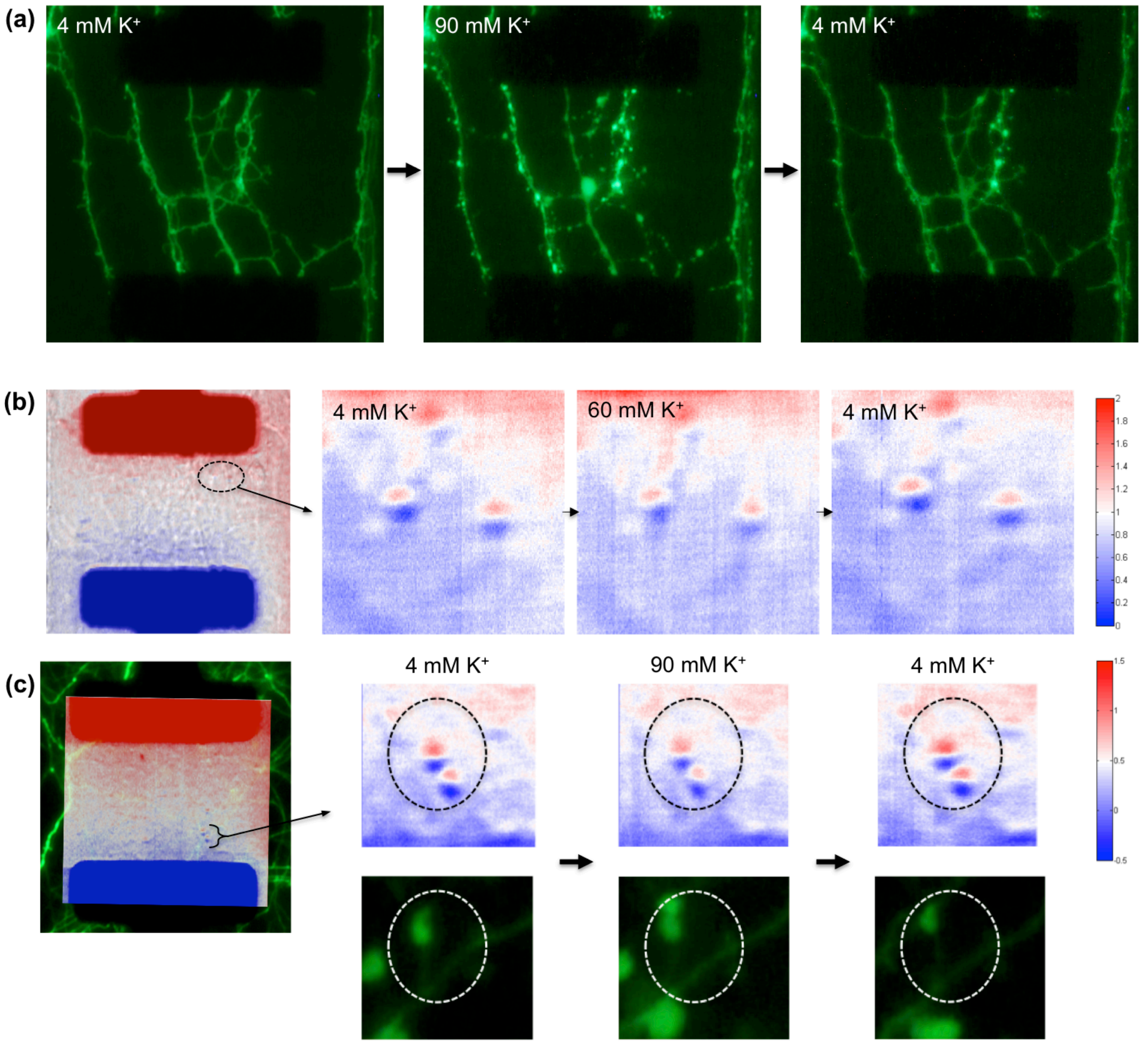

Figure 5.11: Fluorescence and photocurrent results from chemical stimulation experiments in three separate devices. **(a)** A series of fluorescence images demonstrates the change in fluorescence intensity of neuronal processes transfected with a GFP-tagged Ca^{2+} indicator as the culture media is switched from 4 mM K^+ to 90 mM K^+ concentration and then back to 4 mM K^+. **(b)** An overlay of a photocurrent map with a DIC image shows the overlap of photocurrent dots with neuronal processes (left panel). A series of zoomed-in photocurrent maps focused on two photocurrent dots reveals a change in the size and intensity of the dots as the media is cycled between 4 mM K^+ and 60 mM K^+ concentration. **(c)** Simultaneous monitoring of fluorescence and photocurrent images demonstrates concurrent changes in fluorescence intensity and photocurrent dot size and signal magnitude.

5.4 Summary

In summary, we have designed, fabricated, and tested a novel microfluidic system that incorporates an array of graphene transistors that can be combined with scanning photocurrent microscopy to probe neuronal activities with high spatiotemporal resolution. We developed a set of unique fabrication and operational protocols to produce a functioning device that was compatible with neuronal cell culture and optoelectronic measurements. The platform was used to demonstrate the ability to detect neuronal processes, protrusions, spines, and synapses with photocurrent mapping of the graphene sensing region. In addition, the device was used to monitor electrical synaptic activity at the single-synapse level in response to global chemical stimulation. The graphene-based microfluidic scanning photocurrent microscopy platform presented here can potentially be used for more extensive studies of neuronal development and behavior. For instance, the device could be used to examine synapse formation and development or modified for use with entire brain slices. The system can also be extended for use in other realms of cell biology, such as the observation of cancer cell migration across a graphene transistor. Altogether, both the demonstrated capabilities and tremendous future potential of this sensing scheme make it a highly impactful tool for cell biology research.

CHAPTER 6

SUMMARY AND FUTURE OUTLOOK

6.1 Summary

In this dissertation, several novel microfluidic cell culture and co-culture platforms were introduced as engineering solutions for a variety of needs in cell biology studies. Extensive characterization and demonstration of these platforms for a number of cell biology applications have been conducted. Though the new microfluidic designs vary in function and construction, they are all intended to probe important aspects of cell behavior in a controlled *in vitro* environment. These microfluidic systems can serve as high functionality tools that enable studies of cell behavior, response, and interaction (through both direct contact and via soluble factors) under external mechanical, electrical, or chemical stimuli.

First, a microfluidic cell co-culture device that employs a liquid fluorocarbon oil barrier to separate cell populations was presented as an alternative approach to the previously demonstrated solid-PDMS valve-enabled co-culture platform. A thorough characterization of the device was conducted, showing that the oil barrier was stable for extended periods of time and under realistic cell culture conditions. Neurons maintained in each cell culture chamber were separated using the oil barrier and transfected with different colored fluorescent proteins, demonstrating the applicability of the device for neurobiological studies, particularly those focused on synapse formation and function.

Finally, low molecular weight cell staining dyes were employed to show that the oil barrier can provide a better fluidic seal than the solid-PDMS valve design.

Another alternative to the solid-PDMS valve microfluidic device was proposed that uses a thin membrane valve to enable separation of cell populations in three-dimensional cell culture, as well as enhance nutrient/media exchange for cells embedded in a gel matrix. Several different fabrication methods were detailed to create reproducible and functional devices, and parametric studies were conducted using a finite element model, upon which a general guideline for device design was established. A proof-of-concept experiment using colored dyes demonstrated the performance of a two- and three-chamber version of the membrane valve system. Additionally, a collagen gel matrix embedded with nanoparticles was loaded into a membrane valve platform and the resulting flow perfusion was characterized.

Next, the design and development of a microfluidic ligand trap cell culture platform was detailed. The ligand trap allows for the investigation of specific cell signaling pathways by removing particular ligands from the cellular microenvironment using receptor-coated nanoparticles embedded in a nanoporous gel. Fluorescence microscopy was used to characterize the device performance, indicating that the ligand trap could be effective for long time periods and for normal or high binding affinity ligand/receptor pairs. In addition, preliminary ELISA results were presented that attempt to validate the use of the ligand trap device with the important molecule IL-6, which mediates many critical physiological processes including those in neurobiology. Although these initial ELISA results were difficult to reproduce due to the relatively small dynamic detection range of the ELISA assay, limited media exchange, and significant dilution effects, an alternative ligand trap fabrication approach using a photopolymerizable PEGDA gel as the semi-permeable barrier was proposed and demonstrated. This new approach should improve the reproducibility of the ligand trap platform, as well as enable more thorough and consistent quantitative analyses to be conducted.

A microfluidic membrane stretcher scheme was also adapted and developed for use in probing the effects of mechanical stress on fibroblasts. Confocal microscopy was used to characterize the strains achieved on a suspended PDMS membrane for a given applied vacuum pressure. Biological studies showed that culturing NAFs on the device membrane and stretching it initiated cell behaviors similar to those previously observed in CAFs. For instance, the fibronectin organization in the local fibroblast environment changed from randomly oriented fibers in unstretched NAFs to more CAF-like aligned fibers for stretched NAFs. In addition, cancer cells co-cultured with NAFs tended to more closely associate and migrate along the fibroblasts that had been stretched. Finally, the observation that the receptor for the tumor-associated growth factor PDGF is expressed in higher quantities in stretched NAFs suggests that mechanical stress triggers biochemical signaling cascades that could play significant roles in NAF activation and CAF genesis.

Finally, a novel microfluidic sensing scheme was created that integrates a collection of graphene transistors into a microfluidic co-culture device, enabling scanning photocurrent microscopy of neuronal processes and synaptic activity. Several unique fabrication methods were developed to produce a working graphene-based microfluidic optoelectronic sensing platform. The working device was used to map the locations of dendritic spines, protrusions, and synaptic activity in a neuron culture by identifying areas of enhanced photocurrent magnitude produced by interactions between neuronal processes and the graphene substrate at specific locations. In addition, the photocurrent system was employed to successfully monitor changes in synaptic activity upon the global exposure of the neuron culture to a depolarizing chemical stimulus.

6.2 Future Outlook

Significant progress has been achieved in the development and implementation of the microfluidic systems presented in this dissertation. However, given the tremendous potential in this field, there are abundant exciting opportunities still available to further advance the capabilities and applications of each of the described microfluidic cell culture platforms. The following paragraphs outline several potential directions in which the technology may evolve.

First, the double-membrane valve concept presented in Chapter II can be used to create an actual three-dimensional neuron culture system. By simultaneously activating two adjacent membrane valves, a neuron-ECM mixture can be loaded into the channel formed between the pressurized membranes. Then, after the valves are deactivated, the resulting three-dimensional gel will contain a large interfacial surface area with the culture media flowing on each side. As discussed in Chapter II, this will hopefully promote greater health in the neuron populations by enhancing the nutrient/waste exchange within the gel. This concept can be similarly applied to three-dimensional matrix cultures of a variety of cell types.

The ligand trap microfluidic system detailed in Chapter III also has the potential for further development. First, extensive ELISA measurements or other quantitative analyses could be conducted that evaluate the ligand trap performance at various relevant time points. Then, the IL-6 trap design should be employed with actual cells in an effort to observe changes in cellular response when IL-6 is removed from the signaling pathway. Finally, further exploration of the photopolymerizable gelation technique for creating the ligand trap system should result in a more reproducible platform with a simplified fabrication. With this technique, the ligand trap platform can be more easily extended for use in the study of any desired cell signaling pathway.

Additional characterization of the membrane stretcher platform presented in Chapter IV may also be conducted. Primarily, a series of experiments could be performed to elucidate the effects of membrane strain magnitude as well as stretch duration on the modification of NAF behavior. More complex “double” membrane stretchers containing multiple stretchable membranes on a single device may also be implemented as a means to increase experimental throughput. Furthermore, the stretcher design can be used to apply a mechanical stimulus to other cell types. For instance, stretching neurons and observing the resulting response in terms of viability or even synaptic activity could serve as an effective *in vitro* model for investigating traumatic brain injuries.

Finally, for the graphene-based scanning photocurrent microscopy platform detailed in Chapter V, potential future progress could lead to a number of highly impactful developments. For example, micro-contact patterning of the graphene substrate could be employed to direct neurite growth into specific areas on the graphene transistor, improving throughput by guiding more neurites into the sensing region and also providing the capability of investigating engineered/patterned neural networks. Furthermore, the platform could be modified to accommodate whole slices of brain tissue, enabling the study of synaptic events with high spatiotemporal resolution in the context of an intact neural network. Finally, the graphene-based microfluidic system could be adapted for investigations using other cell types, such as using photocurrent mapping to track the migration of cancer cells across a graphene transistor region.

In conclusion, the future outlook for microfluidic cell culture platforms is promising. The pursuit of elucidating increasingly complex information about the behavior and function of cells will require progressively better designed, more sophisticated and powerful tools and approaches. Microfluidics research will undoubtedly be one area that could contribute significantly to this pursuit. Hopefully, the work presented in this dissertation may serve as both a reference and inspiration for the future development of microfluidic cell culture systems.

REFERENCES

Allen, M., & Jones, J. L. (2011). Jekyll and Hyde: The role of the microenvironment on the progression of cancer. *Journal of Pathology*, *223*(2), 162–176.

Altankov, G., Grinnell, F., & Groth, T. (1996). Studies on the biocompatibility of materials: fibroblast reorganization of substratum-bound fibronectin on surfaces varying in wettability. *Journal of Biomedical Materials Research*, *30*(3), 385–91.

Ao, M., Brewer, B. M., Yang, L., Franco Coronel, O. E., Hayward, S. W., Webb, D. J., & Li, D. (2015). Stretching Fibroblasts Remodels Fibronectin and Alters Cancer Cell Migration. *Scientific Reports*, *5*, 8334.

Ao, M., Franco, O. E., Park, D., Raman, D., Williams, K., & Hayward, S. W. (2007). Cross-talk between paracrine-acting cytokine and chemokine pathways promotes malignancy in benign human prostatic epithelium. *Cancer Research*, *67*(9), 4244–53.

Atencia, J., & Beebe, D. J. (2005). Controlled microfluidic interfaces. *Nature*, *437*(7059), 648–55.

Banks, W. A., Kastin, A. J., & Gutierrez, E. G. (1994). Penetration of interleukin-6 across the murine blood-brain barrier. *Neuroscience Letters*, *179*(1), 53–56.

Beebe, D. J., Mensing, G. a, & Walker, G. M. (2002). Physics and applications of microfluidics in biology. *Annual Review of Biomedical Engineering*, *4*, 261–86.

Berthier, J., Loe-Mie, F., Tran, V.-M., Schoumacker, S., Mittler, F., Marchand, G., & Sarrut, N. (2009). On the pinning of interfaces on micropillar edges. *Journal of Colloid and Interface Science*, *338*(1), 296–303.

Bhatia, S. N., Yarmush, M. L., & Toner, M. (1997). Controlling cell interactions by micropatterning in co-cultures: Hepatocytes and 3T3 fibroblasts. *Journal of Biomedical Materials Research*, *34*(2), 189–199.

Bhowmick, N. A., & Moses, H. L. (2005). Tumor-stroma interactions. *Current Opinion in Genetics and Development*, *15*(1), 97–101.

Biffi, E., Piraino, F., Pedrocchi, A., Fiore, G. B., Ferrigno, G., Redaelli, A., Menegon, A., & Rasponi, M. (2012). A microfluidic platform for controlled biochemical stimulation of twin neuronal networks. *Biomicrofluidics*, *6*(2), 24106–2410610.

Bishop, J. E. (1998). Regulation of cardiovascular collagen deposition by mechanical forces. *Molecular Medicine Today*, *4*(2), 69–75.

Blake, P., Hill, E. W., Castro Neto, A. H., Novoselov, K. S., Jiang, D., Yang, R., Booth, T. J., & Geim, A. K. (2007). Making graphene visible. *Applied Physics Letters*, *91*(6), 063124.

Bonaccorso, F., Sun, Z., Hasan, T., & Ferrari, A. C. (2010). Graphene Photonics and Optoelectronics. *Nature Photonics*, *4*(9), 611–622.

Brantley-Sieders, D. M., Caughron, J., Hicks, D., Pozzi, A., Ruiz, J. C., & Chen, J. (2004). EphA2 receptor tyrosine kinase regulates endothelial cell migration and vascular assembly through phosphoinositide 3-kinase-mediated Rac1 GTPase activation. *Journal of Cell Science*, *117*(Pt 10), 2037–2049.

Brantley-Sieders, D. M., Dunaway, C. M., Rao, M., Short, S., Hwang, Y., Gao, Y., Li, D., Jiang, A., Shyr, Y., Wu, J. Y., & Chen, J. (2011). Angiocrine factors modulate tumor proliferation and motility through EphA2 repression of Slit2 tumor suppressor function in endothelium. *Cancer Research*, *71*(3), 976–87.

Brewer, B. M., Shi, M., Edd, J. F., Webb, D. J., & Li, D. (2014). A microfluidic cell co-culture platform with a liquid fluorocarbon separator. *Biomedical Microdevices*, *16*(2), 311–23.

Brown, X. Q., Ookawa, K., & Wong, J. Y. (2005). Evaluation of polydimethylsiloxane scaffolds with physiologically-relevant elastic moduli: Interplay of substrate mechanics and surface chemistry effects on vascular smooth muscle cell response. *Biomaterials*, *26*(16), 3123–3129.

Bruus, H. (2008). *Theoretical Microfluidics* (p. 346). New York: Oxford University Press.

Buck, R. C. (1980). Reorientation response of cells to repeated stretch and recoil of the substratum. *Experimental Cell Research*, *127*(2), 470–474.

Carano, A. (1990). A new experimental approach to the study of mechanical force in orthodontics. *Mondo Ortodontico*, *15*(1), 63–68.

Carver, W., Nagpal, M. L., Nachtigal, M., Borg, T. K., & Terracio, L. (1991). Collagen expression in mechanically stimulated cardiac fibroblasts. *Circulation Research*, *69*(1), 116–122.

Chatterjee, D., Hetayothin, B., Wheeler, A. R., King, D. J., & Garrell, R. L. (2006). Droplet-based microfluidics with nonaqueous solvents and solutions. *Lab on a Chip*, *6*(2), 199–206.

Chechlacz, M., & Gleeson, J. G. (2003). Is mental retardation a defect of synapse structure and function? *Pediatric Neurology*, *29*(1), 11–17.

Chen, C. S., Tan, J., & Tien, J. (2004). Mechanotransduction at cell-matrix and cell-cell contacts. *Annual Review of Biomedical Engineering*, *6*, 275–302.

Chiquet, M., Gelman, L., Lutz, R., & Maier, S. (2009). From mechanotransduction to extracellular matrix gene expression in fibroblasts. *Biochimica et Biophysica Acta - Molecular Cell Research*, *1793*, 911–920.

Chiquet, M., Koch, M., Matthisson, M., Tannheimer, M., & Chiquet-Ehrismann, R. (1996). Regulation of extracellular matrix synthesis by mechanical stress. *Biochemistry and Cell Biology*, *74*(6), 737–744.

Choi, K. M., & Rogers, J. A. (2003). A photocurable poly(dimethylsiloxane) chemistry designed for soft lithographic molding and printing in the nanometer regime. *Journal of the American Chemical Society*, *125*(14), 4060–4061.

Cirri, P., & Chiarugi, P. (2012). Cancer-associated-fibroblasts and tumour cells: A diabolic liaison driving cancer progression. *Cancer and Metastasis Reviews*, *31*(1-2), 195–208.

Claverol-Tinturé, E., Ghirardi, M., Fiumara, F., Rosell, X., & Cabestany, J. (2005). Multielectrode arrays with elastomeric microstructured overlays for extracellular recordings from patterned neurons. *Journal of Neural Engineering*, *2*(2), L1–L7.

Cooper, G. M. (2000). Cell-Cell Interactions. *The Cell: A Molecular Approach* (2nd ed.). Sunderland (MA): Sinauer Associates.

Coussens, L. M., & Werb, Z. (2002). Inflammation and cancer. *Nature*, *420*(6917), 860–867.

Cuchiara, M. P., Allen, A. C. B., Chen, T. M., Miller, J. S., & West, J. L. (2010). Multilayer microfluidic PEGDA hydrogels. *Biomaterials*, *31*(21), 5491–5497.

Dartsch, P. C., Hämmerle, H., & Betz, E. (1986). Orientation of cultured arterial smooth muscle cells growing on cyclically stretched substrates. *Acta Anatomica*, *125*(2), 108–113.

Daskalopoulos, E. P., Janssen, B. J. A., & Blankesteijn, W. M. (2012). Myofibroblasts in the Infarct Area: Concepts and Challenges. *Microscopy and Microanalysis*, *18*(1), 35–49.

Dean, J. B., Bayliss, D. A., Erickson, J. T., Lawing, W. L., & Millhorn, D. E. (1990). Depolarization and stimulation of neurons in nucleus tractus solitarii by carbon dioxide does not require chemical synaptic input. *Neuroscience*, *36*(1), 207–216.

DeBerardinis, R. J., Lum, J. J., Hatzivassiliou, G., & Thompson, C. B. (2008). The Biology of Cancer: Metabolic Reprogramming Fuels Cell Growth and Proliferation. *Cell Metabolism*, *7*(1), 11–20.

Duffy, D. C., McDonald, J. C., Schueller, O. J. A., & Whitesides, G. M. (1998). Rapid prototyping of microfluidic systems in poly(dimethylsiloxane). *Analytical Chemistry*, *70*(23), 4974–4984.

Dunaevsky, A., Tashiro, A., Majewska, A., Mason, C., & Yuste, R. (1999). Developmental regulation of spine motility in the mammalian central nervous system. *Proceedings of the National Academy of Sciences of the United States of America*, *96*(23), 13438–13443.

Esch, M. B., King, T. L., & Shuler, M. L. (2011). The role of body-on-a-chip devices in drug and toxicity studies. *Annual Review of Biomedical Engineering*, *13*, 55–72.

Ethell, I. M., & Pasquale, E. B. (2005). Molecular mechanisms of dendritic spine development and remodeling. *Progress in Neurobiology*, *75*(3), 161–205.

Even-Ram, S., & Yamada, K. M. (2005). Cell migration in 3D matrix. *Current Opinion in Cell Biology*, *17*(5), 524–532.

Ferguson-Smith, a C., Chen, Y. F., Newman, M. S., May, L. T., Sehgal, P. B., & Ruddle, F. H. (1988). Regional localization of the interferon-beta 2/B-cell stimulatory factor 2/hepatocyte stimulating factor gene to human chromosome 7p15-p21. *Genomics*, *2*(3), 203–208.

Ferrer, I., & Gullotta, F. (1990). Down’s syndrome and Alzheimer's disease: Dendritic spine counts in the hippocampus. *Acta Neuropathologica*, *79*(6), 680–685.

Folch, A. (2013). *Introduction to BioMEMS* (1st ed.). Boca Raton: CRC Press.

Fordyce, P. M., Diaz-Botia, C. a, DeRisi, J. L., & Gomez-Sjoberg, R. (2012). Systematic characterization of feature dimensions and closing pressures for microfluidic valves produced via photoresist reflow. *Lab on a Chip*, *12*(21), 4287.

Franco, O. E., & Hayward, S. W. (2012). *Targeting the tumor stroma as a novel therapeutic approach for prostate cancer. Advances in pharmacology* (Vol. 65, pp. 267–313). San Diego, California.

Franco, O. E., Shaw, A. K., Strand, D. W., & Hayward, S. W. (2010). Cancer associated fibroblasts in cancer pathogenesis. *Seminars in Cell and Developmental Biology*, *21*(1), 33–39.

Friedl, P., & Gilmour, D. (2009). Collective cell migration in morphogenesis, regeneration and cancer. *Nature Reviews Molecular Cell Biology*, *10*(7), 445–457.

Gabbiani, G. (2003). The myofibroblast in wound healing and fibrocontractive diseases. *Journal of Pathology*, *200*(4), 500–503.

Gao, Y. (2011). *Microfluidic platforms for cell culture and microenvironment control*. Vanderbilt University.

Gao, Y., Brantley-Sieders, D., Majumdar, D., Chen, J., Webb, D., & Li, D. (2012). A Simple Approach to Probe the Extracellular Signaling Pathways Using Ligand Traps. *ASME 2012 3rd Micro/Nanoscale Heat & Mass Transfer International Conference* (pp. 1–5). Atlanta, GA.

Gao, Y., Majumdar, D., Jovanovic, B., Shaifer, C., Lin, P. C., Zijlstra, A., Webb, D. J., & Li, D. (2011). A versatile valve-enabled microfluidic cell co-culture platform and demonstration of its applications to neurobiology and cancer biology. *Biomedical Microdevices*, *13*(3), 539–548.

Gates, B. D., Xu, Q., Love, J. C., Wolfe, D. B., & Whitesides, G. M. (2004). Unconventional Nanofabrication. *Annual Review of Materials Research*, *34*(1), 339–372.

Geim, A. K., & Novoselov, K. S. (2007). The rise of graphene. *Nature Materials*, *6*(3), 183–191.

Giannoni, E., Bianchini, F., Masieri, L., Serni, S., Torre, E., Calorini, L., & Chiarugi, P. (2010). Reciprocal activation of prostate cancer cells and cancer-associated fibroblasts stimulates epithelial-mesenchymal transition and cancer stemness. *Cancer Research*, *70*(17), 6945–6956.

Goetz, J. G., Minguet, S., Navarro-Lérida, I., Lazcano, J. J., Samaniego, R., Calvo, E., Tello, M., Osteso-Ibanez, T., Pellinen, T., Echarri, A., Cerezo, A., Klein-Szanto, A. J. P., Garcia, R., Keely, P. J., Sanchez-Mateos, P., Cukierman, E., & Del Pozo, M. A. (2011). Biomechanical remodeling of the microenvironment by stromal caveolin-1 favors tumor invasion and metastasis. *Cell*, *146*(1), 148–163.

Gonda, T. A., Tu, S., & Wang, T. C. (2009). Chronic inflammation, the tumor microenvironment and carcinogenesis. *Cell Cycle*, *8*(13), 2005–2013.

Goslin, K., Asmussen, H., Banker, G. (1998). Rat hippocampal neurons in low-density culture. In K. Banker, G., Goslin (Ed.), *Culturing Nerve Cells* (2nd ed., pp. 339–370). Cambridge, MA: MIT Press.

Gray, D. S., Tien, J., & Chen, C. S. (2003). Repositioning of cells by mechanotaxis on surfaces with micropatterned Young's modulus. *Journal of Biomedical Materials Research Part A*, *66*(3), 605–614.

Halliday, N. L., & Tomasek, J. J. (1995). Mechanical properties of the extracellular matrix influence fibronectin fibril assembly in vitro. *Experimental Cell Research*, *217*(1), 109–117.

Hansson, G. K., Robertson, A.-K. L., & Söderberg-Nauclér, C. (2006). Inflammation and atherosclerosis. *Annual Review of Pathology*, *1*, 297–329.

Herbert, T. B., & Cohen, S. (1993). Stress and immunity in humans: a meta-analytic review. *Psychosomatic Medicine*, *55*(4), 364–379.

Hibara, A., Iwayama, S., Matsuoka, S., Ueno, M., Kikutani, Y., Tokeshi, M., & Kitamori, T. (2005). Surface modification method of microchannels for gas-liquid two-phase flow in microchips. *Analytical Chemistry*, *77*(3), 943–947.

Hibara, A., Nonaka, M., Hisamoto, H., Uchiyama, K., Kikutani, Y., Tokeshi, M., & Kitamori, T. (2002). Stabilization of liquid interface and control of two-phase confluence and separation in glass microchips by utilizing octadecylsilane modification of microchannels. *Analytical Chemistry*, *74*(7), 1724–1728.

Hosmane, S., Fournier, A., Wright, R., Rajbhandari, L., Siddique, R., Yang, I. H., Ramesh, K. T., Venkatesan, A., & Thakor, N. (2011). Valve-based microfluidic compression platform: single axon injury and regrowth. *Lab on a Chip*, *11*(22), 3888.

Hosokawa, K., Sato, K., Ichikawa, N., & Maeda, M. (2004). Power-free poly(dimethylsiloxane) microfluidic devices for gold nanoparticle-based DNA analysis. *Lab on a Chip*, *4*(3), 181–185.

Hsu, C.-H., Chen, C., & Folch, A. (2004). "Microcanals" for micropipette access to single cells in microfluidic environments. *Lab on a Chip*, *4*(5), 420–424.

Hu, C., Wang, Z., Zhai, L., Yang, M., Shan, L., Chai, C., Liu, M., & Wang, L. (2013). Effects of cancer-associated fibroblasts on the migration and invasion abilities of SGC-7901 gastric cancer cells. *Oncology Letters*, *5*(2), 609–612. Spandidos Publications.

Huang, C., Miyazaki, K., Akaishi, S., Watanabe, A., Hyakusoku, H., & Ogawa, R. (2013). Biological effects of cellular stretch on human dermal fibroblasts. *Journal of plastic, reconstructive & aesthetic surgery*, *66*(12), e351–61.

Huang, S., & Ingber, D. E. (2005). Cell tension, matrix mechanics, and cancer development. *Cancer Cell*, *8*(3), 175–176.

Huh, D., Hamilton, G. a, & Ingber, D. E. (2011). From 3D cell culture to organs-on-chips. *Trends in Cell Biology*, *21*(12), 745–754.

Huh, D., Matthews, B. D., Mammoto, A., Montoya-Zavala, M., Hsin, H. Y., & Ingber, D. E. (2010). Reconstituting organ-level lung functions on a chip. *Science*, *328*(5986), 1662–1668.

Imura, Y., Asano, Y., Sato, K., & Yoshimura, E. (2009). A microfluidic system to evaluate intestinal absorption. *Analytical Sciences : The International Journal of the Japan Society for Analytical Chemistry*, *25*(12), 1403–1407.

Ishaug, S. L., Crane, G. M., Miller, M. J., Yasko, A. W., Yaszemski, M. J., & Mikos, A. G. (1997). Bone formation by three-dimensional stromal osteoblast culture in biodegradable polymer scaffolds. *Journal of Biomedical Materials Research*, *36*(1), 17–28.

Jang, K.-J., & Suh, K.-Y. (2010). A multi-layer microfluidic device for efficient culture and analysis of renal tubular cells. *Lab on a Chip*, *10*(1), 36–42.

Jean, L., Majumdar, D., Shi, M., Hinkle, L. E., Diggins, N. L., Ao, M., Broussard, J. A., Evans, J. C., Choma, D. P., & Webb, D. J. (2013). Activation of Rac by Asef2 promotes myosin II-dependent contractility to inhibit cell migration on type I collagen. *Journal of Cell Science*, *126*(Pt 24), 5585–97.

Jilka, R. L., Hangoc, G., Girasole, G., Passeri, G., Williams, D. C., Abrams, J. S., Boyce, B., Broxmeyer, H., & Manolagas, S. C. (1992). Increased osteoclast development after estrogen loss: mediation by interleukin-6. *Science*, *257*(5066), 88–91.

Kalluri, R., & Zeisberg, M. (2006). Fibroblasts in cancer. *Nature Reviews Cancer*, *6*(5), 392–401.

Kam, L. C., Shen, K., & Dustin, M. L. (2013). Micro- and nanoscale engineering of cell signaling. *Annual Review of Biomedical Engineering*, *15*, 305–26.

Kandel, E. R., Schwartz, J. H., & Jessel, T. M. (2000). *Principles of Neural Science* (4th ed.). McGraw-Hill.

Kane, B. J., Zinner, M. J., Yarmush, M. L., & Toner, M. (2006). Liver-specific functional studies in a microfluidic array of primary mammalian hepatocytes. *Analytical Chemistry*, *78*(13), 4291–4298.

Kang, J. H., Kim, Y. C., & Park, J.-K. (2008). Analysis of pressure-driven air bubble elimination in a microfluidic device. *Lab on a Chip*, *8*(1), 176–178.

Khetani, S. R., & Bhatia, S. N. (2008). Microscale culture of human liver cells for drug development. *Nature Biotechnology*, *26*(1), 120–126.

Kimura, H., Yamamoto, T., Sakai, H., Sakai, Y., & Fujii, T. (2008). An integrated microfluidic system for long-term perfusion culture and on-line monitoring of intestinal tissue models. *Lab on a Chip*, *8*(5), 741–746.

Kiskowski, M. A., Jackson, R. S., Banerjee, J., Li, X., Kang, M., Iturregui, J. M., Franco, O. E., Hayward, S. W., & Bhowmick, N. A. (2011). Role for stromal heterogeneity in prostate tumorigenesis. *Cancer Research*, *71*(10), 3459–3470.

Köster, S., Angilè, F. E., Duan, H., Agresti, J. J., Wintner, A., Schmitz, C., Rowat, A. C., Merten, C. A., Pisignano, D., Griffiths A. D., & Weitz, D. A. (2008). Drop-based microfluidic devices for encapsulation of single cells. *Lab on a Chip*, *8*(7), 1110–1115.

Lai, H. H., Xu, W., & Allbritton, N. L. (2011). Use of a virtual wall valve in polydimethylsiloxane microfluidic devices for bioanalytical applications. *Biomicrofluidics*, *5*(2), 24105.

Langevin, H. M., Bouffard, N. A., Badger, G. J., Iatridis, J. C., & Howe, A. K. (2005). Dynamic fibroblast cytoskeletal response to subcutaneous tissue stretch ex vivo and in vivo. *American Journal of Physiology. Cell Physiology*, *288*(3), C747–C756.

Larsen, G. L., & Henson, P. M. (1983). Mediators of inflammation. *Annual Review of Immunology*, *1*(1), 335–359. A.

Lee, A. A., Delhaas, T., McCulloch, A. D., & Villarreal, F. J. (1999). Differential responses of adult cardiac fibroblasts to in vitro biaxial strain patterns. *Journal of Molecular and Cellular Cardiology*, *31*(10), 1833–1843.

Lee, C., Wei, X., Kysar, J. W., & Hone, J. (2008). Measurement of the elastic properties and intrinsic strength of monolayer graphene. *Science*, *321*(5887), 385–388.

Lee, J. N., Park, C., & Whitesides, G. M. (2003). Solvent Compatibility of Poly(dimethylsiloxane)-Based Microfluidic Devices. *Analytical Chemistry*, *75*(23), 6544–6554.

Lekic, P., & Mcculloch, C. A. G. (1996). Periodontal ligament cell populations: The central role of fibroblasts in creating a unique tissue. *Anatomical Record*, *245*(2), 327–341.

Li, C. Y., Shan, S., Huang, Q., Braun, R. D., Lanzen, J., Hu, K., Lin, P., & Dewhirst, M. W. (2000). Initial stages of tumor cell-induced angiogenesis: evaluation via skin window chambers in rodent models. *Journal of the National Cancer Institute*, *92*(2), 143–147.

Li Jeon, N., Baskaran, H., Dertinger, S. K. W., Whitesides, G. M., Van de Water, L., & Toner, M. (2002). Neutrophil chemotaxis in linear and complex gradients of interleukin-8 formed in a microfabricated device. *Nature Biotechnology*, *20*(8), 826–830.

Li, N., Zhang, X., Song, Q., Su, R., Zhang, Q., Kong, T., Liu, L., Jin, G., Tang, M., & Cheng, G. (2011). The promotion of neurite sprouting and outgrowth of mouse hippocampal cells in culture by graphene substrates. *Biomaterials*, *32*(35), 9374–9382.

Li, X., Cai, W., An, J., Kim, S., Nah, J., Yang, D., Piner, R., Velamakanni, A., Jung, I., Tutuc, E., Banerjee, S. K., Colombo, L., & Ruoff, R. S. (2009). Large-area synthesis of high-quality and uniform graphene films on copper foils. *Science*, *324*(5932), 1312–1314.

Li, X., Zhu, Y., Cai, W., Borysiak, M., Han, B., Chen, D., Piner, R. D., Colombo, L., & Ruoff, R. S. (2009). Transfer of large-area graphene films for high-performance transparent conductive electrodes. *Nano Letters*, *9*(12), 4359–4363.

Li, Z., & Sheng, M. (2003). Some assembly required: the development of neuronal synapses. *Nature Reviews Molecular Cell Biology*, *4*(11), 833–841.

Liu, M., Sun, J., Sun, Y., Bock, C., & Chen, Q. (2009, March 1). Thickness-dependent mechanical properties of polydimethylsiloxane membranes. *Journal of Micromechanics and Microengineering*.

Livnah, O., Bayer, E. a, Wilchek, M., & Sussman, J. L. (1993). Three-dimensional structures of avidin and the avidin-biotin complex. *Proceedings of the National Academy of Sciences of the United States of America*, *90*(11), 5076–5080.

Lodish, H., Berk, A., Zipursky, S. L., Matsudaira, P., Baltimore, D., & Darnell, J. (2000). Overview of Extracellular Signaling. *Molecular Cell Biology* (4th ed.). New York: W.H. Freeman.

Lowe, K. C., Davey, M. R., & Power, J. B. (1998). Perfluorochemicals: Their applications and benefits to cell culture. *Trends in Biotechnology*, *16*(6), 272–278.

Lucchetta, E. M., Lee, J. H., Fu, L. a, Patel, N. H., & Ismagilov, R. F. (2005). Dynamics of Drosophila embryonic patterning network perturbed in space and time using microfluidics. *Nature*, *434*(7037), 1134–1138.

Lynn, N. S., & Dandy, D. S. (2009). Passive microfluidic pumping using coupled capillary/evaporation effects. *Lab on a Chip*, *9*(23), 3422–3429.

Majumdar, D., Gao, Y., Li, D., & Webb, D. J. (2011). Co-culture of neurons and glia in a novel microfluidic platform. *Journal of Neuroscience Methods*, *196*(1), 38–44.

Marcus, J. S., Anderson, W. F., & Quake, S. R. (2006). Microfluidic single-cell mRNA isolation and analysis. *Analytical Chemistry*, *78*(9), 3084–3089.

Maruyama, T., Matsushita, H., Uchida, J., Kubota, F., Kamiya, N., & Goto, M. (2004). Liquid membrane operations in a microfluidic device for selective separation of metal ions. *Analytical Chemistry*, *76*(15), 4495–4500.

Maruyama, T., Uchida, J., Ohkawa, T., Futami, T., Katayama, K., Nishizawa, K., Sotowa, K., Kubota, F., Kamiya, N., & Goto, M. (2003). Enzymatic degradation of p-chlorophenol in a two-phase flow microchannel system. *Lab on a Chip*, *3*(4), 308–312.

Matus, A., Ackermann, M., Pehling, G., Byers, H. R., & Fujiwara, K. (1982). High actin concentrations in brain dendritic spines and postsynaptic densities. *Proceedings of the National Academy of Sciences of the United States of America*, *79*(23), 7590–7594.

Mazutis, L., & Griffiths, A. D. (2012, April 24). Selective droplet coalescence using microfluidic systems. *Lab on a Chip*.

McDonald, J. C., & Whitesides, G. M. (2002). Poly(dimethylsiloxane) as a material for fabricating microfluidic devices. *Accounts of Chemical Research*, *35*(7), 491–499.

Mehling, M., & Tay, S. (2014). Microfluidic cell culture. *Current Opinion in Biotechnology*, *25*, 95–102.

Melin, J., & Quake, S. R. (2007). Microfluidic large-scale integration: the evolution of design rules for biological automation. *Annual Review of Biophysics and Biomolecular Structure*, *36*, 213–231.

Mendonça Torres, P. M., & de Araujo, E. G. (2001). Interleukin-6 increases the survival of retinal ganglion cells in vitro. *Journal of Neuroimmunology*, *117*(1-2), 43–50.

Merkel, T. C., Bondar, V. I., Nagai, K., Freeman, B. D., & Pinnau, I. (2000). Gas sorption, diffusion, and permeation in poly(dimethylsiloxane). *Journal of Polymer Science, Part B: Polymer Physics*, *38*(3), 415–434.

Meyvantsson, I., & Beebe, D. J. (2008). Cell culture models in microfluidic systems. *Annual Review of Analytical Chemistry*, *1*, 423–449.

Mukhopadhyay, R. (2007). When PDMS isn't the best. *Analytical Chemistry*, *79*(9), 3248–3253.

Murakami, M., Hibi, M., Nakagawa, N., Nakagawa, T., Yasukawa, K., Yamanishi, K., Taga, T., & Kishimoto, T. (1993). IL-6-induced homodimerization of gp130 and associated activation of a tyrosine kinase. *Science*, *260*(5115), 1808–1810.

Nahshol, O., Bronner, V., Notcovich, A., Rubrecht, L., Laune, D., & Bravman, T. (2008). Parallel kinetic analysis and affinity determination of hundreds of monoclonal antibodies using the ProteOn XPR36. *Analytical Biochemistry*, *383*(1), 52–60.

Nair, R. R., Blake, P., Grigorenko, A. N., Novoselov, K. S., Booth, T. J., Stauber, T., Peres, N. M. R., & Geim, A. K. (2008). Fine structure constant defines visual transparency of graphene. *Science*, *320*(5881), 1308.

Neidlinger-Wilke, C., Grood, E. S., Wang, J. H. C., Brand, R. A., & Claes, L. (2001). Cell alignment is induced by cyclic changes in cell length: Studies of cells grown in cyclically stretched substrates. *Journal of Orthopaedic Research*, *19*(2), 286–293.

Nelson, C. M., & Bissell, M. J. (2006). Of extracellular matrix, scaffolds, and signaling: tissue architecture regulates development, homeostasis, and cancer. *Annual Review of Cell and Developmental Biology*, *22*, 287–309.

Novoselov, K. S., Geim, A. K., Morozov, S. V., Jiang, D., Zhang, Y., Dubonos, S. V., Grigorieva, I. V., & Firsov, A. A. (2004). Electric field effect in atomically thin carbon films. *Science*, *306*(5696), 666–669.

Oka, H., Shimono, K., Ogawa, R., Sugihara, H., & Taketani, M. (1999). A new planar multielectrode array for extracellular recording: Application to hippocampal acute slice. *Journal of Neuroscience Methods*, *93*(1), 61–67.

Olumi, A. F., Grossfeld, G. D., Hayward, S. W., Carroll, P. R., Tlsty, T. D., & Cunha, G. R. (1999). Carcinoma-associated Fibroblasts Direct Tumor Progression of Initiated Human Prostatic Epithelium. *Cancer Research*, *59*(19), 5002–5011.

Orimo, A., Gupta, P. B., Sgroi, D. C., Arenzana-Seisdedos, F., Delaunay, T., Naeem, R., Carey, V. J., Richardson, A. L., & Weinberg, R. A. (2005). Stromal fibroblasts present in invasive human breast carcinomas promote tumor growth and angiogenesis through elevated SDF-1/CXCL12 secretion. *Cell*, *121*(3), 335–348.

Östman, A., & Heldin, C. H. (2007). PDGF Receptors as Targets in Tumor Treatment. *Advances in Cancer Research*, *97*(06), 247–274.

Östman, A., & Heldin, C.-H. (2001). Involvement of platelet-derived growth factor in disease: development of specific antagonists. *Advances in Cancer Research*, *80*, 1–38.

Pankov, R., Endo, Y., Even-Ram, S., Araki, M., Clark, K., Cukierman, E., Matsumoto, K., & Yamada, K. M. (2005). A Rac switch regulates random versus directionally persistent cell migration. *Journal of Cell Biology*, *170*(5), 793–802.

Park, S. Y., Park, J., Sim, S. H., Sung, M. G., Kim, K. S., Hong, B. H., & Hong, S. (2011). Enhanced differentiation of human neural stem cells into neurons on graphene. *Advanced Materials*, *23*(36), H263–7.

Parkin, D. M., Pisani, P., & Ferlay, J. (1999). Global cancer statistics. *CA: A Cancer Journal for Clinicians*, *49*(2), 33–64.

Peterson, W. M., Meggyesy, C., Yu, K., & Miller, S. S. (1997). Extracellular ATP activates calcium signaling, ion, and fluid transport in retinal pigment epithelium. *The Journal of Neuroscience*, *17*(7), 2324–2337.

Phan, S. H. (2010). The Myofibroblast in Pulmonary Fibrosis. *Chest*, *122*(6_suppl), 286S.

Pietras, K., Stumm, M., Hubert, M., Buchdunger, E., Rubin, K., Heldin, C.-H., McSheehy, P., Wartmann, M., & Ostman, A. (2003). STI571 Enhances the Therapeutic Index of Epothilone B by a Tumor-selective Increase of Drug Uptake. *Clinical Cancer Research*, *9*(10), 3779–3787.

Polacheck, W. J., Li, R., Uzel, S. G. M., & Kamm, R. D. (2013). Microfluidic platforms for mechanobiology. *Lab on a Chip*, *13*(12), 2252–67.

Polanska, U. M., & Orimo, A. (2013). Carcinoma-associated fibroblasts: Non-neoplastic tumour-promoting mesenchymal cells. *Journal of Cellular Physiology*, *228*(8), 1651–1657.

Van der Poll, T., Keogh, C. V, Guirao, X., Buurman, W. a, Kopf, M., & Lowry, S. F. (1997). Interleukin-6 gene-deficient mice show impaired defense against pneumococcal pneumonia. *The Journal of Infectious Diseases*, *176*(2), 439–444.

Puleo, C. M., McIntosh Ambrose, W., Takezawa, T., Elisseeff, J., & Wang, T.-H. (2009). Integration and application of vitrified collagen in multilayered microfluidic devices for corneal microtissue culture. *Lab on a Chip*, *9*(22), 3221–3227.

Py, C., Denhoff, M. W., Martina, M., Monette, R., Comas, T., Ahuja, T., Martinez, D., Wingar, S., Caballero, J., Laframboise, S., Mielke, J., Bogdanov, A., Luk, C., Syed, N., & Mealing, G. (2010). A novel silicon patch-clamp chip permits high-fidelity recording of ion channel activity from functionally defined neurons. *Biotechnology and Bioengineering*, *107*(4), 593–600.

Ravula, S. K., Wang, M. S., Asress, S. a, Glass, J. D., & Bruno Frazier, A. (2007). A compartmented neuronal culture system in microdevice format. *Journal of Neuroscience Methods*, *159*(1), 78–85.

Ren, X., Bachman, M., Sims, C., Li, G. P., & Allbritton, N. (2001). Electroosmotic properties of microfluidic channels composed of poly(dimethylsiloxane). *Journal of Chromatography B: Biomedical Sciences and Applications*, *762*(2), 117–125.

Rhoads, R. E. (1999, October 22). Signal transduction pathways that regulate eukaryotic protein synthesis. *Journal of Biological Chemistry*.

Sappington, R. M., Chan, M., & Calkins, D. J. (2006). Interleukin-6 protects retinal ganglion cells from pressure-induced death. *Investigative Ophthalmology and Visual Science*, *47*(7), 2932–2942.

Sarrazy, V., Billet, F., Micallef, L., Coulomb, B., & Desmoulière, A. (2011). Mechanisms of pathological scarring: Role of myofibroblasts and current developments. *Wound Repair and Regeneration*, *19*(Suppl 1), s10–s15.

Schedin, F., Geim, A. K., Morozov, S. V, Hill, E. W., Blake, P., Katsnelson, M. I., & Novoselov, K. S. (2007). Detection of individual gas molecules adsorbed on graphene. *Nature Materials*, *6*(9), 652–655.

Scheiffele, P. (2003). Cell-cell signaling during synapse formation in the CNS. *Annual Review of Neuroscience*, *26*, 485–508.

Schmid-Schönbein, G. W. (2006). Analysis of inflammation. *Annual Review of Biomedical Engineering*, *8*, 93–131.

Schomburg, W. K. (2011). *Introduction to Microsystem Design* (Vol. 1). Berlin, Heidelberg: Springer Berlin Heidelberg.

Shestopalov, I., Tice, J. D., & Ismagilov, R. F. (2004). Multi-step synthesis of nanoparticles performed on millisecond time scale in a microfluidic droplet-based system. *Lab on a Chip*, *4*(4), 316–321.

Shi, M., Majumdar, D., Gao, Y., Brewer, B. M., Goodwin, C. R., McLean, J. A., Li, D., & Webb, D. J. (2013). Glia co-culture with neurons in microfluidic platforms promotes the formation and stabilization of synaptic contacts. *Lab on a Chip*, *13*(15), 3008–21.

Shi, W., Wen, H., Lu, Y., Shi, Y., Lin, B., & Qin, J. (2010). Droplet microfluidics for characterizing the neurotoxin-induced responses in individual Caenorhabditis elegans. *Lab on a Chip*, *10*(21), 2855–2863.

Shi, Z.-D., & Tarbell, J. M. (2011). Fluid flow mechanotransduction in vascular smooth muscle cells and fibroblasts. *Annals of Biomedical Engineering*, *39*(6), 1608–1619.

Shieh, A. C. (2011). Biomechanical forces shape the tumor microenvironment. *Annals of Biomedical Engineering*, *39*(5), 1379–1389.

Shoham, D., Glaser, D. E., Arieli, A., Kenet, T., Wijnbergen, C., Toledo, Y., Hildesheim, R., & Grinvald, A. (1999). Imaging Cortical Dynamics at High Spatial and Temporal Resolution with Novel Blue Voltage-Sensitive Dyes. *Neuron*, *24*(4), 791–802.

Sigma-Aldrich. (2013). Material Safety Data Sheet - Tetrabutylammonium fluoride solution. Saint Louis. Retrieved April 3, 2014, from http://www.sigmaaldrich.com/MSDS/MSDS/DisplayMSDSPage.do?country=US&language=en&productNumber=216143&brand=ALDRICH&PageToGoToURL=http://www.sigmaaldrich.com/catalog/product/aldrich/216143?lang=en

Sims, S. M., Holmgren, L., Cathcart, H. M., & Sappington, R. M. (2012). Spatial regulation of interleukin-6 signaling in response to neurodegenerative stressors in the retina. *American Journal of Neurodegenerative Disease*, *1*(2), 168–79.

Skelley, A. M., & Voldman, J. (2008). An active bubble trap and debubbler for microfluidic systems. *Lab on a Chip*, *8*(10), 1733–1737.

Skinner, M. (1991). Cell-cell interactions in the testis. *Endocrine Reviews*, *12*(1), 45–77.

Smith, Y., Villalba, R. M., & Raju, D. V. (2009). Striatal spine plasticity in Parkinson's disease: pathological or not? *Parkinsonism and Related Disorders*, *15*, S156–S161.

Sorra, K. E., & Harris, K. M. (2000). Overview on the structure, composition, function, development, and plasticity of hippocampal dendritic spines. *Hippocampus*, *10*(5), 501–511.

Squires, T., & Quake, S. (2005). Microfluidics: Fluid physics at the nanoliter scale. *Reviews of Modern Physics*, *77*(July), 977.

Stetler-Stevenson, W. G., Aznavoorian, S., & Liotta, L. A. (1993). Tumor cell interactions with the extracellular matrix during invasion and metastasis. *Annual Review of Cell Biology*, *9*, 541–573.

Steward, R. L., Cheng, C.-M., Ye, J. D., Bellin, R. M., & LeDuc, P. R. (2011). Mechanical stretch and shear flow induced reorganization and recruitment of fibronectin in fibroblasts. *Scientific Reports*, *1*(147).

Sung, J. H., & Shuler, M. L. (2009). Prevention of air bubble formation in a microfluidic perfusion cell culture system using a microscale bubble trap. *Biomedical Microdevices*, *11*(4), 731–738.

Surmeian, M., Slyadnev, M. N., Hisamoto, H., Hibara, A., Uchiyama, K., & Kitamori, T. (2002). Three-layer flow membrane system on a microchip for investigation of molecular transport. *Analytical Chemistry*, *74*(9), 2014–2020.

Takayama, S., McDonald, J. C., Ostuni, E., Liang, M. N., Kenis, P. J., Ismagilov, R. F., & Whitesides, G. M. (1999). Patterning cells and their environments using multiple laminar fluid flows in capillary networks. *Proceedings of the National Academy of Sciences of the United States of America*, *96*(10), 5545–5548.

Takechi, H., Eilers, J., & Konnerth, A. (1998). A new class of synaptic response involving calcium release in dendritic spines. *Nature*, *396*(6713), 757–760.

Taylor, A. M., Blurton-Jones, M., Rhee, S. W., Cribbs, D. H., Cotman, C. W., & Jeon, N. L. (2005). A microfluidic culture platform for CNS axonal injury, regeneration and transport. *Nature Methods*, *2*(8), 599–605.

Taylor, A. M., Rhee, S. W., Tu, C. H., Cribbs, D. H., Cotman, C. W., & Jeon, N. L. (2003). Microfluidic multicompartment device for neuroscience research. *Langmuir*, *19*(5), 1551–1556.

Tetala, K. K. R., Swarts, J. W., Chen, B., Janssen, A. E. M., & van Beek, T. a. (2009). A three-phase microfluidic chip for rapid sample clean-up of alkaloids from plant extracts. *Lab on a Chip*, *9*(14), 2085–2092.

Tibbitt, M. W., & Anseth, K. S. (2009). Hydrogels as extracellular matrix mimics for 3D cell culture. *Biotechnology and Bioengineering*, *103*(4), 655–663.

Toepke, M. W., & Beebe, D. J. (2006). PDMS absorption of small molecules and consequences in microfluidic applications. *Lab on a Chip*, *6*(12), 1484–1486.

Tomasek, J. J., Gabbiani, G., Hinz, B., Chaponnier, C., & Brown, R. A. (2002). Myofibroblasts and mechano-regulation of connective tissue remodelling. *Nature Reviews Molecular Cell Biology*, *3*(5), 349–363.

Tourovskaia, A., Figueroa-Masot, X., & Folch, A. (2005). Differentiation-on-a-chip: a microfluidic platform for long-term cell culture studies. *Lab on a Chip*, *5*(1), 14–19.

Unger, M. A., Chou, H. P., Thorsen, T., Scherer, A., & Quake, S. R. (2000). Monolithic microfabricated valves and pumps by multilayer soft lithography. *Science*, *288*(5463), 113–116.

Valastyan, S., & Weinberg, R. A. (2011). Tumor metastasis: molecular insights and evolving paradigms. *Cell*, *147*(2), 275–92.

Ventsel, E., & Krauthammer, T. (2001). *Thin Plates and Shells: Theory, Analysis, and Applications*. New York: Marcel Decker.

Walker, G. M., & Beebe, D. J. (2002). A passive pumping method for microfluidic devices. *Lab on a Chip*, *2*(3), 131–4.

Wang, S. J., Geng, Y., Zheng, Q., & Kim, J.-K. (2010). Fabrication of highly conducting and transparent graphene films. *Carbon*, *48*(6), 1815–1823.

Weidenhamer, N. K., & Tranquillo, R. T. (2013). Influence of cyclic mechanical stretch and tissue constraints on cellular and collagen alignment in fibroblast-derived cell sheets. *Tissue Engineering Part C: Methods*, *19*(5), 386–95.

De Wever, O., & Mareel, M. (2003). Role of tissue stroma in cancer cell invasion. *The Journal of Pathology*, *200*(4), 429–447.

De Wever, O., Nguyen, Q.-D., Van Hoorde, L., Bracke, M., Bruyneel, E., Gespach, C., & Mareel, M. (2004). Tenascin-C and SF/HGF produced by myofibroblasts in vitro provide convergent pro-invasive signals to human colon cancer cells through RhoA and Rac. *The FASEB Journal*, *18*(9), 1016–1018.

Whitesides, G. M. (2006). The origins and the future of microfluidics. *Nature*, *442*(7101), 368–373.

Whitesides, G. M., Ostuni, E., Takayama, S., Jiang, X., & Ingber, D. E. (2001). Soft lithography in biology and biochemistry. *Annual Review of Biomedical Engineering*, *3*, 335–373.

Wolfer, D. P., Crusio, W. E., & Lipp, H. P. (2002). Knockout mice: Simple solutions to the problems of genetic background and flanking genes. *Trends in Neurosciences*, *25*(7), 336–340.

Xia, F., Mueller, T., Golizadeh-Mojarad, R., Freitage, M., Lin, Y. M., Tsang, J., Perebeinos, V., & Avouris, P. (2009). Photocurrent imaging and efficient photon detection in a graphene transistor. *Nano Letters*, *9*(3), 1039–1044.

Xing, F., Saidou, J., & Watabe, K. (2010). Cancer associated fibroblasts (CAFs) in tumor microenvironment. *Frontiers in Bioscience*, *15*(1), 166–179.

Xu, W., Xue, H., Bachman, M., & Li, G. P. (2006). Virtual walls in microchannels. *Annual International Conference of the IEEE Engineering in Medicine and Biology - Proceedings* (Vol. 1, pp. 2840–2843).

Yang, N., Mosher, R., Seo, S., Beebe, D., & Friedl, A. (2011). Syndecan-1 in breast cancer stroma fibroblasts regulates extracellular matrix fiber organization and carcinoma cell motility. *American Journal of Pathology*, *178*(1), 325–335.

Young, E. W. K., & Beebe, D. J. (2010). Fundamentals of microfluidic cell culture in controlled microenvironments. *Chemical Society Reviews*, *39*(3), 1036–1048.

Zetter, B. R. (1998). Angiogenesis and tumor metastasis. *Annual Review of Medicine*, *49*, 407–424.

Zhang, H., Webb, D. J., Asmussen, H., & Horwitz, A. F. (2003). Synapse formation is regulated by the signaling adaptor GIT1. *Journal of Cell Biology*, *161*(1), 131–142.

Zhao, B., Viernes, N. O. L., Moore, J. S., & Beebe, D. J. (2002). Control and applications of immiscible liquids in microchannels. *Journal of the American Chemical Society*, *124*(19), 5284–5285.

Zheng, W., Wang, Z., Zhang, W., & Jiang, X. (2010). A simple PDMS-based microfluidic channel design that removes bubbles for long-term on-chip culture of mammalian cells. *Lab on a Chip*, *10*(21), 2906–2910.

Zimmermann, H., & Whittaker, V. P. (1974). Effect of electrical stimulation on the yield and composition of synaptic vesicles from the cholinergic synapses of the electric organ of Torpedo: a combined biochemical, electrophysiological and morphological study. *Journal of Neurochemistry*, *22*(3), 435–450.